

T-2470

MEASUREMENTS AND MODELING
OF ROCK MASS RESPONSE
TO UNDERGROUND EXCAVATION

By

Abdel Wadood M. A. El Rabaa

ProQuest Number: 10782265

All rights reserved

INFORMATION TO ALL USERS

The quality of this reproduction is dependent upon the quality of the copy submitted.

In the unlikely event that the author did not send a complete manuscript and there are missing pages, these will be noted. Also, if material had to be removed, a note will indicate the deletion.



ProQuest 10782265

Published by ProQuest LLC (2018). Copyright of the Dissertation is held by the Author.

All rights reserved.

This work is protected against unauthorized copying under Title 17, United States Code
Microform Edition © ProQuest LLC.

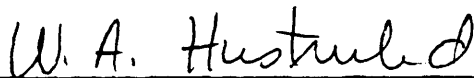
ProQuest LLC.
789 East Eisenhower Parkway
P.O. Box 1346
Ann Arbor, MI 48106 – 1346


A thesis submitted to the Faculty and Board of Trustees of the Colorado School of Mines in partial fulfillment of the requirements for the degree of Master of Science in mining engineering.

Signed: 
Abdel Wadood El Rabaa

Golden, Colorado

Date: Dec 15, 1981

Approved: 
Dr. W. A. Hustrulid
Thesis Advisor


Dr. Phyl B. Johnson, Head
Department of Mining Engineering

Golden, Colorado

Date: Dec 15, 1981

ABSTRACT

The Colorado School of Mines under sponsorship of the Department of Energy through the Office of Nuclear Waste Isolation (ONWI) has established a hard rock research facility at its Experimental Mine near Idaho Springs, Colorado. The purpose of this facility was to evaluate/develop mining, geologic and geotechnical procedures appropriate for use in establishing nuclear waste repositories in hard rock.

Within the room excavation at the Experimental mine, several technical tasks were undertaken in response to the needs of ONWI. This specific research task was concerned with the evaluation of the rock mass response to the excavation technique, determination of the stress field, and the rock mass modulus evaluation. Based upon the field measurements, the facility was modelled mathematically by using the finite element method. Displacements associated with the facility excavation were monitored by instruments placed in the roof and in the walls. The recorded displacements were considerably influenced by the fractured nature of the rock. Most measured displacements were movements associated with joints opening or closing. Stress measurements were made using both the CSIRO cell and the USBM borehole gage at three selected sites. Near the room

contours, an intensified stress zone was determined, while the original stress field was found to be a combination of both topographic and tectonic stresses as well as gravity. The rock mass modulus was determined by a newly-built CSM-cell that was used in NX-boreholes. The measurements were made around the room at six different sections. The modulus values were highly controlled by the pre-existing fractures in the room vicinity. A comparison revealed that average modulus values among the six sections were not significantly different. The finite element method was adopted to simulate the response of the rock mass during and after the excavation. Two types of models were developed; the first was a plane strain model, and the second was an axisymmetry model. The models predicted the elastic response of the rock mass, stresses and displacements. Model results showed that the stresses around the excavation can best be simulated by the finite element method. The displacements predicted by the model, as anticipated, were slightly smaller than the actual measurements.

TABLE OF CONTENTS

	<u>PAGE</u>
ABSTRACT.	iii
LIST OF FIGURES	ix
LIST OF TABLES.	xiii
ACKNOWLEDGMENTS	xvi
1. INTRODUCTION	
1.1 The experimental room.	1
1.2 Scope of work.	1
1.3 Work Plan.	4
2. FIELD MEASUREMENTS	
2.1 Introduction	6
2.2 Rock Mass Response	6
2.2.1 Room excavation technique	6
2.2.2 Joint analysis in the site.	8
2.2.3 Room instrumentation.	9
(I) Relative movement of the roof.	12
(II) Roof-floor convergence	23
(III) Wall-wall convergence.	28
2.3 In Situ Stress Field	35
2.3.1 Review of stress field at the mine. . .	35
2.3.2 In situ stress measurement locations. .	38
2.3.3 In situ stress measurements using the CSIRO cell.	40

	<u>PAGE</u>
2.3.4 In situ stress results based on the USBM deformation gage.	62
2.3.5 Near stress field	64
2.3.6 Influence of topography	66
2.3.7 Discussion and conclusion	67
2.4 Rock mass modulus.	71
2.4.1 Introduction.	71
2.4.2 CSM-cell.	73
2.4.3 Testing sequence and data processing.	76
2.4.4 Results	81
2.4.5 Discussion and conclusion	85
 3. FINITE ELEMENT MODELING	
3.1 Introduction	90
3.2 Model Development.	91
3.2.1 Two dimensional representation of the room models.	91
3.2.2 Modeling procedure.	92
3.2.3 Modeling analysis assumptions	94
3.3 Plane Strain Model.	97
3.3.1 Plane strain model with in situ stress loading.	97
3.3.2 Plane strain model with gravity loading.	108
3.4 Axisymmetry Model.	113
3.5 Models Validation.	128

	<u>PAGE</u>
3.5.1 Stress validation.	129
3.5.2 Displacement validation.	139
3.6 Model Application	140
4. SUMMARY AND CONCLUSION	
4.1 Summary	144
4.2 Field Measurements Conclusion	144
4.3 Modeling Conclusion	146
4.4 Recommendation for Future Work.	148
REFERENCES	150
APPENDICES	
A. Rock Properties	
A.1 Uniaxial compressive testing.	152
A.2 Biaxial compressive testing	159
A.3 Triaxial compressive testing.	164
A.4 Brazilian test.	166
B. In Situ Stress	
B.1 CSIRO data reduction program.	167
B.2 Stresses due to topography.	172
B.3 USBM borehole gage deformation measurements.	175
B.4 CSIRO strain measurements for stress calculations	177
C. CSM Cell System	
C.1 CSM cell system	190

	<u>PAGE</u>
C.2 CSM cell calibration.	191
C.3 Results - Ring No. 2 through Ring No. 6.	198
C.4 Mathematical analysis of the CSM cell system	208
C.5 Field raw data.	218

LIST OF FIGURES

<u>FIGURE</u>		<u>PAGE</u>
1.1	Location of the experimental room.	2
1.2	Surface topography of the site	3
2.1	Blast faces position at the experimental room.	7
2.2	Plan view and longitudinal section of the instrumented room	11
2.3	Extensometer No. 1	14
2.4	Extensometer No. 2	15
2.5	Extensometer No. 3	17
2.6	Extensometer No. 4	18
2.7	Extensometer No. 5	20
2.8	Roof-floor convergence recorded by stations C1, C2, and C3	24
2.9	Roof-floor convergence recorded by stations C4 and C5.	25
2.10	Roof-floor convergence recorded by stations C6 and C7.	26
2.11	Wall convergence recorded by stations R1 and R2	30
2.12	Wall convergence recorded by stations R3, R4 and R5	31
2.13	Wall convergence recorded by stations R6 and R7	32
2.14	Locations of previous stress measurements at the experimental mine.	36
2.15	Overcoring tests at the experimental mine.	39

<u>FIGURE</u>	<u>PAGE</u>
2.16 CSIRO cell components.	40
2.17 Orientation of the strain gages in the CSIRO cell.	41
2.18 Strain readings overcoring test P-2	43
2.19 Biaxial testing overcoring test P-2	45
2.20 Longitudinal section through the CSIRO cell	46
2.21 The principal stresses plotted in the lower hemisphere equal area diagram	54
2.22 The in situ stress profile (USBM gage)	63
2.23 In situ stresses and the joint sets	69
2.24 The radial boreholes location in the experimental room	72
2.25 The components of the CSM-cell system	74
2.26 Diagrammatic representation of the CSM cell	75
2.27 Pressure-volume curve for tests in the calibration aluminum cylinder, and in the borehole.	77
2.28 Rock mass modulus distribution in Ring #1	83
2.29 Rock mass modulus vs. intact rock modulus	89
2.30 Histogram representing (E_r/E) ratio.	89
3.1 Configuration of the experimental room models.	92

<u>FIGURE</u>	<u>PAGE</u>
3.2 Geology of the experimental room.	95
3.3 In situ stress loading model mesh	99
3.4 Loading condition (Case A).	100
3.5 Model loading condition (Case B).	101
3.6 Vertical stress contour plot.	103
3.7 Horizontal stress contour plot.	104
3.8 Shear stress contour plot	105
3.9 Maximum principal stress contour plot.	106
3.10 Maximum principal stress direction plot.	107
3.11 Gravity loading model mesh.	109
3.12 Model loading condition (case 4).	112
3.13 Configuration of axisymmetry model.	115
3.14 Axisymmetry model mesh.	116
3.15 Vertical stress component (measured and predicted).	130
3.16 Radial stress component (measured and predicted).	131
3.17 NX-radial boreholes configuration	141
A.1 Biaxial compression chamber	159
A.2 Triaxial test results	165
B.1 Configuration of distributed load of mountainous topography	173
C.1 CSM cell system	198
C.2 Rock mass modulus distribution in Ring #2	199

<u>FIGURE</u>		<u>PAGE</u>
C.3	Rock mass modulus distribution in Ring #3.	201
C.4	Rock mass modulus distribution in Ring #4.	203
C.5	Rock mass modulus distribution in Ring #5.	205
C.6	Rock mass modulus distribution in Ring #6.	207

LIST OF TABLES

<u>TABLE</u>		<u>PAGE</u>
2.1	Joint sets in the site.	8
2.2	Extensometers information	12
2.3	Relative movement versus face advance recorded by the roof extensometers	21
2.4	Roof-floor convergence stations information	23
2.5	Roof-floor convergence versus advance	27
2.6	Wall-wall convergence stations information	29
2.7	Wall-wall convergence versus advance	29
2.8	Review of stress measurements at the CSM Experimental Mine.	37
2.9	In situ stress measurements	38
2.10	Results of in situ stress measure- ments using the CSIRO cell.	51
2.11	Biaxial compressive testing results	57
2.12	CSM cell results in the over- coring hole	58
2.13	Laboratory testing on the over- cores samples	59
2.14	Biaxial test results (USBM gage).	60
2.15	Rock properties for stress calculation	61
2.16	Near stress field measurements.	64

<u>TABLE</u>	<u>PAGE</u>	
2.17	Rock mass modulus (Ring No. 1)	82
2.18	Averaged E_r	84
3.1	Axisymmetry model results (total convergence)	119
3.2	Axisymmetry model results (extensometer No. 1)	121
3.3	Axisymmetry model results (extensometer No. 2)	122
3.4	Axisymmetry model results (extensometer No. 3)	123
3.5	Axisymmetry model results (extensometer No. 4)	124
3.6	Axisymmetry model results (extensometer No. 5)	124
3.7	Axisymmetry model results (stresses versus depth)	127
3.8	Predicted roof-floor convergence comparable to the field measurements.	135
3.9	Predicted relative movement of the roof comparable to the field movements	136
3.10	Predicted wall-wall convergence comparable to the field measurements.	138
A.1	Uniaxial compressive test results	154
A.2	Summary of uniaxial compressive testing results	158
A.3	Biaxial test results.	161
A.4	Triaxial test results	164
A.5	Brazilian test results.	166

<u>TABLE</u>		<u>PAGE</u>
B.1	Stresses due to topography.	174
B.2	Overcoring strain reading Test H1	178
B.3	Overcoring strain reading Test T1	179
B.4	Overcoring strain reading Test T2	180
B.5	Overcoring strain reading Test T3	181
B.6	Overcoring strain reading Test T4	182
B.7	Overcoring strain reading Test T5	183
B.8	Overcoring strain reading Test T6	184
B.9	Overcoring strain reading Test P-1.	185
B.10	Overcoring strain reading Test P-2.	186
B.11	Overcoring strain reading Test P-3.	187
B.12	Overcoring strain reading Test P-4.	188
B.13	Overcoring strain reading Test P-5.	189
C.1	Rock mass modulus Ring No. 2.	198
C.2	Rock mass modulus Ring No. 3.	200
C.3	Rock mass modulus Ring No. 4.	202
C.4	Rock mass modulus Ring No. 5.	204
C.5	Rock mass modulus Ring No. 6.	206

ACKNOWLEDGMENTS

The author wishes to express his sincere appreciation to Dr. W. Hustrulid, the thesis supervisor, for his physical help, pertinent suggestions, support, and guidance in all stages of the work.

The author wishes to thank Professors George B. Clark and Robert Trent, the committee members, for reviewing the work, and Professor Robert King for his advice and encouragement. Thanks are extended to Brad Boison of Terrametrics for his technical help and advice.

I would also like to thank all my fellow graduate students, especially Falah H. Thamir, Hamid Maleki, Gideon P. Chitombo, Mike S. Ness, and Randal Barnes for their help and moral support.

Thanks are extended to the Geological and Mineral Resources Department of the Sudan, and the Sudanese Embassy in Washington, D.C., for their invaluable services and support.

Also I would like to thank Rebecca Marsh for typing my thesis.

Most of all thanks to ALLAH for everything.

1. INTRODUCTION

1.1 The Experimental Room.

The experimental room was excavated at the Colorado School of Mines experimental mine (Edgar Mine), Idaho Springs, Colorado.

The room was driven equidistant between the Miami tunnel and A-Left spur, oriented N23W, as shown in Figure 1.1. The room is 100 ft. long and of a rectangular cross section of 15 ft. wide and 10 ft. high. The gradient of the rock cover directly over the room is from 296 ft. at the room gate to 255 ft. at the end, see Figure 1.2.

The excavation took place during July through October, 1979.

1.2 Scope of Work.

The study encompassed three major objectives of equal significance; these are as follows:

a) To provide rock mass response data which included rock mass modulus distribution, and in situ stress measurements. This data was to be used within the nuclear waste investigation program.

b) To evaluate the rock mass response both during and after the excavation of the experimental room; and

c) To provide the necessary input data to develop and validate mathematical models simulating the rock mass

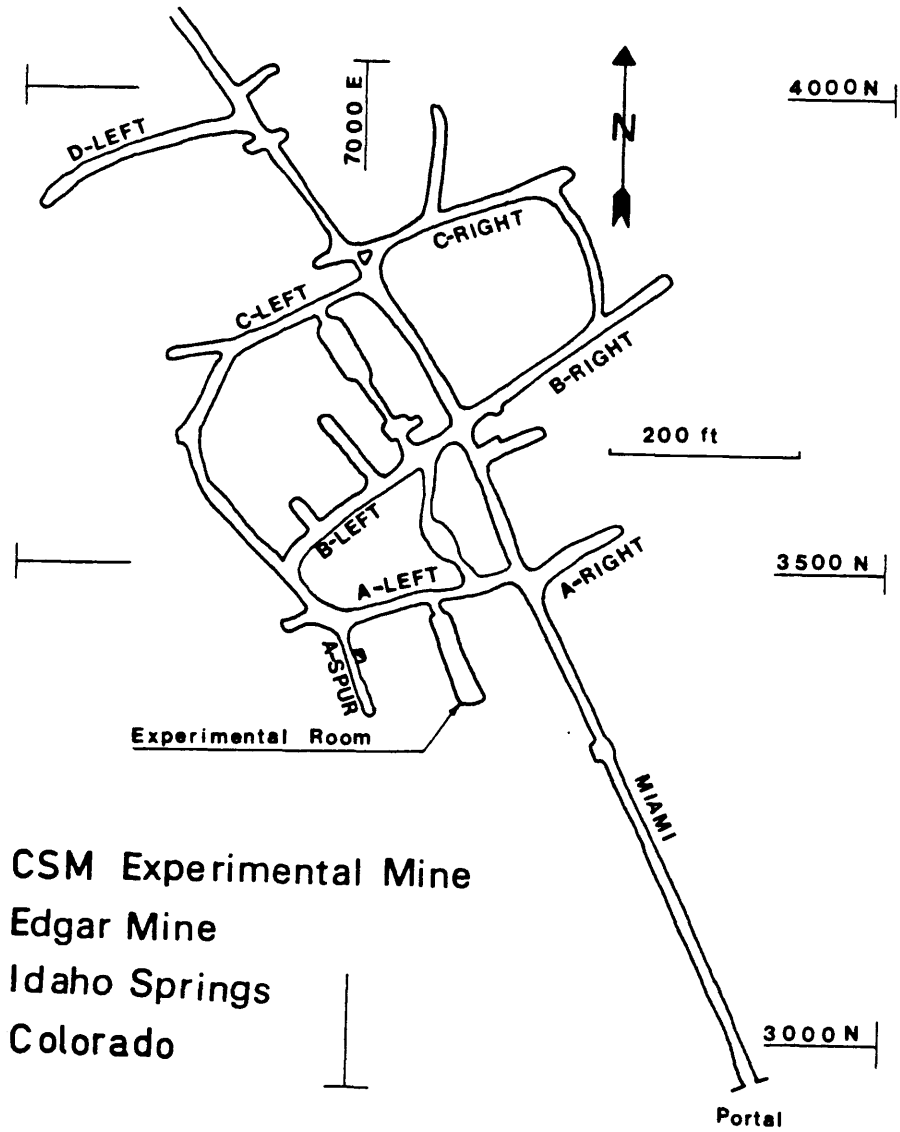


Figure 1.1 Location of the experimental room.

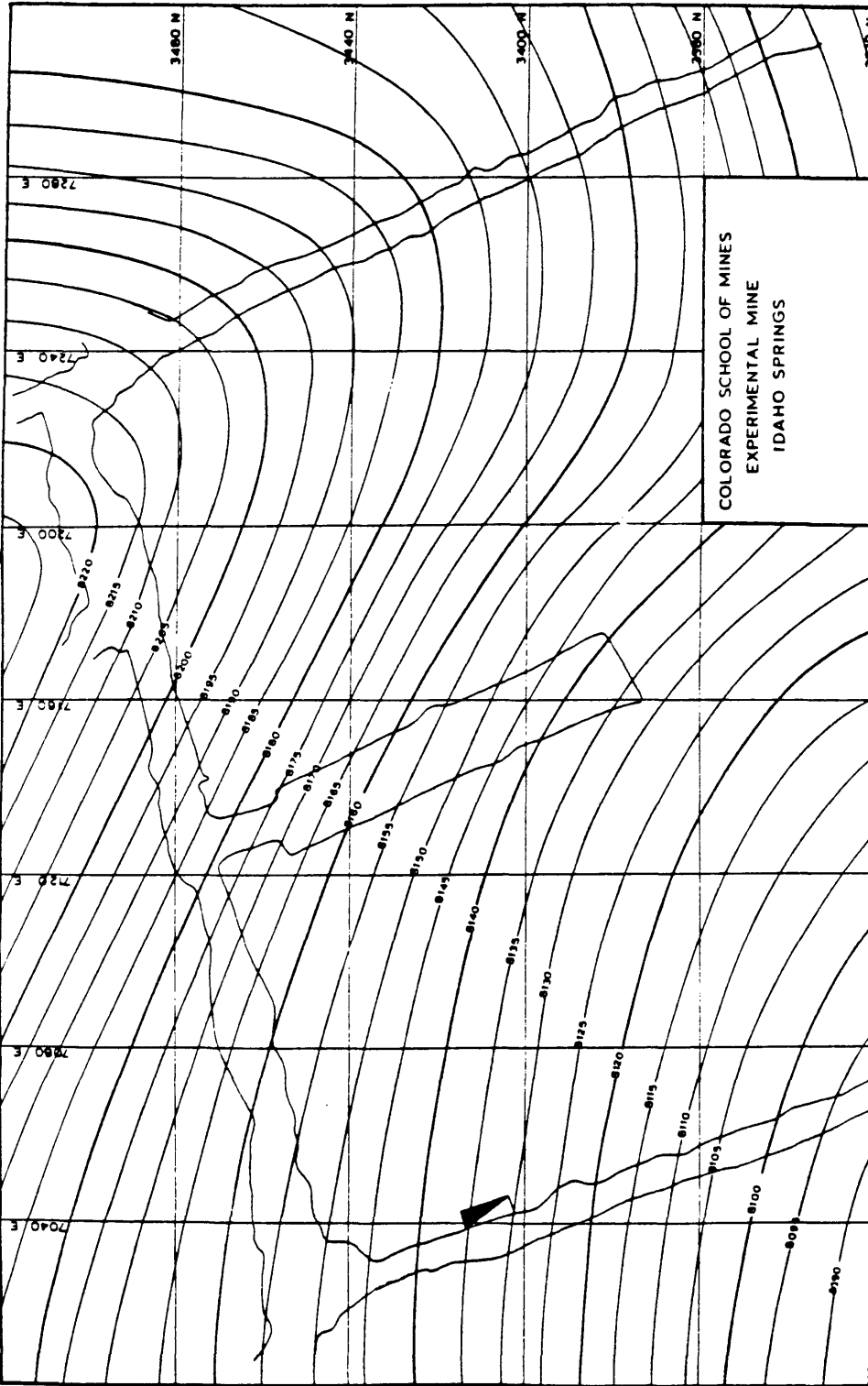


Figure 1.2 Surface topography of the site.

1.3 Work Plan.

The work plan involved two distinct phases. The first phase was the collection of field measurements at the site along with the analysis of collected data. The second phase dealt with the mathematical modeling simulating the rock mass response.

Several field measurement programs were conducted in the experimental room during and after the excavation. The measurements which were made during the excavation were of displacements exhibited by the rock mass associated with the excavation sequence. They included the following:

- a) Roof-floor convergence;
- b) Relative movement of the roof;
- c) Wall-wall convergence.

After the room was completed, other types of measurements were made to determine the following:

- a) The in situ stresses which comprised the near stress field and the in situ stress field (virgin stress).
- b) The rock mass modulus of deformation, surrounding the room.

All field Measurements, their locations, techniques, procedures, and the results are discussed in detail in Chapter 2.

The rock mass response (displacements, and stresses) was mathematically modelled by using the finite element

analysis of structural mechanics. The models were developed through the knowledge of room geometry, the sequence of excavation, the in situ stresses, and the rock mass modulus value. The validation of the models was accomplished by comparing field measurements with the corresponding results obtained from the models. The following field measurements were used for this comparison:

- a) Stress field components;
- b) Roof-floor convergence;
- c) Wall-wall convergence;
- d) Relative movement of the roof.

The level of agreement in this comparison reflects the overall level of agreement between the model results as a whole and the rock mass response both measurable and otherwise.

2. FIELD MEASUREMENTS

2.1 Introduction.

Three different major groups of measurements were made at the experimental site. These groups are given below:

a) Rock mass response measurements. These were displacements displayed by the rock mass in response to excavation. The displacements were measured during the excavation by convergence stations which were installed in the roof, floor, and the walls.

Extensometers installed in the roof measured the relative movement of the roof.

b) In situ stress field measurements. These measurements were made at different depths into the rock from the room walls after the room was completed.

c) Rock mass modulus measurements. These measurements were of the in situ elastic constant of the rock mass. They were made in boreholes drilled radially from the room.

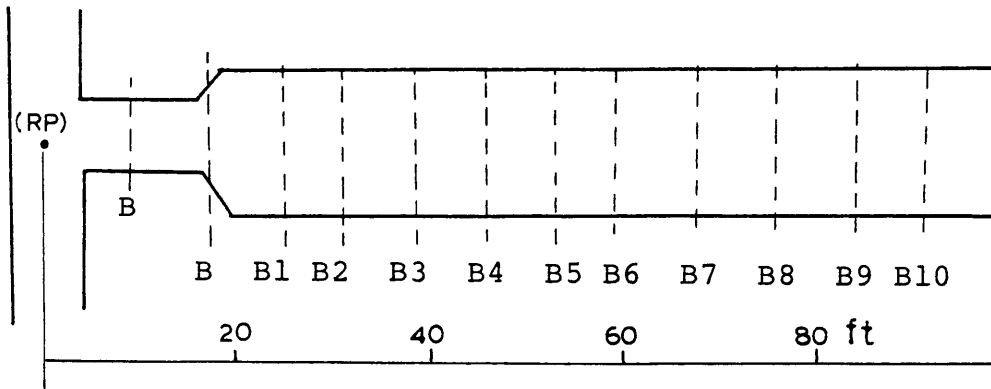
2.2 Rock Mass Response.

2.2.1 Room Excavation Technique.

The experimental room was excavated carefully using different blasting techniques. The room was driven using full face advance with an average of 7.5 ft./blast.

Ten controlled blast rounds were needed to complete the

experimental room. An average of seventy 1.5 inch boreholes were shot per round, Holmberg (1980). The position of the faces created by each blast are shown in Figure 2.



RP: Surveying spad (reference point)
 B1-B10: Controlled blasts

Figure 2.1 Blast faces position
 at the experimental
 room.

The distances between the new faces created by each blast and the reference point (RP) are as follows: (Chitombo, 1981).

<u>Blast</u>	<u>Distance of the face from (RP), ft.</u>
B 1	31.0
B 2	38.6
B 3	45.4
B 4	53.0

(continued)

<u>Blast</u>	<u>Distance of the face from (RP), ft.</u>
B 5	59.4
B 6	67.9
B 7	76.2
B 8	84.3
B 9	90.1
B10	98.1

2.2.2 Joint Analysis in the Site.

Extensive and detailed mapping of the joints was carried out in the vicinity of the experimental room. Joint mapping was performed on the walls, the roof, faces prior to each blast, and in surrounding drifts. This structural data has suggested eleven different sets of joints, Rosasco, (1981).

Table 2.1 shows the parameters of each set.

Table 2.1 Joint Sets in the Site.

Set	Strike	Dip	Mean Spacing(cm)
1	N56E	83NW	40.6
2	N73E	70NW	32.5
3	N72E	82SE	83.3
4	N83E	75NW	48.3
5	N81E	62NW	-
6	N63W	84NE	45.3
7	N41N	86SW	58.5
8	N33E	58SE	32.5
9	N51W	63NE	-
10	N80E	48SE	13
11	N21W	32NE	10

The data from 268 different joints were used to construct the above table. The weighted average joint spacing at the site was calculated as 17.3 in. (44 cm), Rosas (1981). Besides the joints, the room was also intersected by a shear zone which was dipping vertically with a bearing of N45E.

2.2.3 Room Instrumentation.

Monitoring the total displacement of the rock mass associated with room excavation requires that the instrumentation be installed prior to room excavation. However, in this case, the installation of monitoring instruments, prior to excavation was not practical because of the extreme distances involved. The nearest tunnels (Miami and A-Left spur), see Figure 1.1, were 100 ft. away from both sides, and the distance to the surface was above 300 ft. As a result of the above limitation, the instruments were placed only during the room excavation as the face advanced. The distances between the instruments and the face at installation time was controlled by the excavation scheduling and the blast throw. The following displacement monitoring instruments were installed.

- (I) Five multiple position borehole extensometers
- (II) Seven roof-floor convergence stations
- (III) Seven wall-wall convergence stations

Figure 2.2 shows the locations of these instruments, and the major structural features of the room.

The recorded displacements by the instruments were those occurring after each installation; i.e. no displacements were recorded prior to instrument installation. Thus, the absence of some data is explained. This unrecorded data could be predicted by the mathematical model as described in Chapter 3.

The readings from the instruments were precluded by the presence of mining equipment, water, and the muck at various periods during the excavation of the room; nevertheless, sufficient data was collected for the analysis.

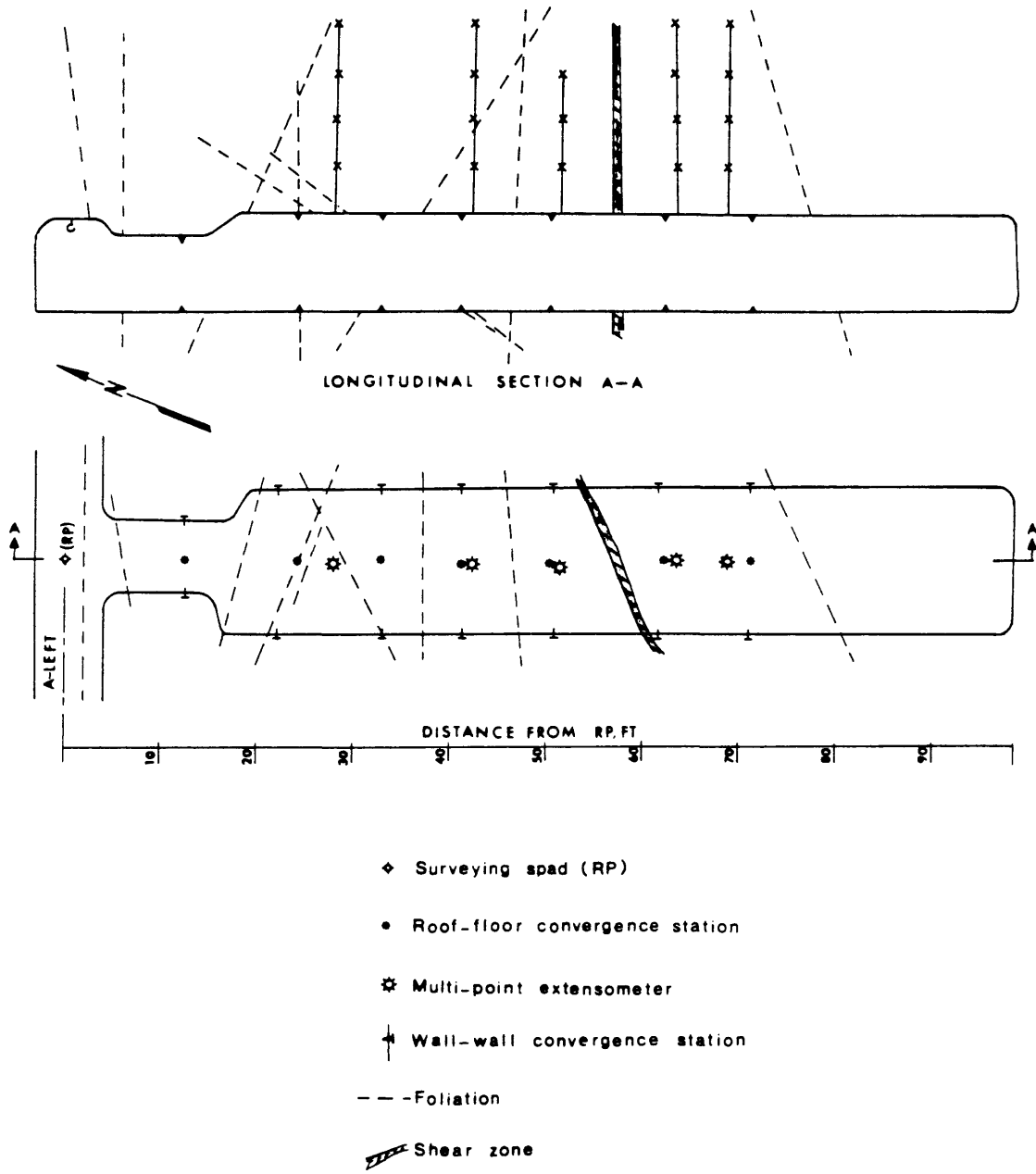


Figure 2.2 Plan view and longitudinal section of the instrumented room.

(I) Relative Movement of the Roof.

Five multiple position borehole extensometers were installed along the centerline of the roof in 1 3/4 in. diameter boreholes. The extensometers were RMC model manufactured by Irad Gage, Inc. with mechanical anchoring capability and sonic probe readout meter. Each extensometer incorporates five anchors at depths of 0, 5, 10, 15, and 20 ft. The surface anchor (zero depth) had a built-in anchor for calibra-

The deepest anchor was intended to be installed at 30 ft., but considerable difficulty in cleaning out the drill cuttings was encountered for depth of more than 22 ft. due to water pressure losses. Hence, the deepest anchor position came at 20 ft. Table 2.2 gives full information about each extensometer.

Table 2.2 Extensometers Information

Ext. No.	Date of Installation	Distance from R.P.#	Anchor Depths Ft.	Face Position From R.P. Ft.
1	8/ 4/79	28	5,10,15,20	38.6
2	8/16/79	42.5	5,10,15,20	53.0
3	8/31/79	51.1	5,10,15	67.9*
4	8/31/79	63.6	5,10,15,20	67.9
5	9/17/79	68.7	5,10,15,20	76.2

#RP: Reference Point, see Figure 2.1

*: Difficulties were encountered in installing the deepest (20 ft.) anchor.

Extensometers Output

The measurements recorded by the extensometers during the excavation can be best presented graphically. These graphs show the movement of the shallower anchors of the extensometers relative to the deepest anchor. The (-) movement or rise indicates that the distance between the given anchor and the deepest anchor has decreased. But, if the distances between the given anchor and the deepest anchor increases, then (+) movement or sagging has occurred.

Extensometer No. 1

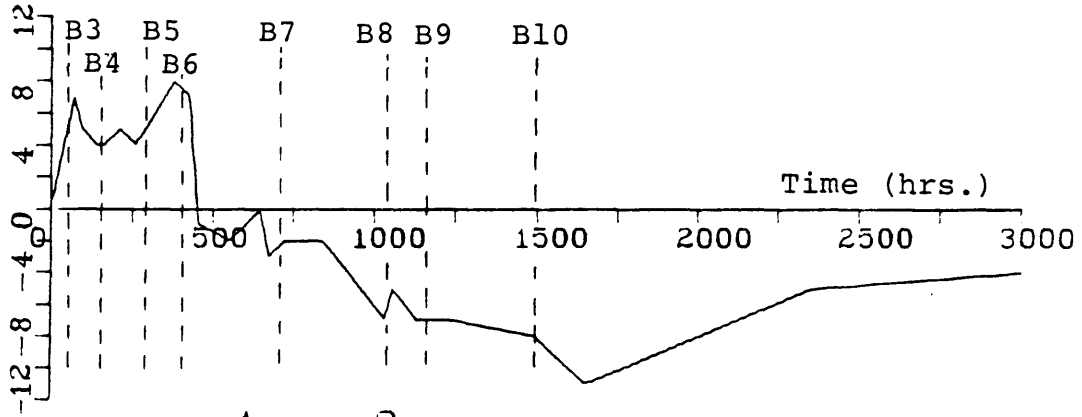
This extensometer was installed in its entirety. The relative movement recorded by this extensometer is shown in Figure 2.3. The measurements show that sagging took place during the early face advance B3, B4, B5, and B6. After that, the movement became variable and could not be explained as an elastic rock response.

Extensometer No. 2

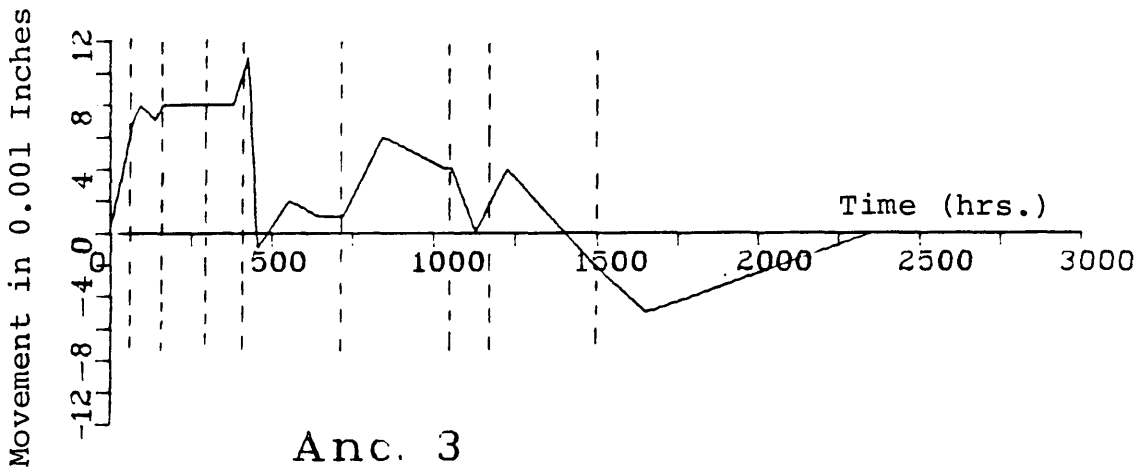
This extensometer was installed completely with four anchors. Only a few days later, it became evident that the anchors at 10 and 20 ft. positions had not been set properly. Therefore, the data collected only represented the movement of the anchor at the 5 ft. position relative to the anchor at

EXTENSOMETER NO. 1

Anc. 1



Anc. 2



Anc. 3

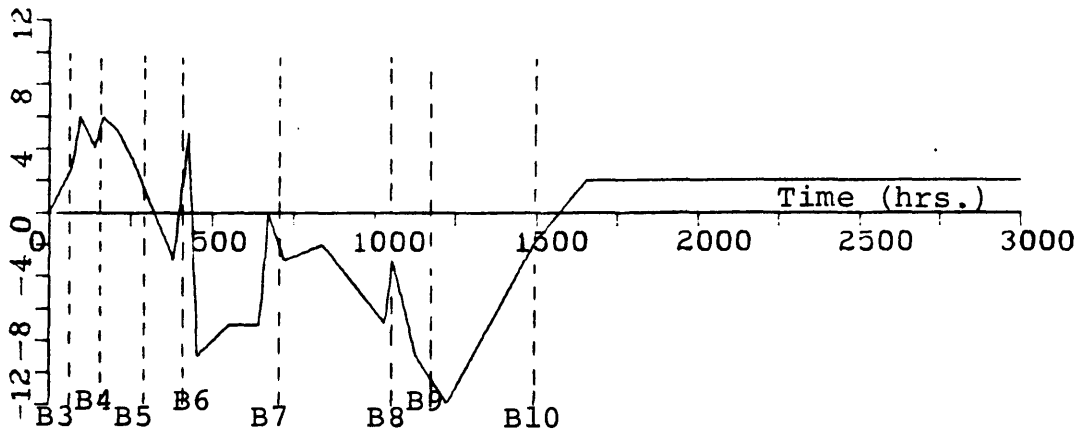


Figure 2.3 Extensometer No. 1

EXTENSOMETER NO. 2 Anc. 1

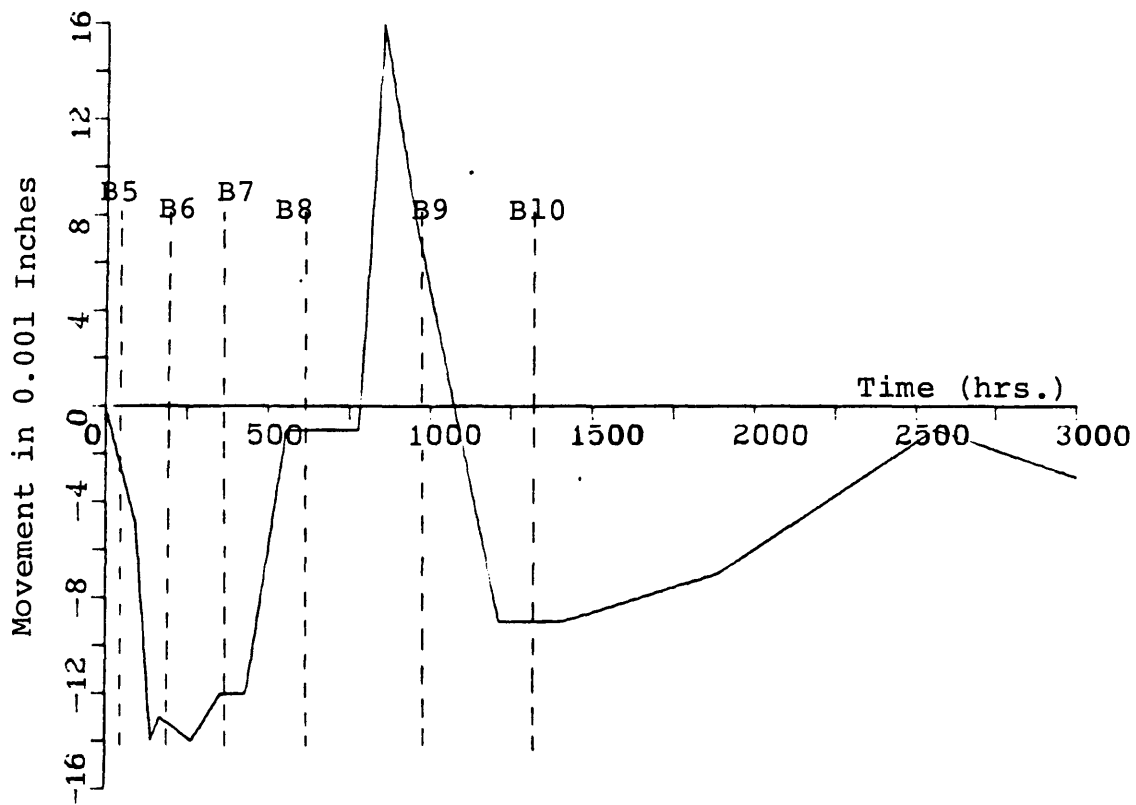


Figure 2.4 Extensometer No. 2

the 15 ft. position. Figure 2.4 shows the output from this extensometer during the excavation. No useful information can be drawn from this extensometer, since only one anchor output was recorded and the relative movement displayed no obvious attitude.

Extensometer No. 3

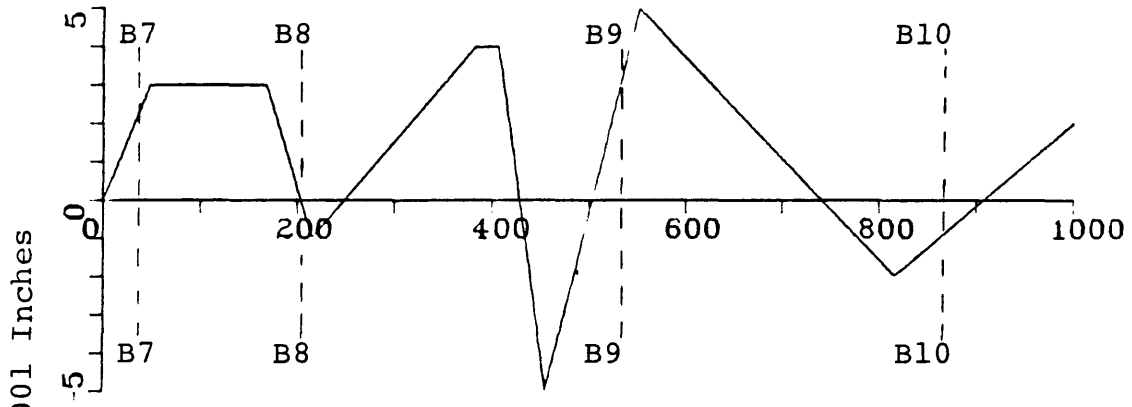
It was installed with three anchors at 5, 10, 15 ft. depths. The movement of anchor 1 (5 ft. position) and 2 (10 ft. position) was related to the 15 ft. anchor and is shown in Figure 2.5. The movement of anchor 1 varied between rise and sag during the excavation. Figure 2.5 indicates that the movement of this anchor can be averaged to zero. Anchor 2 had shown the tendency to rise after the third blast. This extensometer was installed about 17 ft. away from the face; thereby not in position to record earlier face advancements.

Extensometer No. 4

No problems were encountered in installing this extensometer. Figure 2.6 shows the movement recorded by this extensometer. This extensometer was located on the (beyond) shear zone in the room. Sagging was noted by anchor 1 and 2 during the early advance. Anchor 3 (15 ft.) had relative movement upward during the excavation.

EXTENSOMETER NO. 3

Anc. 1



Anc. 2

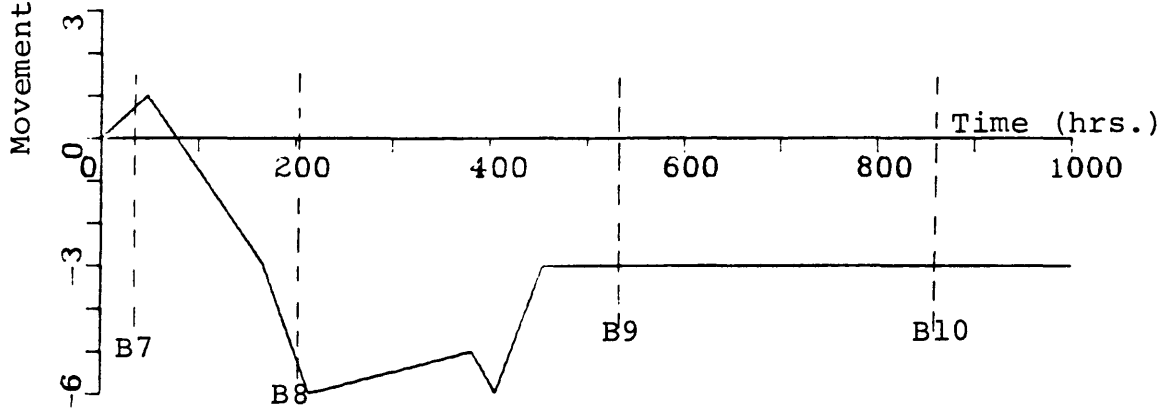


Figure 2.5 Extensometer No. 3

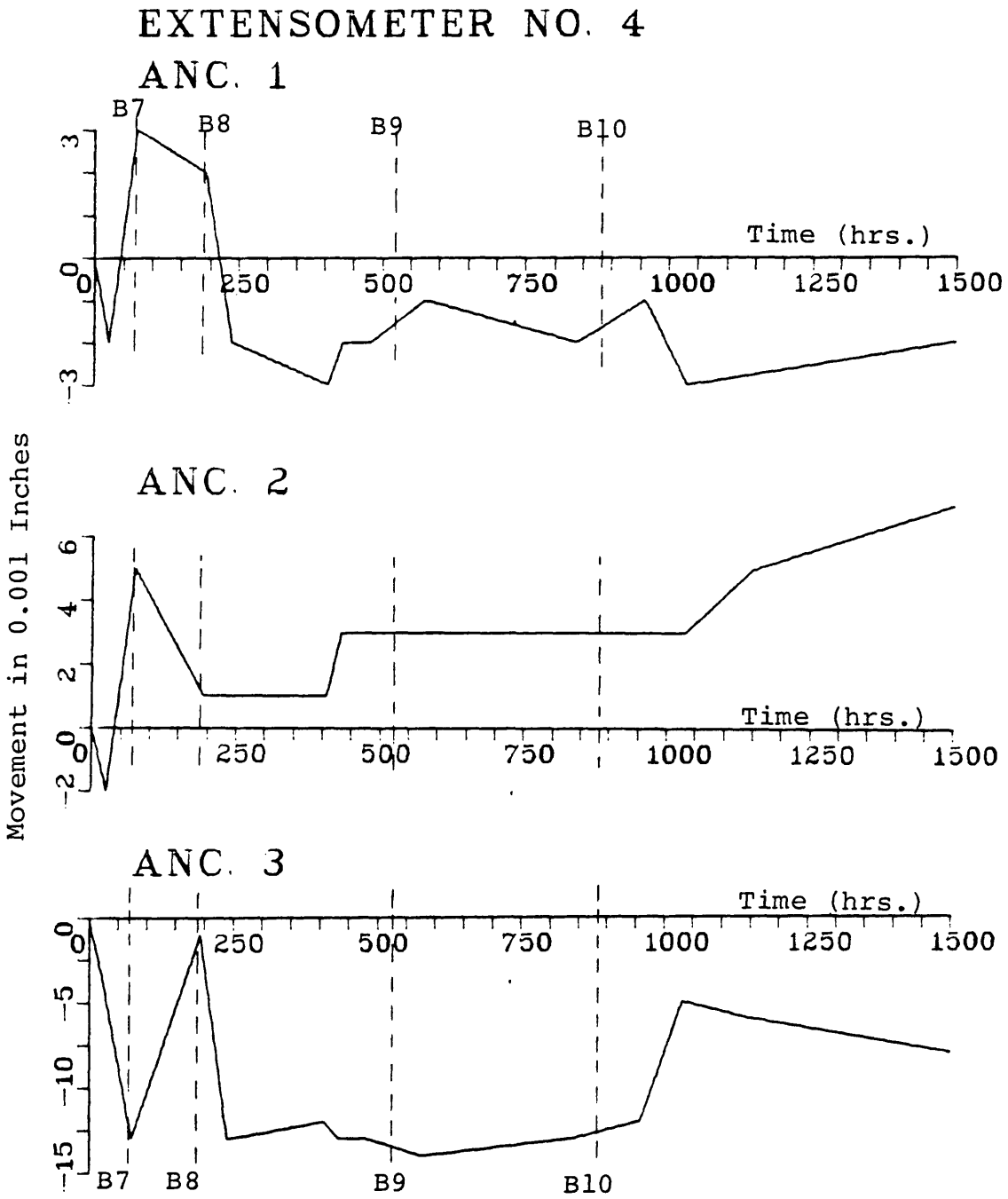


Figure 2.6 Extensometer No. 4

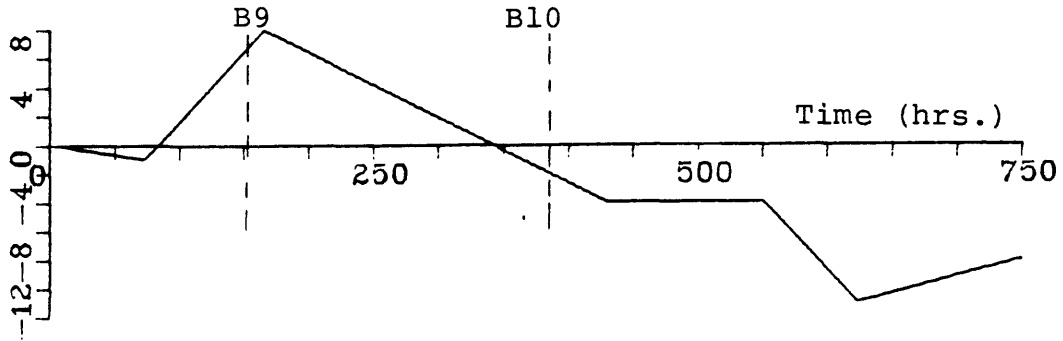
Extensometer No. 5

It was completely installed having four anchors. The relative movements of the shallower anchors to the deepest anchor at 20 ft. position are shown in Figure 2.7. The extensometer was also installed at the other side of the shear zone. The instrument was not implaced until after two face advances, and there were two more face advances following its installation. The relative movement of anchors 1 and 3 were variable during the advance. Anchor 2 showed sagging after B9 and B10.

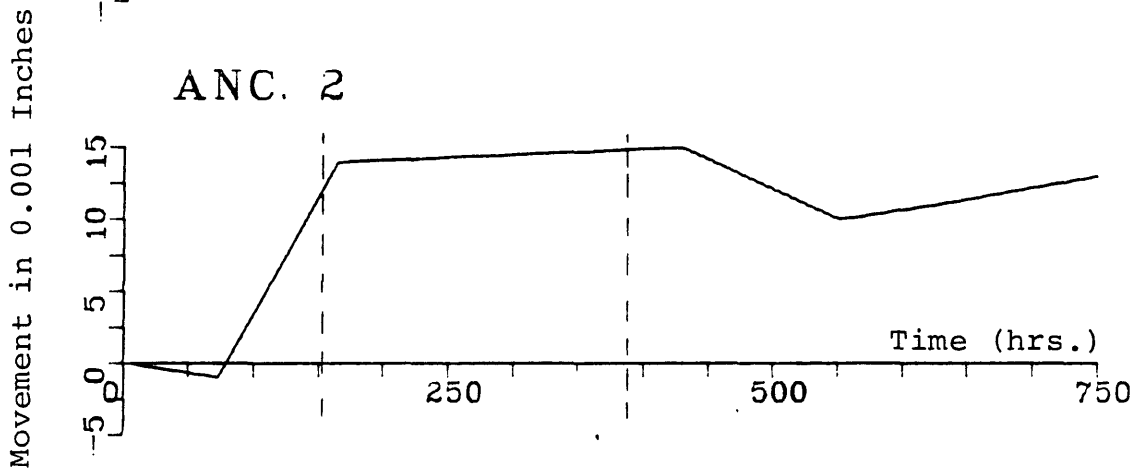
The relative movement of the shallower anchors to the deepest anchor recorded by all extensometers are summarized in Table 2.3.

EXTESOMETER NO.5

ANC. 1



ANC. 2



ANC. 3

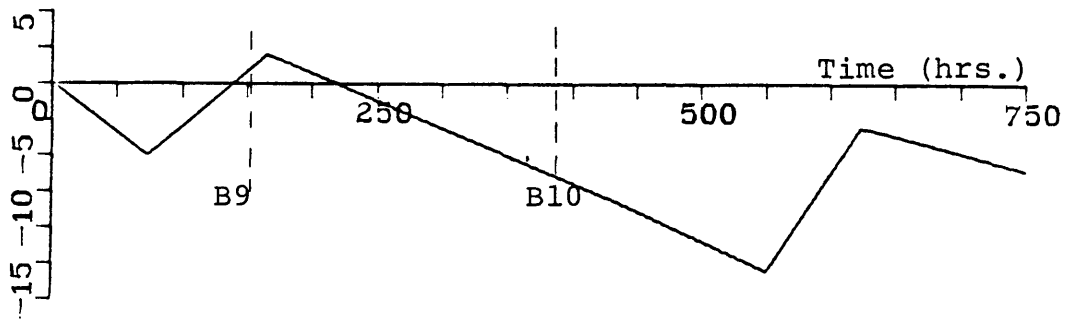


Figure 2.7 Extensometer No. 5

Table 2.3 Relative Movement Versus Face Advance
Recorded by the Roof Extensometers
(movement x 10^{-3} inches)

Extensometer No. 1											28' from (RP)
Anchor	B1	B2	B3	B4	B5	B6	B7	B8	B9	B10	
	31'	38.6'	45.4'	53.'	59.4'	67.9'	76.2'	84.3'	90.1'	98.1'	
1	-	-	4	5	7	-2	-6	-6	- 7	-8	
2	-	-	7	8	8	11	1	4	2	-2	
3	-	-	6	6	-1	5	-3	-4	-10	-2	
Extensometer No. 2											42.5' from (RP)
1	-	-	-	-	-2	-14	-12	-2	- 8	-8	
Extensometer No. 3											51.1' from (RP)
1	-	-	-	-	-	-	3	0	5	3	
2	-	-	-	-	-	-	1	-6	- 3	-3	
Extensometer No. 4											63.6' from (RP)
1	-	-	-	-	-	-	3	2	- 1	- 1	
2	-	-	-	-	-	-	1	1	3	3	
3	-	-	-	-	-	-	-13	-1	-14	-13	
Extensometer No. 5											68.7' from (RP)
1	-	-	-	-	-	-	-	-	8	-4	
2	-	-	-	-	-	-	-	-	14	15	
3	-	-	-	-	-	-	-	-	2	-8	

It can be concluded from the extensometers' data that the movements recorded by the extensometers are small and they displayed no clear relationship between the different anchors nor between each other. This can be attributed to a) the extensometers were not installed early enough to monitor the early elastic behavior of the roof; b) the assumption of taking the deepest anchor at 15 or 20 ft. position as fixed position and relate other anchor's movement to that anchor base is not supported by the model results (Chapter 3), since the model had suggested that these positions would sag 0.006 ± 0.001 inches; c) the fractured nature of the rock has affected the movement of the anchors considerably; d) small displacements are difficult to be monitored by such extensometers.

Furthermore, the extensometers' data did not show any remarkable difference between the displacements of the roof on both sides of the shear zone.

(II) Roof-floor Convergence.

Seven roof-floor convergence stations were installed in the experimental room during the excavation. The locations and other information for these stations are given in Table 2.4. The stations were made of 7/8 in. diameter rock bolts with acorn nuts welded on the head. The bolts were fully grouted into 1 5/8 in. diameter boreholes of an average depth of two ft. Both the Soil Test convergence meter and Irad convergence meter were used to measure the distance between the roof and the floor during the excavation.

Table 2.4 Roof-Floor Convergence Stations Information.

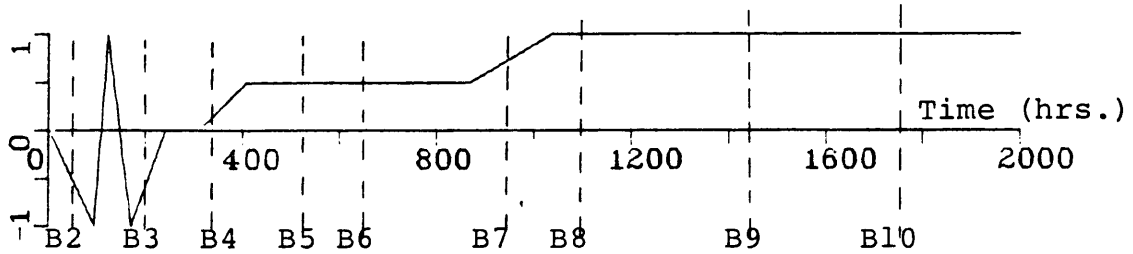
Station No.	Date of Installation	Distance From R.P.	Face Position
C1	7/29/79	12.4	25.2
C2	8/ 2/79	24.3	38.6
C3	8/ 5/79	33.0	38.6
C4	8/ 8/79	41.2	45.4
C5	8/31/79	50.6	67.9
C6	8/31/79	62.6	67.9
C7	9/18/79	71.5	84.3

The convergence between the roof and the floor recorded by these stations are shown in Figure 2.8 to Figure 2.10.

Table 2.5 summarizes the roof-floor convergence readings after each face advance during the excavation.

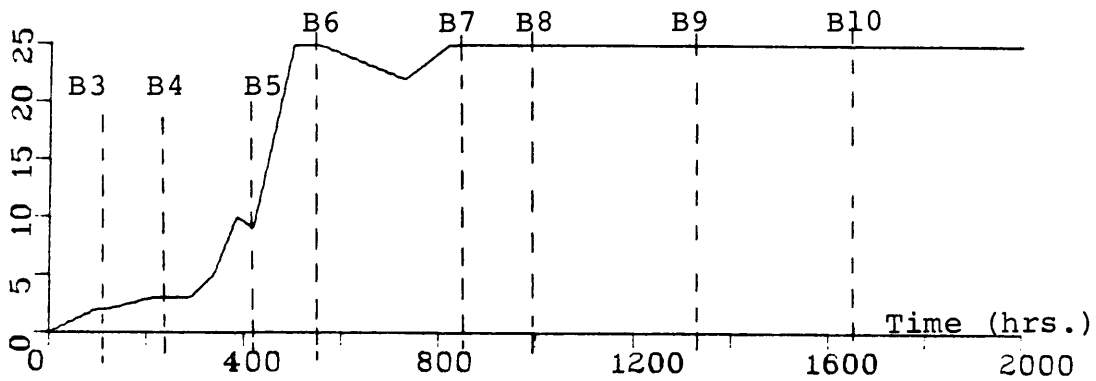
ROOF FLOOR CONVERGENCE

Station No.1



Movement in 0.001 Inches

Station No.2



Station No.3

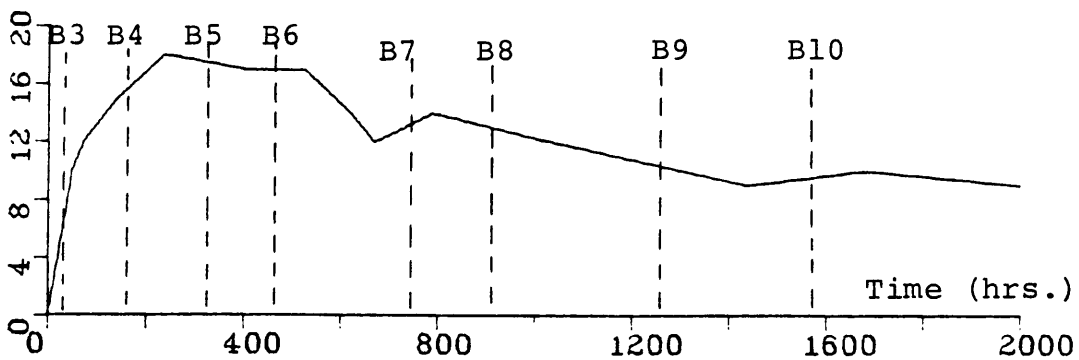
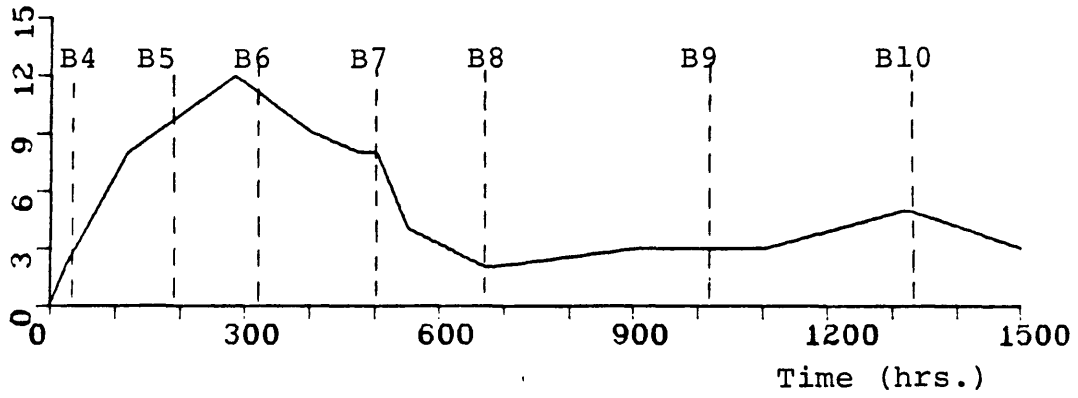


Figure 2.8 Roof-floor convergence recorded by stations C1, C2 and C3.

Station No.4



Station No.5

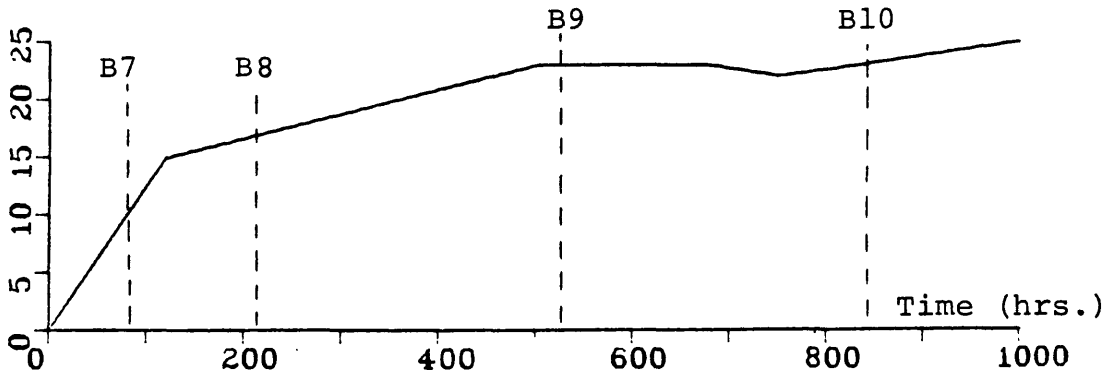


Figure 2.9 Roof-floor convergence recorded by stations C4 and C5.

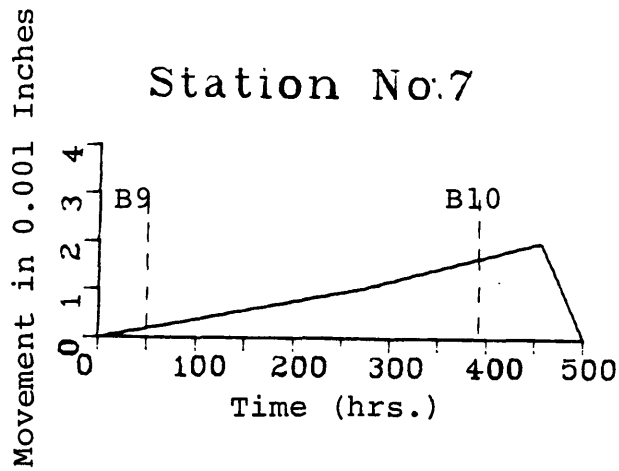
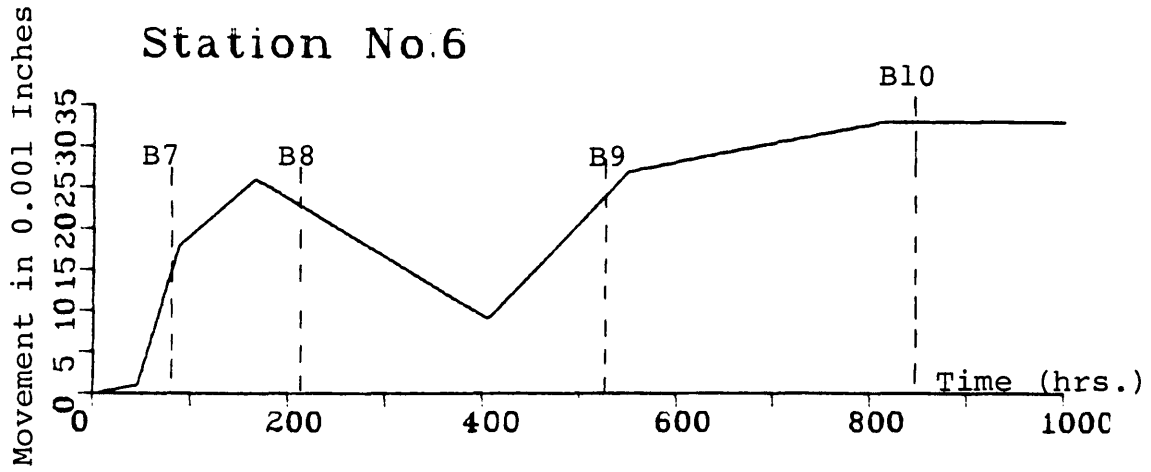


Figure 2.10 Roof-floor convergence recorded by stations C6 and C7.

Table 2.5 Roof-Floor Convergence Versus Advance.(Convergence x 10^{-3} inches)

Station	B1	B2	B3	B4	B5	B6	B7	B8	B9	B10
R1	5	-15	16	2	2	0	3	-1	-4	-5
R2	-	7	16	20	1	2	4	3	5	9
R3	-	-	12	5	8	0	10	5	-6	-2
R4	-	-	-	2	3	13	10	9	11	10
R5	-	-	-	-	-	-3	30	25	10	10
R6	-	-	-	-	-	-	-4	2	2	0
R7	-	-	-	-	-	-	-	-	2	0

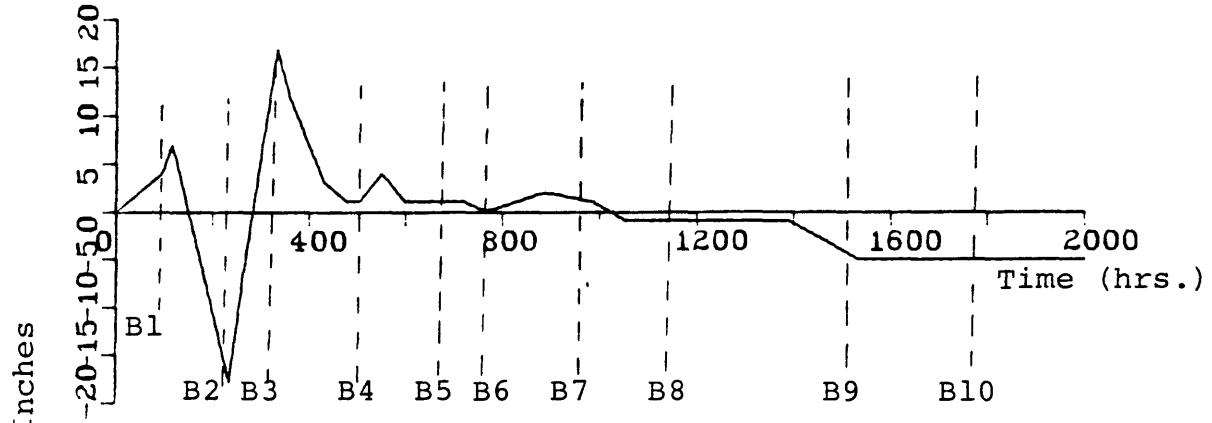
The convergence measurements have shown that the roof-floor closure had taken place in all locations. The convergence magnitudes were different and the minimum displayed by C1 and C7 station. Most measurements revealed that the closure increases during the early advance of the face, but they did not reflect any great roof movement or instability of the roof. Station C2 might reflect the opening of small fractures due to blast B5 and stopped by B6. Stations C3 and C4 displayed similar attitude during the excavation period. Stations C5 and C6 have recorded comparable readings even though they were on different sides of the shear zone. Station C7 has undergone two blasts which seemed to have no significant effect on the station's position, and the movement was missed to be recorded by the

station due to late installation (see Table 2.1). Generally the displacements recorded by C2 to C6 are considered to be highly comparable to those which can be predicted by mathematical model, Chapter 3. It should be mentioned that the model has predicted that the most closure occurs during the next three face advances from the instrument location, so that the convergence recorded by the stations were a combination of elastic and non-elastic movement of the roof and/or the floor, especially the floor since the blasting charges were heavier in the lifters.

III. Wall-Wall Convergence.

Seven wall-wall convergence stations were installed within the first three ft. of the room walls. Rock bolts 7/8 in. in diameter were used, with suitable size of eye-bolts screwed into the head to accommodate the measuring device. Terrametrics tape extensometer was used to measure the wall convergence. Table 2.6 gives the location and other information about these convergence stations.

WALL CONVERGENCE Station No.1



Station No.2

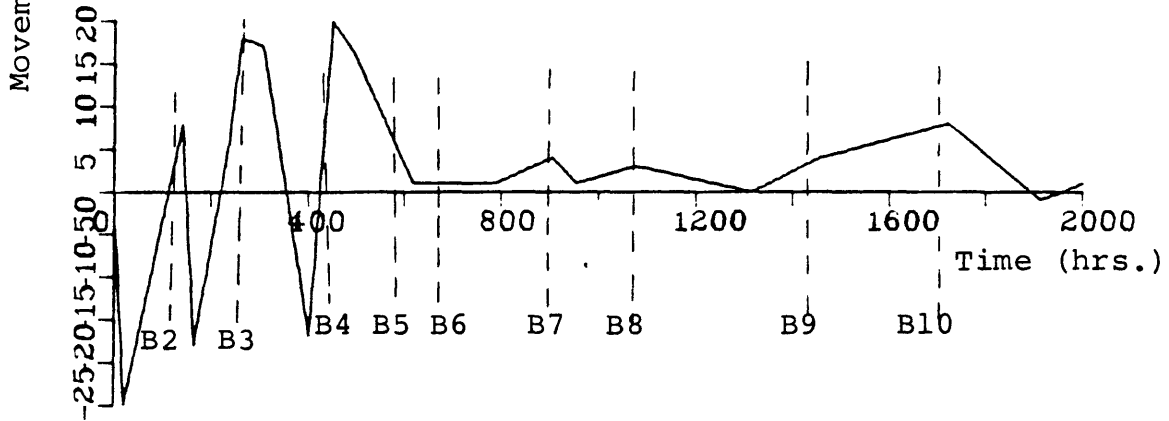
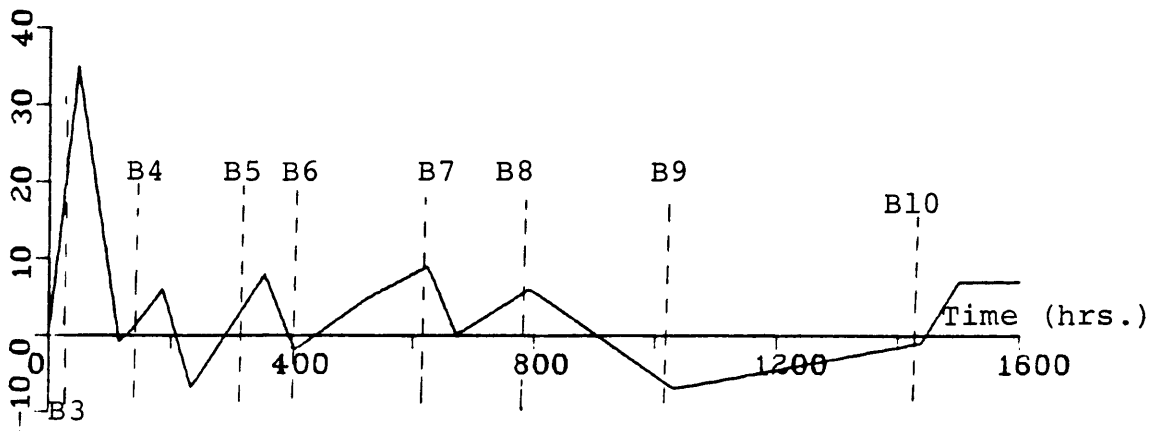
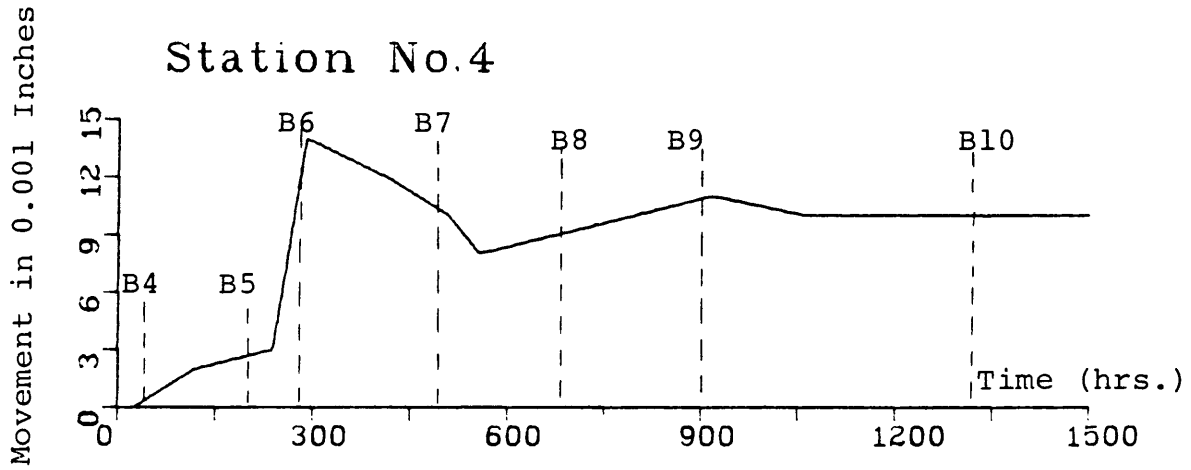


Figure 2.11 Wall convergence recorded by stations R1 and R2.

Station No.3



Station No.4



Station No.5

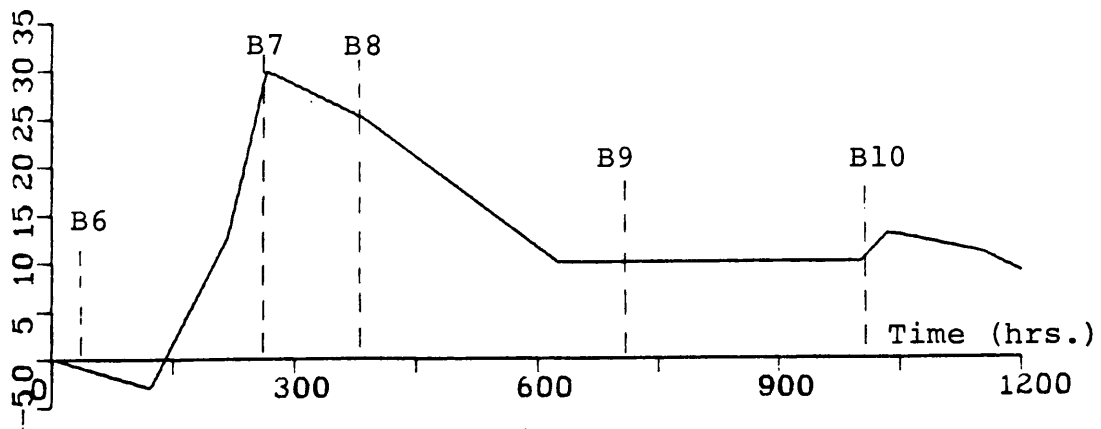


Figure 2.12 Wall convergence recorded by stations R3, R4 and R5.

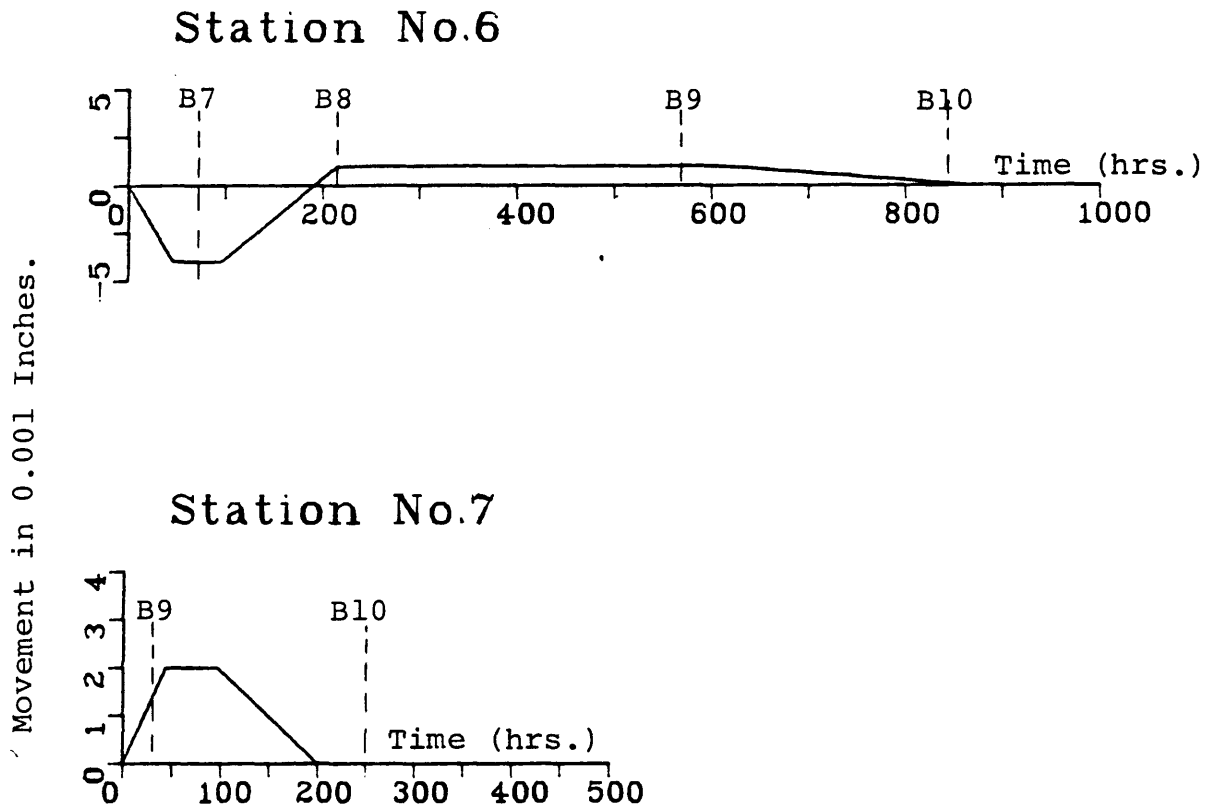


Figure 2.13 Wall convergence recorded by stations R6 and R7.

Wall convergence measurements have displayed variable modes of movements during the course of excavation. Most wall convergence stations showed that the closure between the walls have taken place. The divergence between the walls or the (-) movements in the Figures cannot be explained as an elastic response of the room walls. Stations R1, R2 and R3 were fluctuating during the early face advancements, and they seemed to stabilize after four blasts. Stations R4 and R5 recorded a comparable measurement after they experienced the first three blasts. Convergence recorded by stations R6 and R7 were small during the excavation, and then vanished.

High readings were noticed during the excavation time which could be related to the blasting shocks.

The general conclusion which can be drawn from all displacements measurements are as follows:

a) The displacements occurred during the excavation were variable, and controlled by the structural features of the rock mass.

b) The late installation of the instrumentation has led to missing of some useful data which could have reflected the early behavior of the rock mass.

c) The recorded displacements and convergence data has reflected the stability of rock mass at the experimental room.

d) Deformations recorded by instruments on both sides of the shear zone did not show any obvious difference in the rock behavior on both sides of that zone.

2.3 In Situ Stress Field

2.3.1 Review of Stress Field at the Mine.

CSM-Experimental mine had undergone several in situ stress measurements at different sites, in different periods of time.

Stress relief overcoring was the adopted technique for these measurements, using different types of gages. A review of those measurements are listed in Table 2.8, and the location of these tests are shown in Figure 2.14 combined with the major structural features of the mine.

Stress orientation on the area has been investigated by Moench and Drake (1966), who suggested, on the basis of data on faults, joints, and veins, that the stress field was compressive and was oriented N-NE in early Tertiary. Later in Tertiary time the region was subjected to tensional stress also oriented N-NE. "Further investigation by Moench (1974) concerning the youngest fault movements suggesting that trend north-northwest, appropriate for σ_1 oriented about N12W, and σ_3 about N78E (both presumably horizontal)", Lee, et al. (1976).

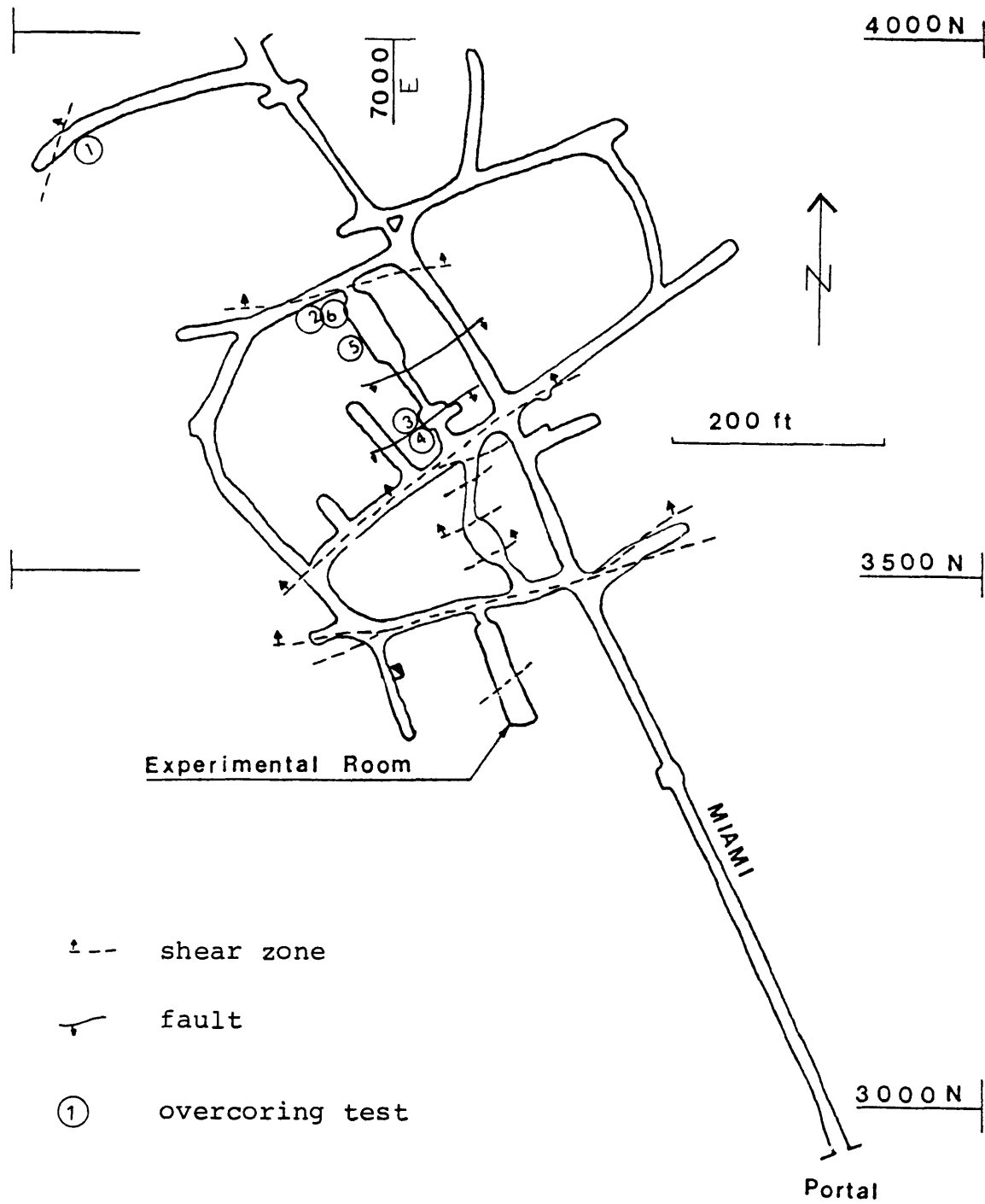


Figure 2.14 Locations of previous stress measurements at the experimental mine.

Table 2.8 Review of Stress Measurements at CSM Experimental Mine.

Investigator	Gage Used	Results Concluded by the Investigator	Location on Map
Wentworth (1962)	USBM Gage	Hole 1: bearing S 50.5 W p=400 psi, Q=50 psi, $\theta=41^\circ$	1
		Hole 2: bearing S 8.0 W p=500 psi, Q=330 psi, $\theta=35^\circ$ $\sigma_H > \sigma_v$	
USGS (3/1968)	USGS Probe	$\sigma_1 = 1440$ psi, bearing S74E, plunge 53° $\sigma_2 = 1045$ psi, bearing N0.0E, plunge 10° $\sigma_3 = 510$ psi, bearing S86W, plunge 35° $\sigma_H = \sigma_v$	2
USGS (3/1968)	USGS Probe	$\sigma_1 = 1805$ psi, bearing N47E, plunge 20° $\sigma_2 = 1225$ psi, bearing S16E, plunge 51° $\sigma_3 = 690$ psi, bearing N56W, plunge 32° $\sigma_H = 1.33 \sigma_v$	3
USGS (5/1968)	USGS Probe	$\sigma_1 = 620$ psi, N68E, plunge 16° $\sigma_2 = 515$ psi, S27E, plunge 17° $\sigma_3 = 420$ psi, N62W, plunge 66° $\sigma_H = 1.1 \sigma_v$	4
Cox (1967)	USBM Gage	P = 1250 psi, Q=500 psi, $\theta=37^\circ$ $\sigma_H = 1.25 \sigma_v$	5
	USGS Probe	$\sigma_1 = 1250$ psi, N45.8W, 38° $\sigma_2 = 869$ psi, N65.8W, plunge 20° $\sigma_3 = 1417$ psi, S77E, plunge 45.3° $\sigma_H = 1.15 \sigma_v$	6

θ : The angle measured from the vertical to P in the counterclockwise direction.

2.3.2 In Situ Stress Measurement Locations.

The in situ stress field in the vicinity of the experimental room was measured in three parallel holes. The holes were 5 ft. apart, horizontal, and perpendicular to the room axis, S67W. The tested holes were carefully located at the middle section of the room, and 5.5 ft. above the room floor. Stress relief overcoring technique was adopted using both the USBM deformation gage and CSIRO cell. Table 2.9 shows the number of tests per hole, and is shown in Figure 2.15.

The results associated with the use of USBM gage were presented in detail in another report, Tadolini (1981): however, the final conclusions are used in this analysis with the CSIRO cell results.

Table 2.9 In Situ Stress Measurements.

Hole No.	Distance (ft.) From the Gate (RP)	Gage	Number of Tests	Maximum Hole Depth (ft.)
1	54	CSIRO USBM	1 5	16
2	49	CSIRO	6	26.9
3	44	CSIRO USBM	5 17	30

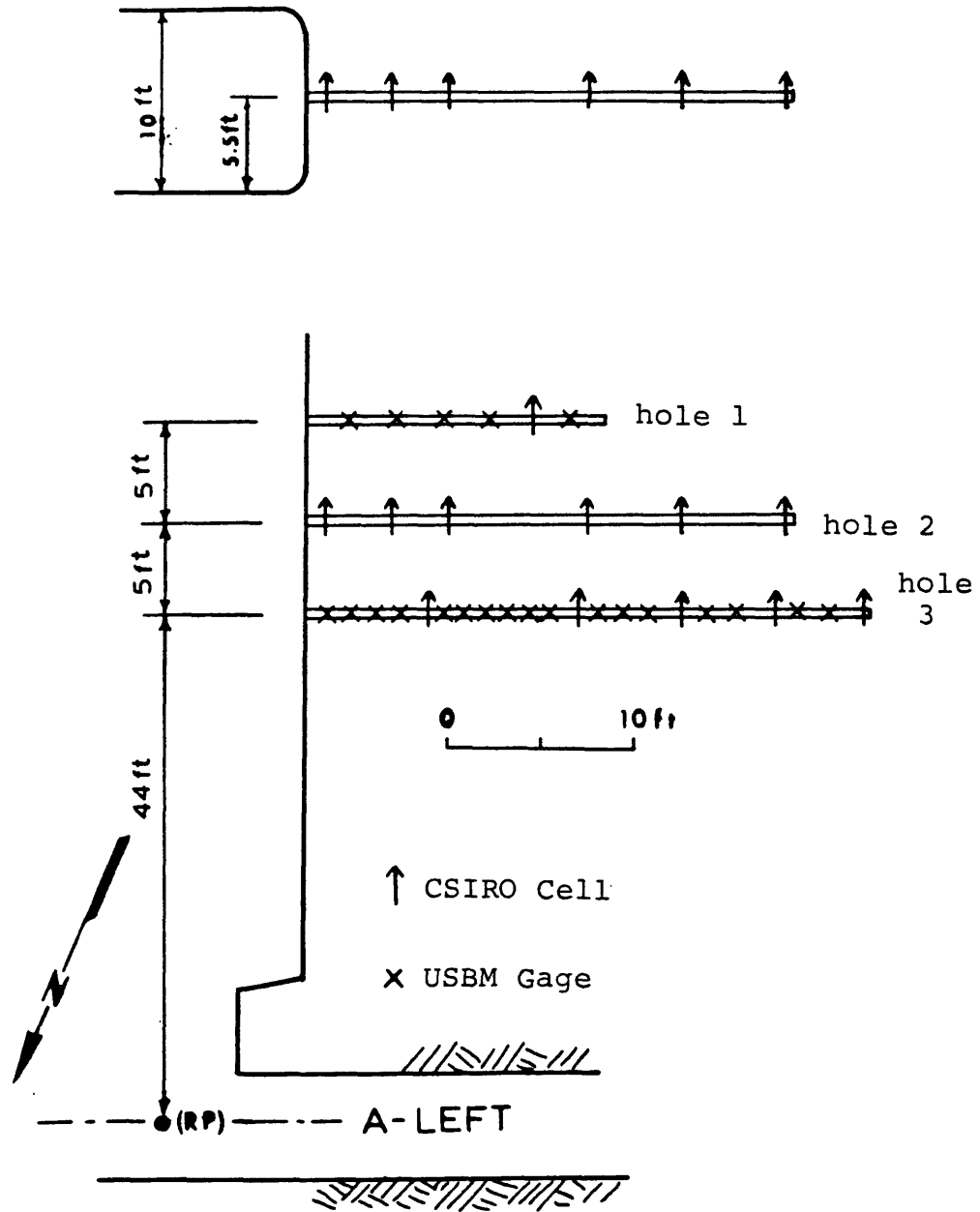


Figure 2.15 Overcoring tests at the experimental room.

2.3.3 In Situ Stress Measurements Using CSIRO Cell.

CSIRO Cell Design.

CSIRO "hollow inclusion cell" was used to monitor the borehole wall deformation produced by the overcoring process. The cell is a thin walled pipe made of epoxy plastic, having 32mm I.D., 36mm O.D., which closely fits an Ex-borehole. It is cemented in place using a special Araldite mixture recommended by the manufacturer for different temperatures. The different components of the cell are shown in Figure 2.16.

The cell incorporates nine strain gages in three rosettes. These rosettes are spaced at 120° within the cell shell. There are two strain gages to monitor the axial deformation, three strain gages for the circumferential

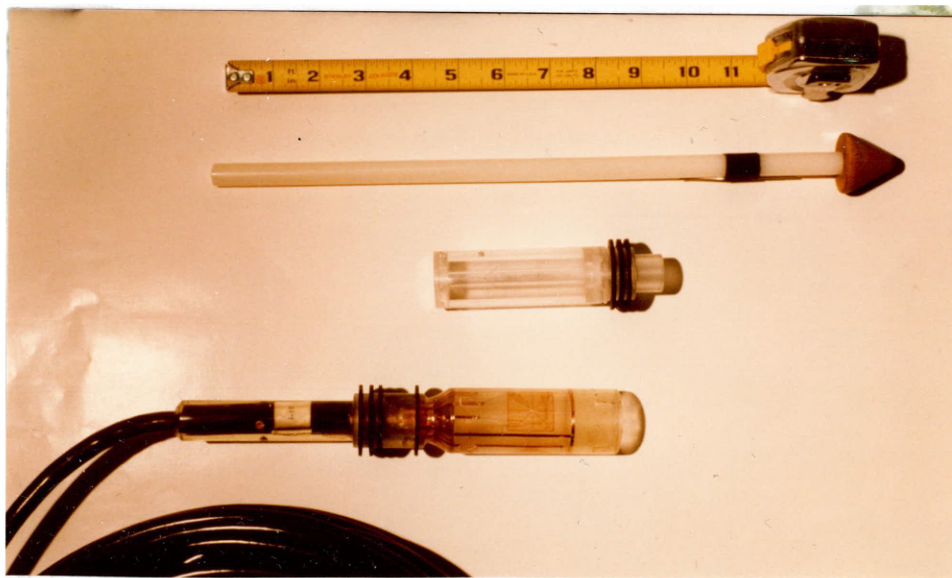


Figure 2.16 CSIRO cell components

deformation, and four gages at $\pm 45^\circ$ to the axis of the borehole. The orientation of the strain gages in the cell is shown in Figure 2.17.

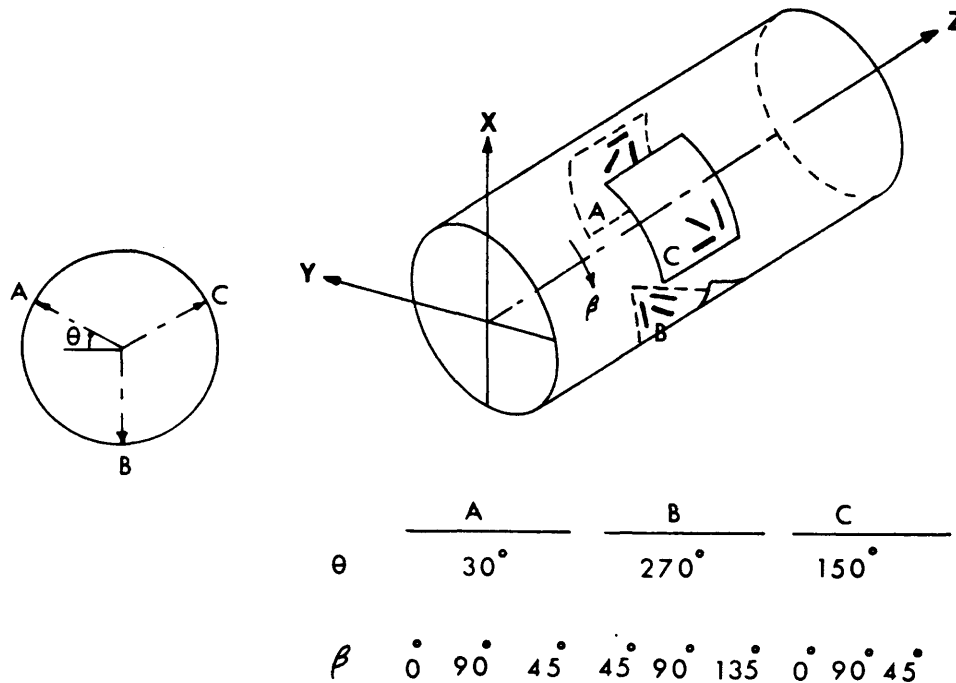


Figure 2.17 Orientation of the strain gages in CSIRO cell.

General Procedures of the Test

The following are the testing procedures used in measuring the in situ stress with the CSIRO cell:

- a. A pilot hole about 3 ft. long and 1.5 in. in diameter (EX) is drilled in the selected site.
- b. The Ex cores are examined before selecting the precise position for grouting the cell.
- c. The hole is cleaned with chlorinated degreaser.
- d. The pre-weighed resin components are homogeneously blended.
- e. The entire shell of the cell is roughened, filled with the resin, and then carefully installed in the hole with the recommended orientation.
- f. Twenty-four hrs. after the installation of the cell, the overcoring operation is performed using a 6" bit assembled in 2 ft. tin-walled core barrel. The bit advance is at a rate of about 1 in./min. After the core barrel is filled, the overcoring process is terminated.
- g. During the bit advance, strain readings are taken at one inch intervals, using a strain indicator and switch box with at least nine channels. (A sample of the strain readings vs. bit advance is shown in Figure 2.18.
- h. The 6" core is retrieved from the barrel or from the hole with the cell glued in place for testing in a bi-axial compression device to check the behavior of the

OVERCORING TEST (P-2) HOLE 3 (AT 14.3 FT.)

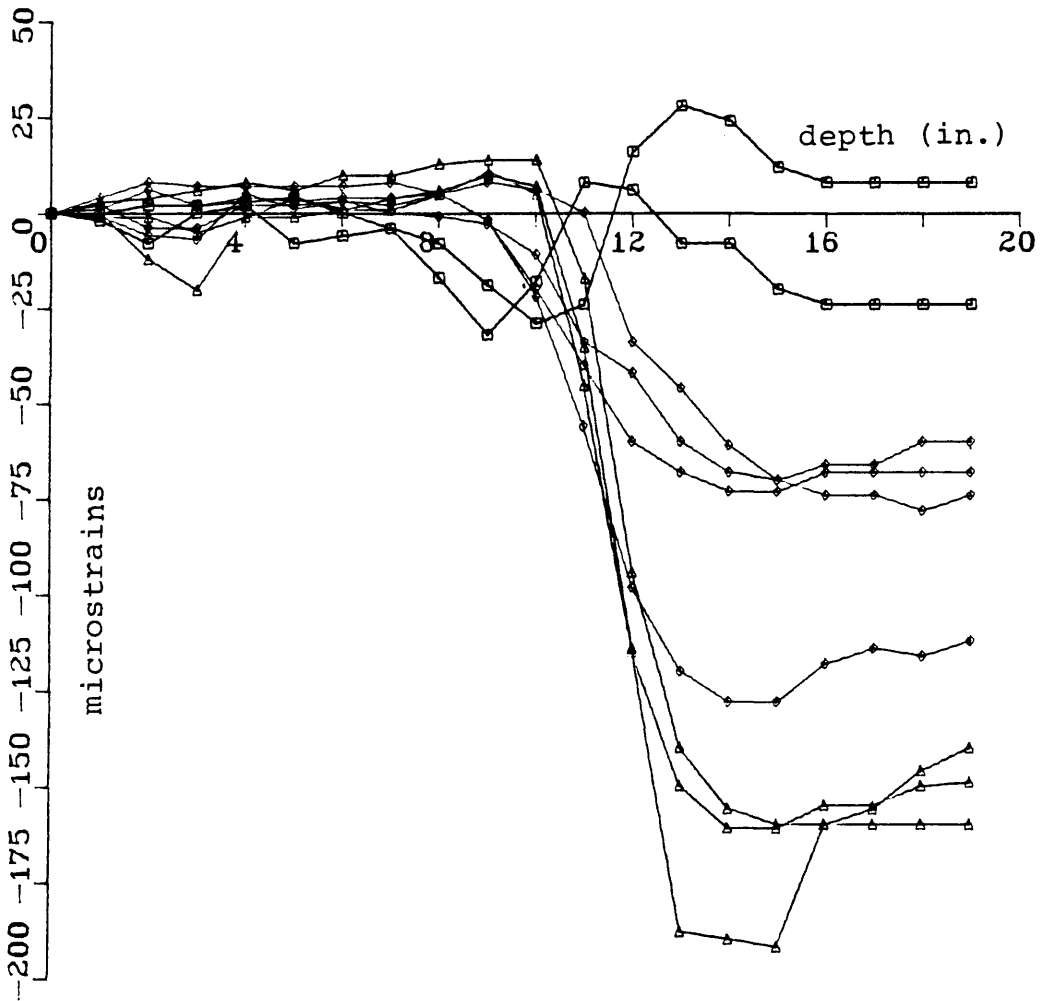


Figure 2.18 Strain readings overcoring test P-2.

strain gages and determine the elastic constants of the rock. (typical biaxial test result is shown in Figure 2.19.)

- i. The 6" core was then cut longitudinally to check the bond between the cell and the rock (Figure 2.20). The detailed testing and installation procedures are provided by the manufacturer's manual.

OVERCORE TEST (P-2)

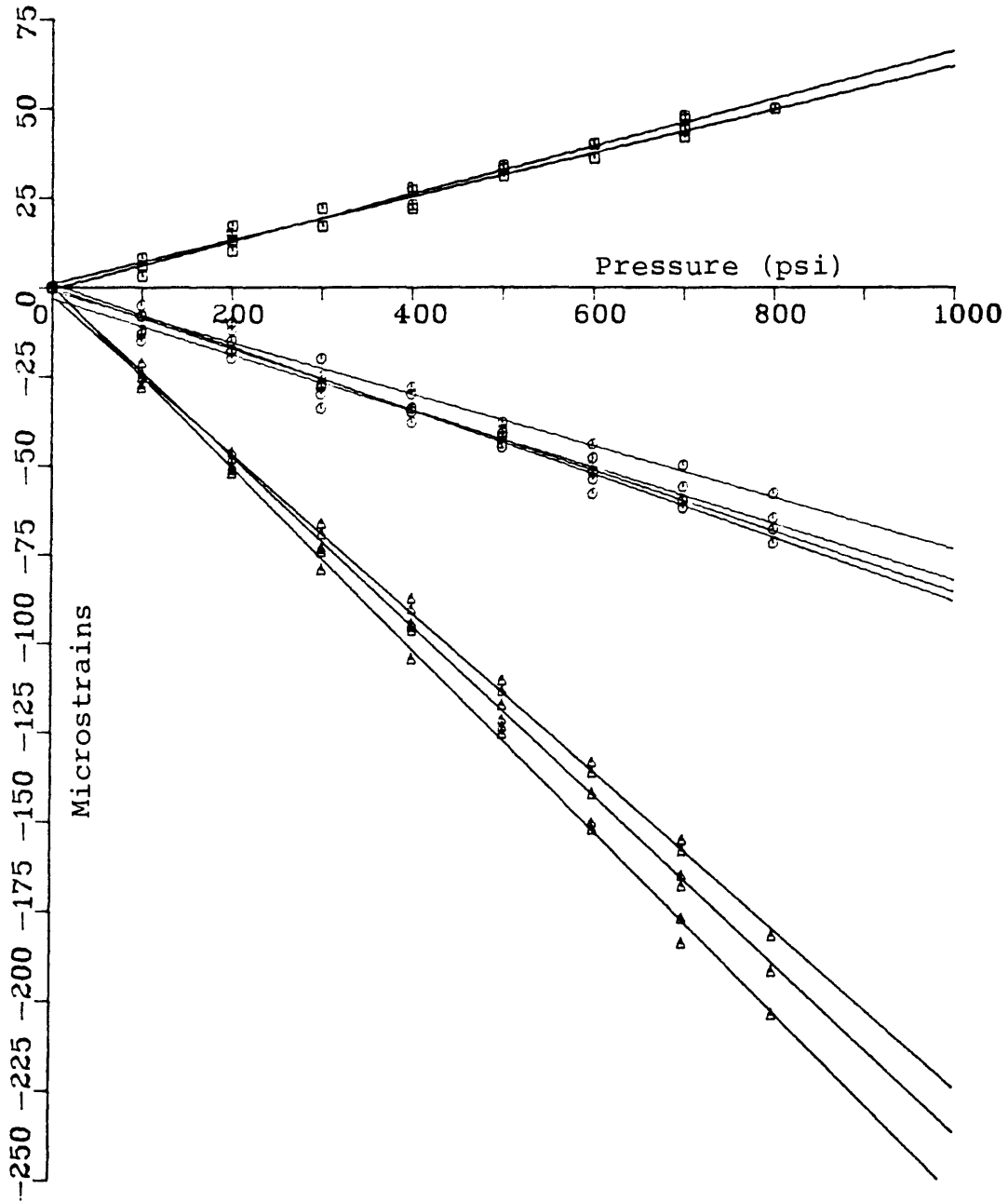


Figure 2.19 Biaxial testing overcoring test P-2.

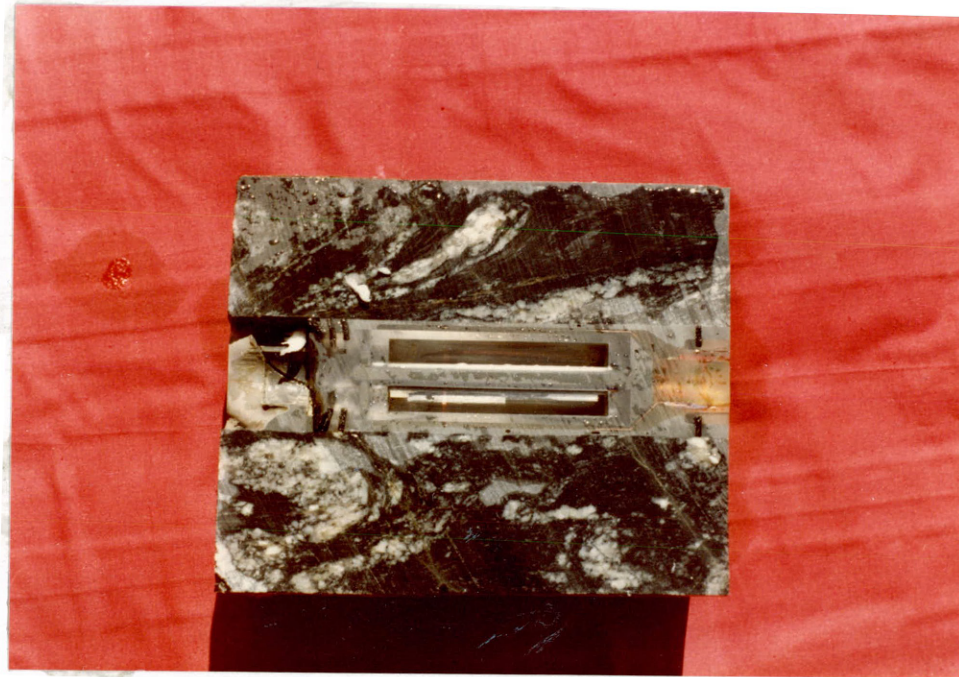


Figure 2.20 Longitudinal Section Through CSIRO Cell.

Theory Involved and Calculations of Stresses.

Assuming that the rock is linearly elastic and isotropic the relationship between the stresses in the rock away from the influence of the borehole and the strain at a point along the borehole wall is:

$$\epsilon E = F_1 \sigma_x + F_2 \sigma_y + F_3 \sigma_z + F_4 \tau_{xy} + F_5 \tau_{yz} + F_6 \tau_{xz}$$

ϵ = the measured borehole wall strain

E = the elastic modulus of the host rock

$\sigma_x, \sigma_y, \sigma_z$ = the normal stress components

$\tau_{xy}, \tau_{yz}, \tau_{xz}$ = the shear stress components

$F_1, F_2, F_3, F_4, F_5, F_6$ = functions of the strain gauges' orientation, Poisson's ratio and correction coefficients for the cell geometry.

As nine separate borehole strains are measured, a system of nine simultaneous multivariate linear equations can be written. In matrix form these are:

$$\begin{array}{c} \left| \begin{array}{c} U_1 \\ U_2 \\ - \\ - \\ - \\ U_9 \end{array} \right| = \left| \begin{array}{cccccc} F_{11} & F_{21} & F_{31} & F_{41} & F_{51} & F_{61} \\ F_{12} & F_{22} & F_{32} & F_{42} & F_{52} & F_{62} \\ - & - & - & - & - & - \\ - & - & - & - & - & - \\ - & - & - & - & - & - \\ F_{19} & F_{29} & F_{39} & F_{49} & F_{59} & F_{69} \end{array} \right| \left| \begin{array}{c} \sigma_x \\ \sigma_y \\ \sigma_z \\ \tau_{xy} \\ \tau_{yz} \\ \tau_{xz} \end{array} \right| \end{array}$$

the elements of the matrices U and F are known and thus statistical estimates of the elements matrix containing the six stress tensors (s) can be found by multiple linear regression.

$$S = (F^t F)^{-1} F^t U$$

where

$$F^t = \text{the transpose of } F$$

$$(F^t F)^{-1} = \text{the inverse of } (F^t F)$$

Principal stresses determination:

The principal stresses can be found by solving the function:

$$F(\sigma) = \begin{vmatrix} \sigma_x - \sigma & t_{yx} & t_{zx} \\ t_{yx} & \sigma_y - \sigma & t_{zy} \\ t_{zy} & t_{yz} & \sigma_z - \sigma \end{vmatrix} = 0$$

for σ , the function $f(\sigma)$ has three real roots and these roots are the principal σ_1 , σ_2 , and σ_3 . Expansion of equation (1) yields

$$\sigma^3 - I_1 \sigma^2 + I_2 \sigma - I_3 = 0$$

where

$$I_1 = \sigma_x + \sigma_y + \sigma_z$$

$$I_2 = \sigma_y \sigma_z + \sigma_z \sigma_x + \sigma_x \sigma_y - t_{yz}^2 - t_{zy}^2 - t_{xy}^2$$

$$I_3 = \begin{vmatrix} \sigma_x & t_{yz} & t_{zx} \\ t_{xy} & \sigma_y & t_{zy} \\ t_{xz} & t_{yz} & \sigma_z \end{vmatrix}$$

Solution of equation (2) is easily performed using the Newton-Raphson iteration method. A data reduction program code for analysis of stresses is given in Appendix B.

Results.

The data reduction program produces the three components of the stresses tensor, plus normal and shear stresses resolved into the reference coordinate axes:

X = vertical

Y = horizontal, normal to the hole axis

Z = horizontal, along the hole axis

The relevant statistical information is also listed. Because the strain readings have shown some fluctuation after the six inch bit had passed the centerline of the HI cell, the program was run for different sets of strain readings taken from the same test. The standard deviations have provided a good estimate of reliability of the results for each set of data. In particular, those results in which the standard deviation were initially low, and the stresses progressed to similar values with lower standard deviations, were considered the most reliable.

Table 2.10 shows the stress field components at each position based upon the CSIRO test results in the three holes.

Table 2.10 Results of In Situ Stress Measurements Using CSIRO Cell.

Hole 1		Stresses in Psi									
Test	Depth (ft.)	σ_1	σ_2	σ_3	σ_x	σ_y	σ_z	τ_{xy}	τ_{zx}	τ_{zy}	
H1	12	500 N62W 25.6SE	413 S15E 54.8NW	276 N39E 22SW	400	435	365	14	124	-100	
Hole 2											
T1	1	1145 N47.6W 44.4SE	583 S20E 46NW	-101 N55E 15SW	768	826	18	-217	1275	232	
T2	4.5	335 N11.4E 42SW	251 S89W 16NE	-96 S17E 43NW	154	81	253	-211	-17	0	
T3	7.5	775 N65W 19.2SE	551 N40E 36SW	522 S3W 47.8NE	551	652	638	64	40	104	
T4	15	486 N66W 21SE	432 N42E 39SW	300 S2.5W 43.6NE	378	404	435	38	-20	74	
T5	20	697 S62W 43.6NE	432 N63E 46SW	320 N26W 1.0SE	558	321	565	0	0	-130	

Table 2.10 (continued)

Hole 2		Stresses in Psi									
Test	Depth (ft.)	σ_1	σ_2	σ_3	σ_x	σ_y	σ_z	τ_{xy}	τ_{zx}	τ_{zy}	
T6	26	561 N73W 21.1SE	450 S16E 54.7NW	314 N28E 26.8SW	358	442	420	62	34	-5	
Hole 3											
P-1	6.5	536 S14W 62NE	338 N42E 25.2SW	217 N54W 11.5SE	470	348	272	-85	91	17	
P-2	14.3	489 N41W 19.4SE	424 S33E 70.7NW	267 S50W 2.2NE	375	405	257	27	7.0	52	
P-3	19.5	586 S81W 18.3NE	193 S24E 37NW	93 N14E 47.3SW	178	182	516	13	-142	.103	
P-4	25	422 N34W 38.8SE	385 S31W 27.7NE	247 S83E 38.7NW	372	404	278	30	50	-28	
P-5	29.5	507 S79W 74NE	388 S67E 13.4NW	266 N21E 9.05W	495	328	339	-7	44	61	

The principal stresses deeper than 12 ft. from the three tested holes are plotted (trend and plunge) in Lambert equal area net to investigate the stress clusters (Figure 2.21. Comparative graphical and averaging statistics have shown the preferred principal stresses are as follows:

$$\sigma_1 = 499.16 \text{ psi} \quad \text{N58W, plunge } 26.0^\circ$$

$$\sigma_2 = 382.5 \text{ psi} \quad \text{S4E, plunge } 52.0^\circ$$

$$\sigma_3 = 322.6 \text{ psi} \quad \text{N45E, plunge } 27.0^\circ$$

(+compressive)

Transformation of the principal stresses into the six components of the stress tensor for any other orientation (Obert, 1967), (i.e. axes of the room) has given the following:

$$\sigma_x \text{ (vertical)} = 391.2 \text{ psi} \pm 33.5$$

$$\sigma_y \text{ (horizontal)} = 465.5 \text{ psi} \pm 33.5 \text{ (parallel to room)}$$

$$\sigma_z \text{ (horizontal)} = 358.5 \text{ psi} \pm 33.5 \text{ (\perp to the room axis)}$$

Shear Stresses

$$\tau_{xy} = 34.4 \text{ psi}$$

$$\tau_{yz} = -49.9 \text{ psi}$$

$$\tau_{zx} = 45.5 \text{ psi}$$

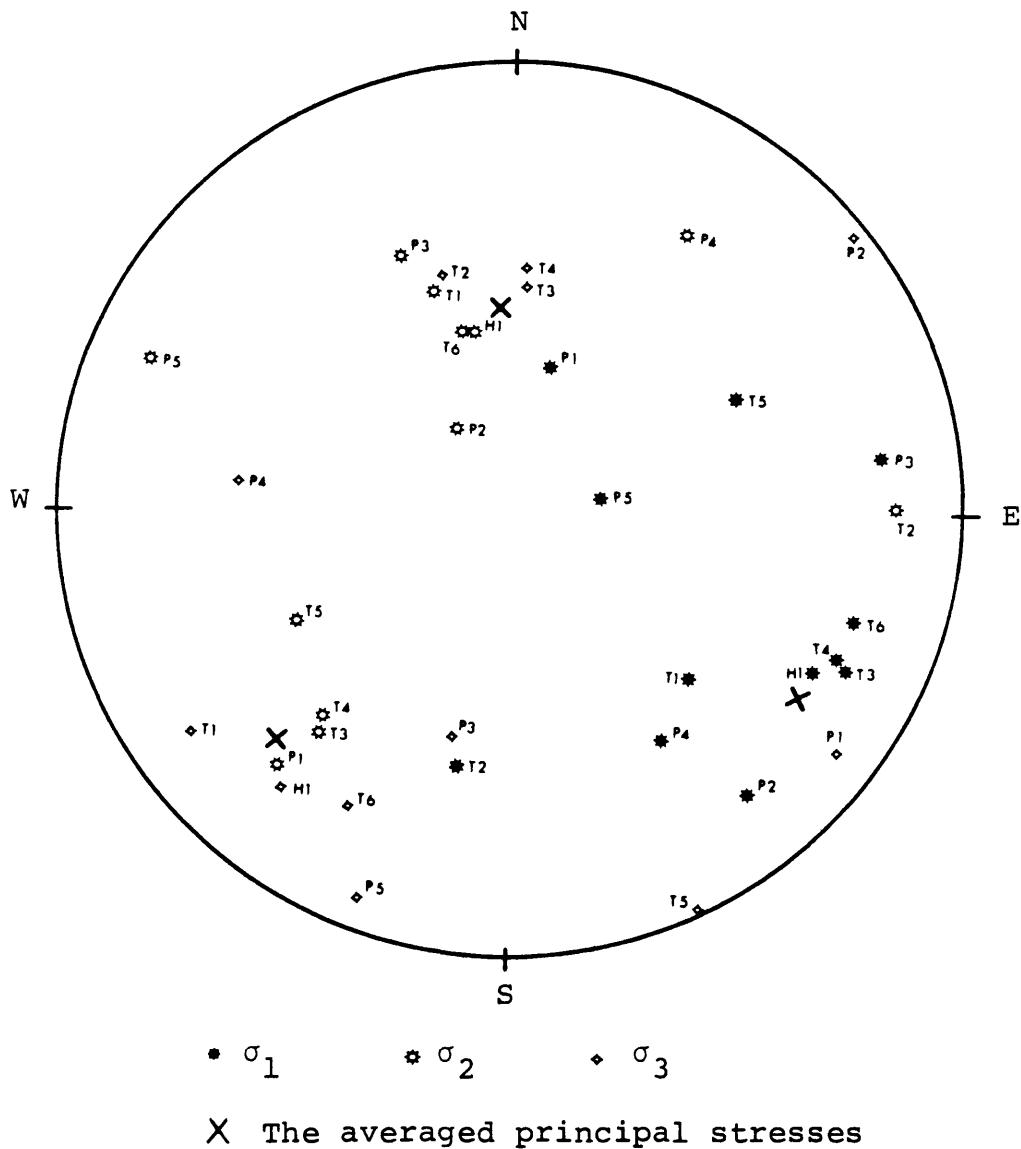


Figure 2.21 The principal stresses plotted in lower hemisphere equal area diagram.

Rock Properties for Stress Calculation.

The rock properties needed for stress calculation were the elastic modulus and the Poisson's ratio. Because of the calculated stresses being directly proportional to the modulus, the latter is a determining factor in calculating the former. Hence, choosing the right elastic constant for stress calculation was a sensitive issue. The following techniques were used to find the rock properties:

- a) Biaxial compressive testing on the overcores contained CSIRO cell.
- b) CSM cell testing in the pilot EX-borehole prior to the cell installation.
- c) Uniaxial compressive testing on samples obtained from the overcores.
- d) Biaxial compressive testing using USBM gage on overcores collected from locations neighboring CSIRO overcoring tests in the specific hole.

In calculating the elastic constants for CSIRO cell data produced by biaxial testing, the following formula was used:

$$E = \frac{\text{applied pressure}}{\text{circumferential strain}} \times 2.422$$

$$\nu = \frac{\text{axial strain}}{\text{circumferential strain}}$$

An example of application of the above formula is given below, using the test data of test P-2, shown in Figure 2.19.

The slopes; pressure/strain, were found for each of the three circumferential strain gage.

For strain gage 2 = 3.93×10^6 psi/microstrain

strain gage 6 = 4.5×10^6 psi/microstrain

strain gage 8 = 4.22×10^6 psi/microstrain

and thus, the elastic constants corresponding to these stress-strain relationships were calculated.

$$E_2 = (3.93 \times 10^6) \times 2.422 = 9.52 \times 10^6 \text{ psi}$$

$$E_6 = (4.5 \times 10^6) \times 2.422 = 10.9 \times 10^6 \text{ psi}$$

$$E_8 = (4.22 \times 10^6) \times 2.422 = 10.22 \times 10^6 \text{ psi}$$

$$\text{The average modulus} = 10.2 \times 10^6 \text{ psi}$$

Poisson's ratio calculated for test P-2:

$$\nu_{12} = \frac{0.06033}{0.2546} = \frac{(\text{axial strain/pressure})\text{slope}}{(\text{circumferential/pressure})\text{slope}} = 0.237$$

$$\nu_{78} = \frac{0.06679}{0.23692} = 0.28$$

$$\text{The average Poisson's ratio} = 0.26$$

where:

ν_{12} = Poisson's ratio calculated using the data of strain gages 1 and 2. Both gages at rosette (A), see Figure 2.17.

ν_{78} = Poisson's ratio calculated using the data of strain gages 7 and 8. Both gages at rosetts (c), see Figure 2.17.

Drift in the strain readings was noticed at the end of some biaxial tests using CSIRO cell. In other words, the strain was not totally recovered to its original reading by the removal of the biaxial pressure. This drift was subtracted linearly from the strain readings. Biaxial testing results are given in Appendix A, and summarized in Table 2.11.

Table 2.11 Biaxial Compressive Testing Results

Test	Depth (ft.)	$\times 10^6$ E psi	ν
H 1	12	8.4	0.31
T 1	1	11.6	0.6
T 2	4.5	5.15	.25
T 3	7.5	8.33	.43
T 4	15	9.7	.42
T 5	20	9.14	0.25
T 6	26	-	-*
P-1	6.5	-	-*
P-2	14.3	10.2	0.26
P-3	19.5	10.3	0.4
P-4	25	-	-*
P-5	30	13.8	0.22

*The overcore was damaged during retrieving

CSM cell was used to determine the rock mass modulus in the pilot (EX) borehole prior to the cell installation. The tests were done in the overcoring hole no. 3 only. The elastic modulus was measured at different distances from the wall. Table 2.12 gives the results of these tests.

Table 2.12 CSM Cell Results in the Overcoring Hole.

Depth (ft.)	Ex10 ⁶ psi	Overcoring Test
1	5.13	
2	4.8	
3	3.6	
6.5	7.2	P-1
8	6.75	
9	4.46	
10	2.25	
11	6.9	
12	5.5	
14.5	6.0	P-2
Avg.	5.2	

Difficulties were encountered in placing the cell beyond the depth of 14.5 ft.

The results associated with laboratory testing on samples obtained from the overcores are given in Table 2.13.

The samples were collected from the overcores of the three tested holes; see Figure 2.15.

Table 2.13 Laboratory Testing on the Overcores Samples
(EX10⁶ psi)

Depth Range (ft.)	Hole 1		Hole 2		Hole 3	
	E	v	E	v	E	v
0- 1	-	-	-	-	-	-
1- 2	6.2	0.24	8.4	.25	-	-
2- 3	6.5	0.29	5.4	0.18	-	-
3- 4	-	-	-	-	-	-
4- 5	7.2	0.19	6.0	0.24	7.7	0.23
6- 7	8.1	0.26	-	-	9.2	0.23
12-13	7.2	0.24	9.3	0.17	-	-
13-14	-	-	-	-	-	-
14-15	-	-	-	-	8.4	0.21
16-17	-	-	8.9	-	-	-
19-20	-	-	-	-	10.3	0.24
21-22	-	-	8.8	0.31	-	-
24-25	-	-	7.75	0.21	11.4	0.22
25-26	-	-	10.3	0.21	-	-

The USBM borehole gage was used also to determine the elastic constant for stress calculation. Trials were made to install USBM gage at the same position where the CSIRO cell was cemented. These trials were unsuccessful, due to damaging the EX-hole in the overcore during the cell coring. However, the gage was used to test other adjacent overcores from the same hole. The results are given in Table 2.14.

Table 2.14 Biaxial Test Results, USBM Gage
($\times 10^6$ psi)

Depth (ft.)	Hole 1	Hole 2	Hole 3
2.5	6.06	-	7.44
3	-	8.2	-
4.5	7.7	-	8.26
12	9.4	10.2	5.22
15	7.11	-	-
17	8.9	9.28	8.07
21	-	9.14	9.05
23	-	-	9.05
27	-	-	10.39
28	-	-	9.47

Investigation of all above modulus data have shown that, there was a noticeable difference between the CSM

cell results and the other techniques. The results from CSM cell have yielded a lower elastic modulus of an average about 2/3 of those obtained by the biaxial testing. However, judgement was made based upon the inspection of the over-cores, strain readings, and the comparison between the available data. Table 2.15 gives the elastic properties used in the stress calculation.

Table 2.15 Rock Properties for Stress Calculation.

Test	Elastic Constant $\times 10^6$ psi	Poisson's Ratio
H 1	6.6	0.31
T 1	8.4	0.25
T 2	5.15	0.24
T 3	6.7	0.22
T 4	6.4	0.25
T 5	8.4	0.16
T 6	6.4	0.2
P-1	7.2	0.23
P-2	6.0	0.26
P-3	6.4	0.40
P-4	7.2	.22
P-5	5.2	0.22

2.3.4 In Situ Stress Results Based on USBM Deformation Gage.

The locations of these tests were given previously, and they have been conducted intermittently with CSIRO cell in hole 3. No useable data was obtained from the overcoring process in hole 1 and the first five measurements in hole 3 (up to 5.3 ft.) due to highly fractured material. The reliefs between 8.25 ft. and 13.3 ft. seemed sporadic partly due to fractures and grain configurations; hence, they are discarded also. The data obtained from 15.92 ft. to 23.5 ft. were the basis for calculations of the stress components from USBM gage (Tadolini, et al., 1981).

Deformation of the borehole and the rock properties used in this analysis are given in Appendix B.

The calculated stresses from the deformation measured by the USBM gage with respect to the x, y coordinate system; i.e. with y in the horizontal and x in the vertical position as the hole is being faced are:

$$\sigma_x = 320 \text{ psi} \pm 61 \text{ psi}$$

$$\sigma_y = 496 \text{ psi} \pm 61 \text{ psi}$$

$$\tau_{xy} = 179 \text{ psi} \pm 36 \text{ psi}$$

The secondary principal stresses are:

$$P = 607 \text{ psi}$$

$$Q = 208 \text{ psi}$$

$$\theta = 32^\circ \pm 5^\circ$$

A stress profile was compiled from individual stress reliefs as shown in Figure 2.22.

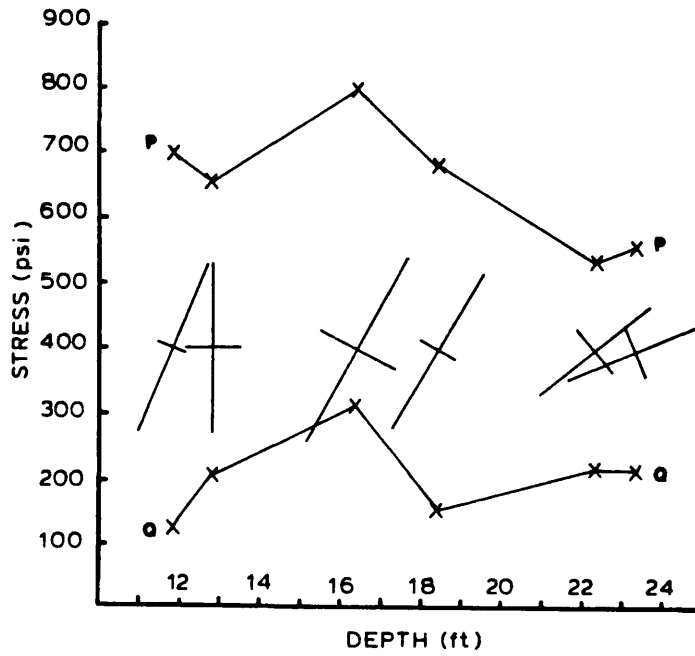


Figure 2.22 The in situ stress profile (USBM gage).

2.3.5 Near Stress Field.

This stress field is defined as those stresses surrounding the room and having been created by redistribution of the original stress field (stresses prior to the excavation) due to the room excavation. Stresses measured at depths less than 12 ft. are considered to belong to this near stress field. Measurements of this field are given in Table 2.16.

Table 2.16. Near Stress Field Measurements.
(stress component in psi)

Depth in the wall (ft.)	CSIRO Measurements			Depth in the wall (ft.)	USBM Measurements	
	σ_x	σ_y	σ_z		σ_x	σ_y
1	768	826	18	0.8	1851	2156
4.5	154	81	253	1.8	1237	801
6.5	470	348	272	2.8	379	1346
7.5	551	652	638	3.8	963	2082
12	400	435	365	4.8	1467	270
σ_x = vertical σ_y = horizontal and parallel to the room axis				8.8	515	921
				9.3	1082	2360
				10.8	1395	332
				11.8	475	1112

σ_z = horizontal and perpendicular to the room axis.

The measurements seemed to be variable and hard to compare, however. They are higher than those used for the

in situ stress field determination, and more than 60% of these measurements agreed on the horizontal stress $\sigma_y >$ the vertical stress σ_x , and $\sigma_y/\sigma_x \approx 1.1$ to 2.1.

2.3.6 Influence of Topography

The topography influence was considered perpendicular to the tested borehole. A vertical section, 2,000 ft. wide crossing the borehole and the topography was analyzed using (Hooker's approach, 1972). Details of this configuration and the analysis are given in Appendix B.

The total influence of topography was found as follows:

$$\sigma_{xg} = 40.6 \text{ psi}$$

$$\sigma_{yg} = 56.4 \text{ psi}$$

$$\tau_{xyg} = 39.9 \text{ psi}$$

(g subscript used for stress due topography)

Hence, the normal stresses in x, y coordinates will be:

$$\sigma_x \text{ (vertical)} = 275 \left(\frac{168}{144} \right) + (40.6) = 361.4 \text{ psi}$$

$$\sigma_y \text{ (horizontal)} = \left(\frac{0.22}{1-.22} \right) (361.4) \left(\frac{168}{144} \right) + (56.4) = 175.3 \text{ psi}$$

$$\tau_{xy} = 39.9 \text{ psi}$$

and the effect on the θ angle is calculated from the formula:

$$\theta = \frac{1}{2} \tan^{-1} \left(\frac{2 \tau_{xy}}{\sigma_x - \sigma_y} \right)$$

$$\theta = \frac{1}{2} \tan^{-1} \frac{(2 \times 39.9)}{(361.4 - 175.3)} = -11.6 \text{ degrees toward the mountain.}$$

2.3.7 Discussion and Conclusion.

Reviewing the state of stresses in different locations at the Experimental mine have shown the variability of the stresses values and directions from one place to another. This was expected when considering the rock type, the local and general structure, topography, and low magnitude stresses.

The variability of stress field has been reported for this rock mass before by Wentworth (1966). Since the comparison of final results of both measuring technique, USBM borehole gage and CSIRO cell have shown great agreement, considering the results and the errors:

USBM stress components:

$$\sigma_x = 320 \text{ psi} \pm 61$$

$$\sigma_y = 496 \text{ psi} \pm 61$$

$$\tau_{xy} = 179 \text{ psi} \pm 36$$

CSIRO stress components:

$$\sigma_x = 391.2 \text{ psi} \pm 33.5$$

$$\sigma_y = 465.5 \text{ psi} \pm 33.5$$

$$\tau_{xy} = 35.4 \text{ psi} \pm 7.3$$

Stresses calculated from topography:

$$\sigma_x = 361.4 \text{ psi}$$

$$\sigma_y = 175.3 \text{ psi}$$

$$\tau_{xy} = 39.9 \text{ psi}$$

The representative stress components selected for use in the analytical prediction models will be as follows:

$$\sigma_x \text{ (vertical)} = 355.55 \text{ psi}$$

$$\sigma_y \text{ (horizontal)} = 480.75 \text{ psi (parallel to the room axis)}$$

$$\sigma_z \text{ (horizontal)} = 358.50 \text{ psi (\perp to the room axis)}$$

$$\tau_{xy} = 36.2 \text{ psi}$$

$$K \approx 1.01 \text{ to } 1.35$$

To approximate the excess tectonic stress which can be found by subtracting the gravitational stresses from the measured stresses (Hooker, 1972), the tectonic stress component in the x-y coordinate, it is found that the y component is only one and has a significant value of 305.45 psi (y-direction is N23W).

Plotting the principal stresses with the structural data of the area in equal area net, Figure 3.11 displays no obvious geometric relation to the large structural features of the rock mass, and this could be attributed to: a) dispersion of data; b) complexity of the geologic environment; c) not enough data for either set to precisely define the relationship; d) the observed stress values are a combination of gravity effect, excess tectonics stresses and induced stresses due to previous mine excavations.

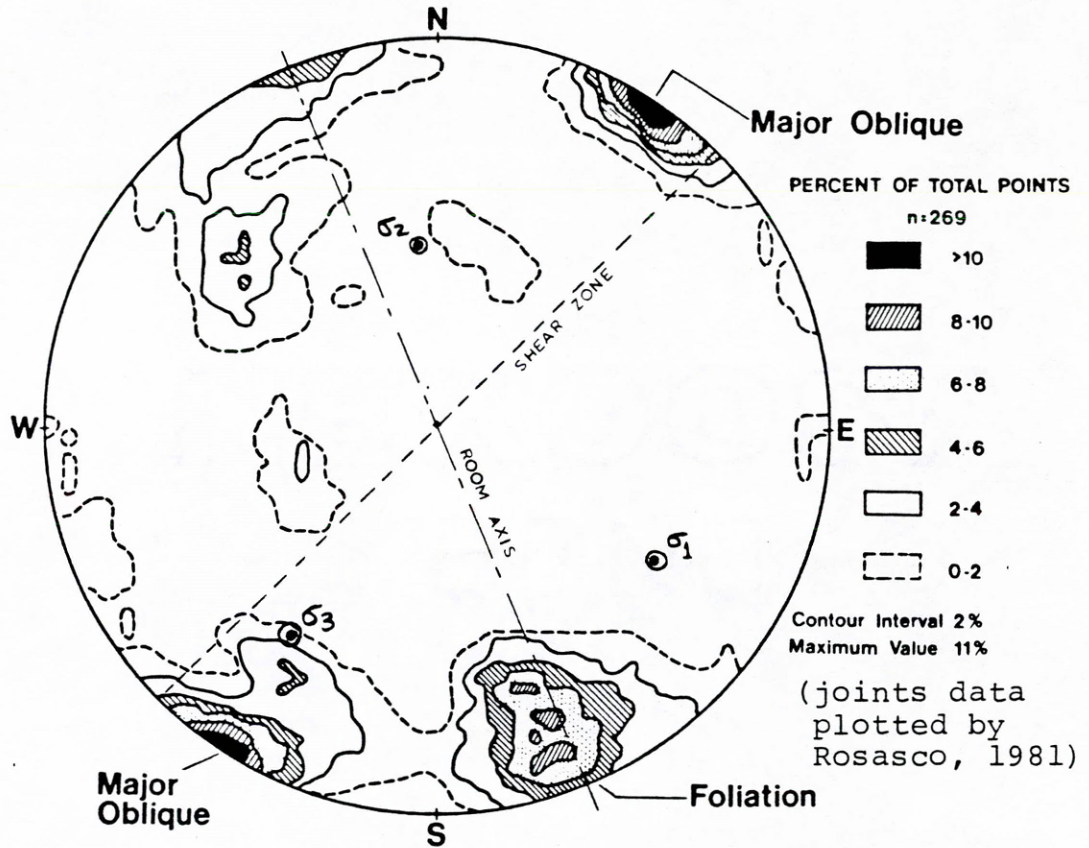


Figure 2.23 In situ stresses, and the joint sets in the site (lower hemisphere equal area net).

Investigation of the overcores to locate the exact position of the pistons of USBM borehole gage, and to compare the strain readings obtained from each piston have shown that when the pistons were located on a quartz intrusion, the stress levels were high, while the pistons located on the biotite gneiss showed a lower state of stress, Tadolini (1981).

2.4 Rock Mass Modulus

2.4.1 Introduction.

The rock mass modulus is the in situ substitute of the elastic modulus of the rock measured in the laboratory, i.e. it is a measure of deformability of in-place rock mass with all its defects and discontinuities. This modulus is a function of the intact rock modulus and the degree of fissuration (Goodman, 1979). In most literature the modulus is expressed as a percentage of the intact rock modulus.

Several field techniques were developed during the last few decades to determine the in situ modulus of deformation, the most widely used techniques are:

- Field loading technique
 - Plate-bearing loading
 - Flat jacking
 - Radial jacking
 - Cable method
- Borehole expansion technique
 - Cylindrical pressure cell
 - Goodman jack
 - CSM-cell

For this study a new CSM-cell was built to measure the change of the rock mass modulus around the experimental room. Six rings of seven NX-boreholes were drilled radially

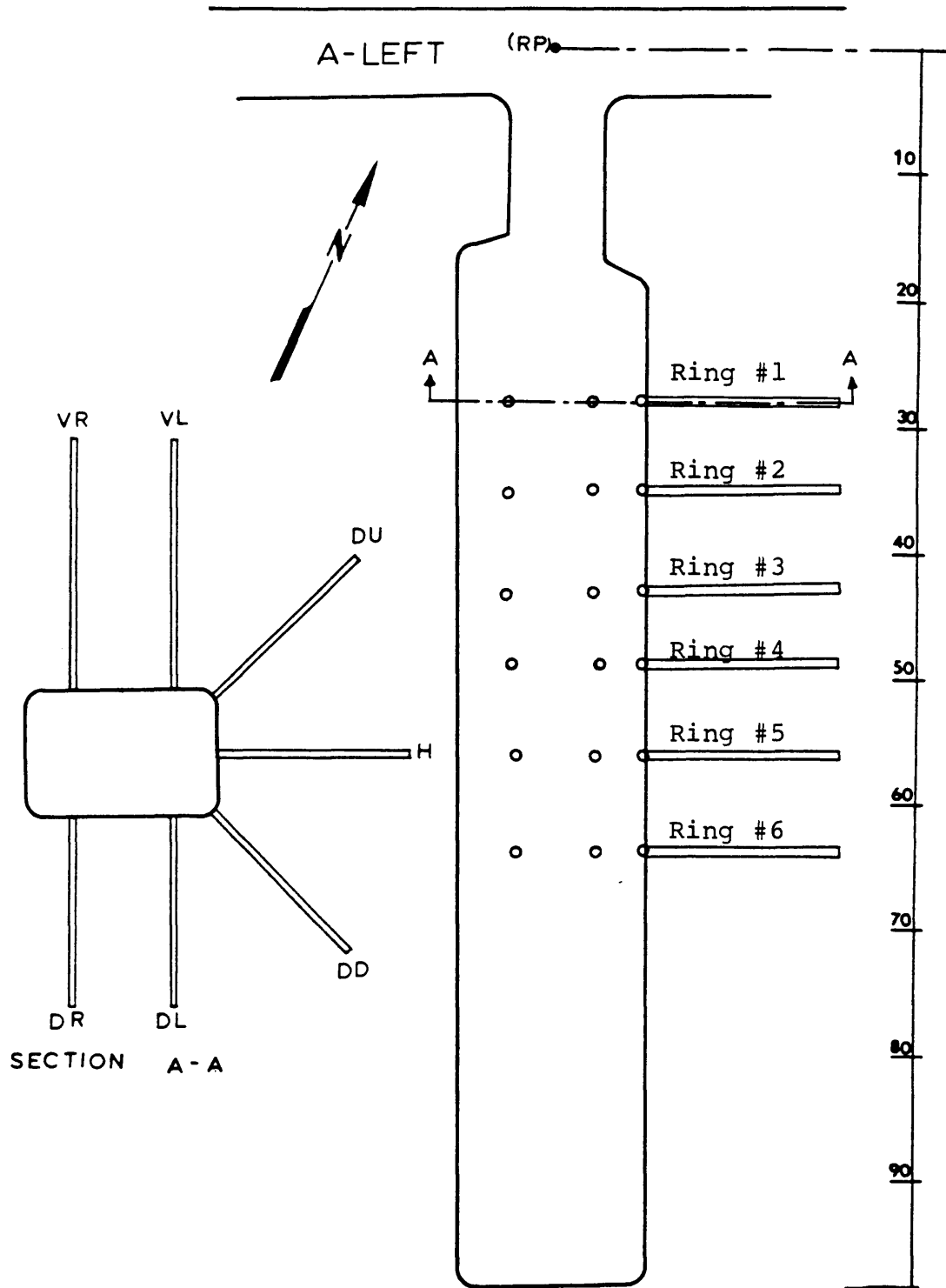


Figure 2.24 The radial boreholes location in the experimental room.

from the room for general testing purposes. For this study the holes were used for determination of the rock mass modulus. Figure 2.27 shows the location of these radial boreholes.

2.4.2 CSM-Cell.

CSM-Cell is a borehole device for determining the modulus of rigidity (G) of the rock; hence, the rock mass modulus by the relationship

$$E_r = 2 (1 + \nu) G$$

where

E_r = rock mass modulus

G = modulus of rigidity

ν = Poisson's ratio

CSM-Cell Design.

The cell has been designed by Hustrulid, 1979, to be used in NX-borehole (3 in. in diameter with the pressure being applied over a length of 6.5 inches).

The basic elements of the system are shown in Figure 2.28, and are described as follows.

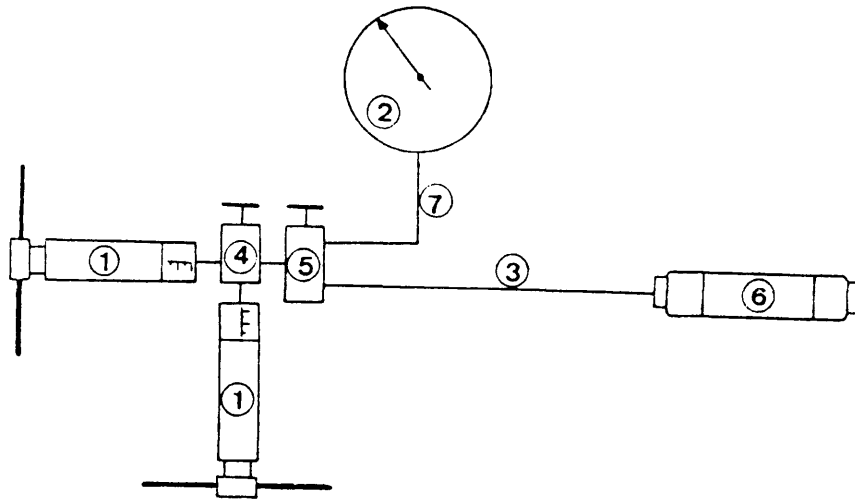


Figure 2.25 The Components of the CSM-Cell System.

- (1) Pressure generator, with vernier indicator, rated at a pressure capacity of 5,000 psi, and fluid capacity of 60 c.c (2 pressure generators have been used).
- (2) Bourdon gauge rated at 0 to 6,000 psi with a bleeder for purging flushing, and bleeding the Bourdon tube. The pressure readings can be read with an accuracy of ± 5 psi.
- (3) Forty (40) ft. of high pressure stainless steel tubing, 1/8" OD and 0.04" ID rated at 30,000 psi short pieces of 1/4" OD stainless steel tubing with the necessary fittings, are silver soldered over the ends of the 1/8" tubing in order to increase the strength and reliability of the connections.
- (4) Three-way high pressure valve rated at 30,000 psi.
- (5) Three-way high pressure valve rated at 30,000 psi.
- (6) CSM borehole cell-the cell is shown diagrammatically in Figure 2.26.

(7) Short stainless steel nipples 1/4" OD and 0.083" ID rated at 30,000 psi.

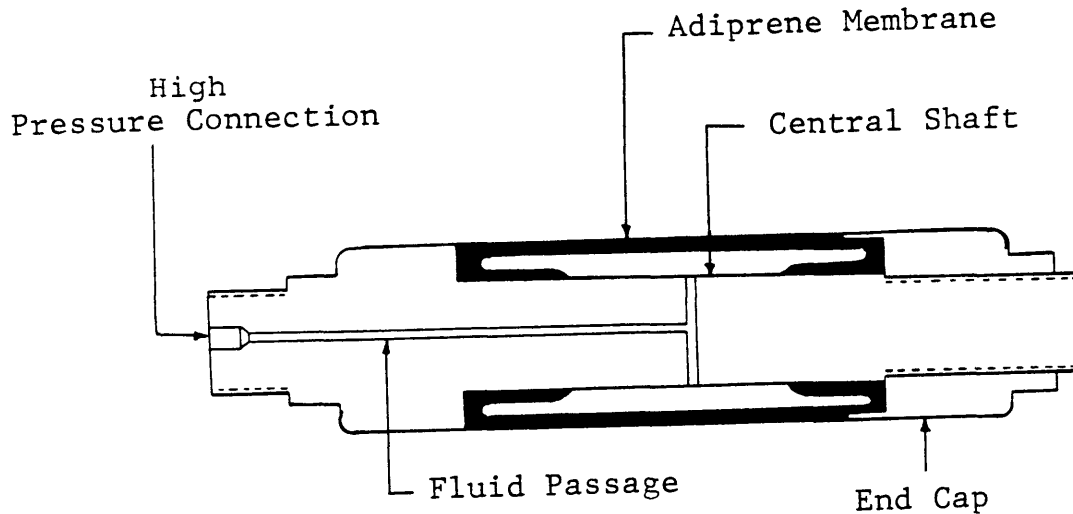


Figure 2.26 Diagrammatic Representation of the CSM-Cell.

The pressurizing devices are two screw type pressure generators, each pressure generator can expel 0.043 cubic inches per turn. A mixture consisting of one part of Conoco permanent antifreeze (ethylene-glycol base) and five parts of water by volume has been used as pressurizing fluid.

Calibration of the System.

The newly built CSM-cell system has been calibrated in the laboratory before its use in the site. The calibration has been performed in an aluminum block 12x12x12 inches, with a NX-borehole drilled in it. The elastic constants of the block were known, the modulus of rigidity, Young's modulus, and Poisson's ratio. By using another calibration cylinder of known elastic constants and CSM-cell, the elastic constants of the block were found. The results of this calibration have proven the reliability of the testing procedures and the system to be used in the site. The data and the calculation of the cell calibration is given in Appendix C.

2.4.3 Testing Sequence and Data Processing.

The below listed procedures were followed in testing the rock mass seeking the rock mass modulus values using CSM-cell.

- a. The system should be stored in the site for enough time to gain the ambient temperature.
- b. The cell is calibrated in a calibration cylinder of known elastic properties before testing the rock. This calibration gives the stiffness of the pressurizing system plus the calibration cylinder, i.e. readings of pressure vs. turns of the pressure generator shaft.

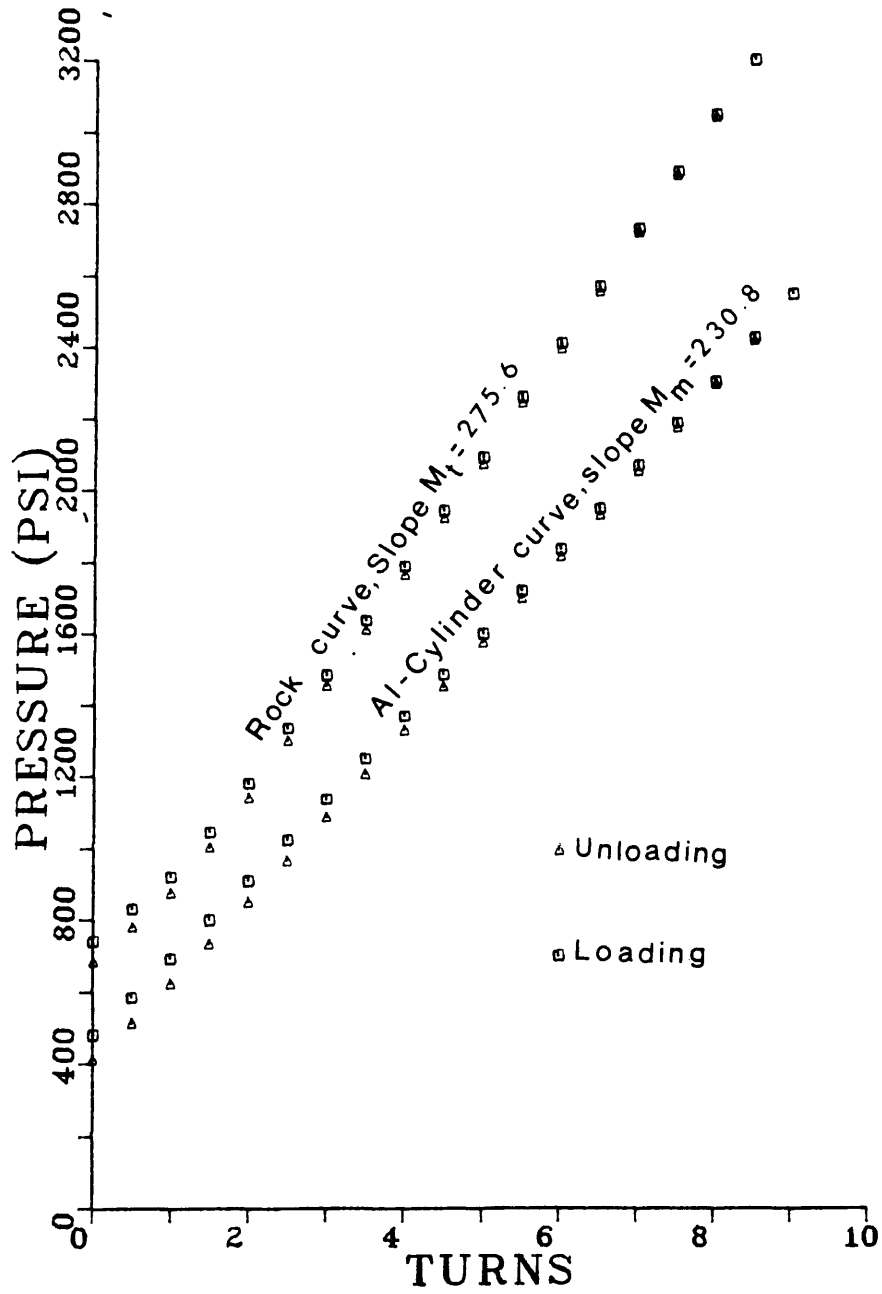


Figure 2.27 Pressure-volume curve for tests in calibration aluminum cylinder, and in the borehole.

The slope of this relationship is found by the least square method (M_m).

c. Testing the rock by inserting the cell in the borehole starting at the bottom of the borehole, recording the cell position, and performing the test in that position, the cell then moved outward to another position at one foot intervals. The relationship between the applied pressure versus turns for each position in the borehole is found (M_t).

d. After the borehole testing has been completed, the cell is then inspected for fluid leakage or any air bubbles introduced to the cell membrane. The cell is again recalibrated in the calibration cylinder.

e. The calibration slopes (before and after testing the rock) are compared; if the difference between the two slopes within the pressure gage accuracy ± 10 psi/turn, the averaged slope will be used in the calculation. Greater difference in the calibration slopes and within an acceptable limit will be linearly distributed over the number of the tests to find (M_m) which corresponds to each testing position.

Typical pressure-volume curves for both calibration and rock testing are shown in Figure 2.27.

From the testing experience and the cell calibration (Appendix C), it is found that:

- The stiffness of the pressurizing system is becoming greater with the excessive use of the cell, i.e. the relationship between the pressure and the volume for both calibration and rock testing are becoming greater by successive testing. So that the distribution of the difference between the calibration slopes linearly over the number of tests in the rock does not lead to erroneous results.
 - The pressure-volume (turns) relationship is linear for pressures over 500 psi. Hence, the slopes of pressure vs. volume for both calibration and rock testing was calculated for regions above 500 psi. This pressure under 500 psi was used to expand the system components, and to put the cell membrane in full contact with the rock.
 - A maximum pressure of 4,000 psi was enough to calculate the pressure-volume relationship, from which the final results become reliable.
- f. To find the rock mass modulus the following calculations were made:

The stiffness of the calibration cylinder (M_c) is found by the formula

$$M_c = \frac{\gamma G_c}{L r_{ic}^2 \left\{ \frac{1 + B - 2 v_c B}{1 - B} \right\}}$$

where:

γ = fluid/turn of pressure generator, in 3/turn.

L = effective length of the membrane, in.

r_{ic} = inner radius of the calibration cylinder, in.

r_{oc} = outer radius of the calibration cylinder, in.

$$B = (r_{ic}/r_{oc})^2$$

G_c = modulus of rigidity of the calibration cylinder, psi.

ν_c = Poisson's ratio of the calibration cylinder.

The stiffness of the pressuring system (M_s) can then be calculated using the equation:

$$M_s = \frac{M_c}{\frac{M_c}{M_m} - 1}$$

where:

M_c = calculated stiffness of the calibration cylinder (psi/turn)

M_m = measured stiffness of the pressurizing system plus the calibration cylinder (psi/turn)

M_s = calculated stiffness of the pressurizing system alone (psi/turn)

The pressure-volume relationship (M_r) for the rock alone can then be calculated as follows:

$$M_r = \frac{M_s}{\frac{M_s}{M_t} - 1}$$

where:

M_t = the slope of curve for the pressurizing system plus the rock.

then the modulus of rigidity of the rock could be determined by the relationship:

$$G_r = M_r \frac{\pi L r_{ir}^2}{\gamma}$$

where:

r_{ir} = radius of hole in rock

G_r = the modulus of rigidity of rock, and hence the rock mass modulus can be found by the relationship:

$$E_r = 2 (1 + \nu_r) G_r$$

ν_r = the Poisson's ratio of the rock

The detailed mathematical analysis of the CSM cell system is given in Appendix C.

2.4.4 Results.

The rock mass modulus values are tabulated and contoured for each of the six rings. Table 2.17 and Figure 2.28 are examples of the modulus results for ring no. 1. The remaining results for rings 2 through 6 are given in appendix C. Table 2.18 contains the consolidated results for all rings.

Table 2.17 Rock Mass Modulus
 (Ring No. 1)
 E_r values $\times 10^6$ psi

Depth (ft)	H	VR	VL	DR	DL	DU	DD
19	-	-	-	-	-	-	-
18	-	4.01	-	-	-	-	-
17	-	3.52	-	-	-	-	-
16	-	4.87	3.65	-	-	-	-
15	-	4.90	5.09	5.41	-	-	-
14	5.2	4.89	6.80	5.42	-	6.32	5.3
13	6.19	4.90	5.35	5.01	5.22	6.13	4.29
12	5.35	5.31	4.83	4.9	4.78	4.23	4.68
11	5.32	5.21	2.34	5.78	4.12	6.5	5.29
10	5.31	5.22	5.48	7.2	4.18	6.4	4.63
9	5.94	5.01	5.35	5.90	6.65	6.41	3.64
8	3.90	4.70	2.84	5.8	3.5	6.33	4.28
7	6.3	4.20	7.40	4.9	2.82	5.38	4.87
6	5.46	3.4	8.00	5.82	3.5	5.64	5.39
5	5.03	4.86	8.20	5.90	5.9	6.37	3.45
4	5.91	4.63	5.90	4.55	7.5	4.23	7.2
3	4.97	2.81	4.30	4.61	3.04	6.13	7.09
2	6.80	5.80	2.06	4.75	5.02	2.87	4.38
1	6.10	3.95	3.07	4.56	5.02	3.17	1.66

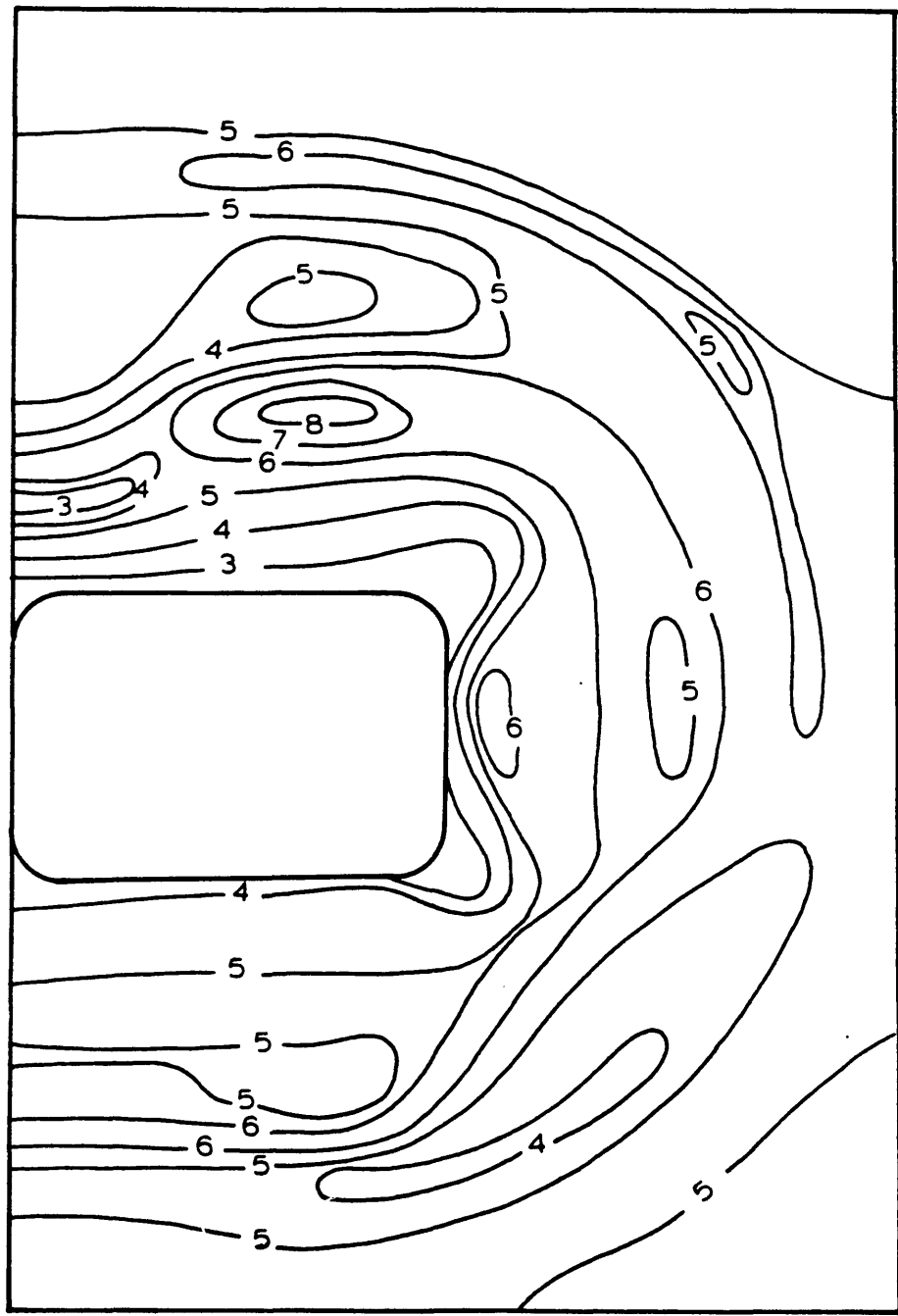


Figure 2.28 Rock mass modulus distribution in Ring #1.

Table 2.18 Averaged $E_r \times 10^6$ psi

Depth (ft)	Averaged E_r /ft/Ring						E_r average for each depth
	Ring #1	Ring #2	Ring #3	Ring #4	Ring #5	Ring #6	
19	-	3.34	3.01	-	-	4.19	3.51
18	4.01	2.88	2.63	5.95	3.00	4.25	3.79
17	3.52	3.14	2.25	5.39	3.00	3.94	3.54
16	4.26	3.42	2.27	5.24	2.50	3.80	3.58
15	5.13	3.66	2.83	4.89	3.06	3.85	3.90
14	5.65	4.05	4.44	4.56	4.04	4.27	4.50
13	5.29	4.93	4.54	5.07	4.16	4.18	4.70
12	4.86	5.98	4.08	4.91	3.65	4.68	4.69
11	4.94	5.34	3.99	5.10	4.66	4.07	4.58
10	5.49	4.80	3.76	5.22	4.18	4.08	4.59
9	5.47	5.05	3.34	5.64	4.42	3.83	4.63
8	4.55	5.00	3.09	5.08	4.56	3.91	4.37
7	5.12	5.38	3.82	4.55	4.12	3.98	4.50
6	5.32	4.95	4.14	4.68	4.36	4.01	4.58
5	5.67	5.04	4.34	4.58	3.30	4.50	4.57
4	5.70	5.66	4.17	6.99	3.54	4.16	5.04
3	4.71	4.63	4.87	5.42	4.15	4.14	4.65
2	4.52	4.58	4.34	4.28	3.95	3.96	4.27
1	3.93	4.46	3.07	5.34	3.05	3.83	3.95
E_r /Ring	4.89	4.54	3.63	5.16	3.73	4.09	4.34
St.Dev.	0.63	0.86	0.77	0.61	0.59	0.22	0.57

*If the values of E_r for deeper depths than 15 ft. are excluded, because only they represent the up vertical holes, then the averaged E_r for the whole test is $(4.54 \pm .23) \times 10^6$ psi.

2.4.5 Discussion and Conclusion.

(1) CSM-Cell is a simple, reliable device for determining the rock mass modulus of deformation (E_r) and detection of fractures in the borehole as well. However, a qualitative picture of the degree of fissuration can easily be abstracted from the E_r values.

(2) The rock mass modulus have shown that the pre-existing fractures are the major factors controlling their values (i.e. values are lower than the overall average in the deeper sections of the boreholes).

(3) As far as blast damage is concerned, averaging of E_r values have suggested the damage has taken place within the first two feet.

(4) Contouring the rock mass modulus values around the room has suggested the following:

- a. The room is surrounded by a lower modulus zone of 3×10^6 psi, and has an average thickness of one foot. This lower modulus zone was noticed to be thicker (max. 3.5 ft.) around the corners of the room in some rings, ring 1, ring 2, ring 3, and the bottom corner in ring 4. The possible explanation for this phenomena could be attributed to drilling and blasting problems during the excavation. For rings 1 and 2 the hole deviations in the corner holes was large. For ring 3,

the existing intersecting joint set was considered the measure determinant of the blast results. For ring 4, excessive hole deviation resulted in reshooting of the contour holes. (Holmberg, 1979).

b. A zone of higher modulus 6×10^6 psi has appeared in the horizontal holes in rings 1, 3, 4, 5, and 6. This zone appears at a distance ranging from one foot (ring 1) to 5 feet (ring 5). This higher modulus zone has fallen within the higher near stress field, and this might suggest that the higher stresses, the bigger the modulus and/or the fractures closure occur due to higher stresses.

(5) Statistical conclusion shows that ring no. 3, and ring no. 5, were located in more fractured sections than the others, and ring no. 4 has shown the best location (i.e. higher averaged E_r for the ring).

(6) The rock mass modulus at the CSM experimental mine has been determined by other investigators; their methods and results are summarized below:

a. Panek, 1960, had conducted several borehole dilation tests in the CSM experimental mine pursuing a relationship between the mean joint spacing and the modulus of rigidity. He fitted his data with the following expression:

$$G_a/\bar{G}_a = 1/3 \sqrt{\bar{s}/d}$$

where:

G_a = the modulus of rigidity

\bar{G}_a = the mean modulus of rigidity

\bar{s} = mean fracture spacing

d = diameter of the borehole

Using his graph and the weighted average joint spacing in the room 44cm, (Rosasco, 1981) this yields an average rock mass modulus of 5.3×10^6 psi. If the maximum and the minimum joint spacing at the site were used, this would give a range of the rock mass modulus between 2.6×10^6 psi and 7.4×10^6 psi.

b. Cox, 1971, has concluded his investigation in this matter with these values:

E_r (horizontal) = 4.7×10^6 psi

E_r (vertical) = 4.0×10^6 psi

(The data for his modulus calculation were collected from an experimental room @ 350 ft. north of this site).

He used the following relationship to calculate E_r :

$$E_r = E / (1 + \sum_{i=1}^n K_i)$$

where:

E = modulus of core specimen, psi

K_i = normal stiffness of the joints, lb/in

n = number of joint sets

The values measured by the CSM-cell suggested the following:

$$E_r \text{ (horizontal)} = (4.41 \pm 1.63) \times 10^6 \text{ psi}$$

$$E_r \text{ (vertical)} = (5.1 \pm 1.15) \times 10^6 \text{ psi}$$

(7) The relationship between the modulus of elasticity of the intact rock specimen (E), and E_r was investigated. The results of this investigation revealed the following:

(a) By using the average values for all measurements, the (E_r/E) ratio was found as follows:

$$E_r = 4.5 \times 10^6 \text{ psi (data of 640 values)}$$

$$E = 8.9 \times 10^6 \text{ psi (data of 97 samples, Appendix A)}$$

$$E_r/E = 0.5$$

(b) Sixty pairs of E and E_r values were plotted as shown in Figure 2.29. Both E and E_r values were corresponding to the same position in a specific borehole. The plot showed that, all the points were fallen under $E = E_r$ line, or in other words, in this particular case, E_r value was always less than its corresponded value of E . The ratio E_r/E was found for each pair, and their average was equal to .51, with standard deviation of 0.17.

(c) A histogram representation of (E_r/E) ratio was constructed using the above data. Figure 2.30 shows the frequency distributions of the (E_r/E) ratio. It can be seen that, the ratio data was normally distributed around the mean, and the maximum percentage 25% of the data ranged between 0.5 and .6.

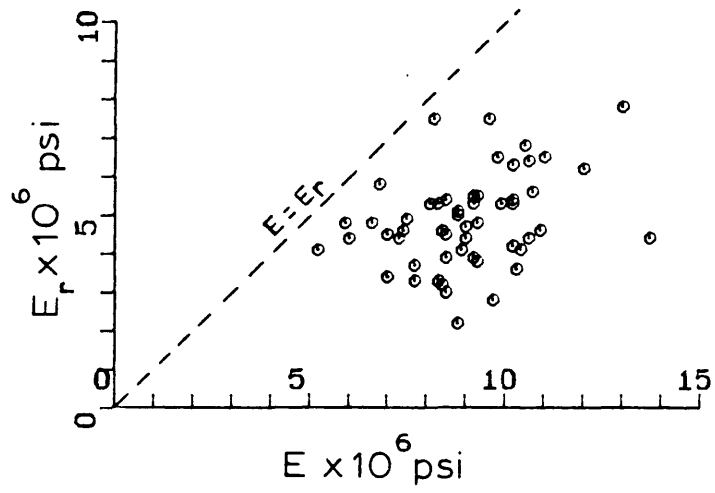


Figure 2.29 Rock mass modulus vs. intact rock modulus.

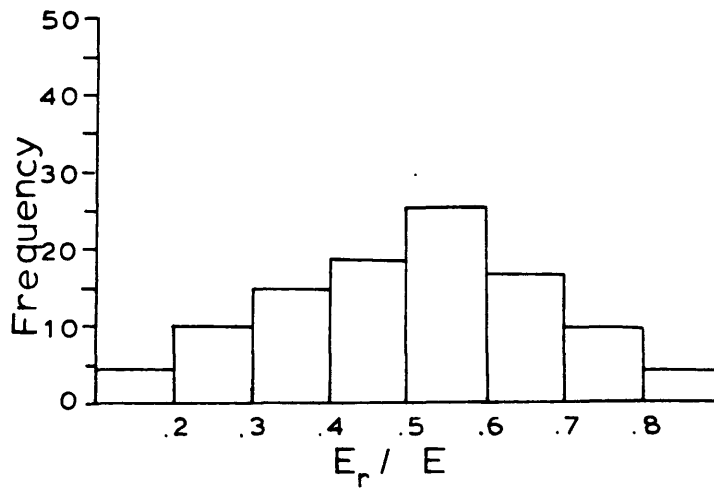


Figure 2.30 Histogram representing (E_r/E) ratio.

3. FINITE ELEMENT MODELING

3.1 Introduction.

The finite element method provides a convenient and versatile means of calculating theoretical stress and displacement fields for problems in rock mechanics. It is a method for representing the geological conditions, geometry, and in situ stress field in a mathematical model of an underground excavation. The method had been used successfully for predicting the rock behavior in many projects. For example: Tumut I and II, Lake Delio, Oroville, Churchill Falls, Morrow Point, Straight Creek, La Angostura, Wehr, and Helms (Willoughby, 1978).

In this method an appropriate geostructural slice of rock is isolated from the rock mass for structural analysis. This slice will be represented by a continuous framework of elements joined together at their vertices, called nodal points or nodes. The size and geometric configuration of these elements are chosen to suit an individual analysis. The concept of the method is that "the behavior of the parts defines the behavior of the whole".

The stress field in the rock mass will be replaced by external forces acting on the framework to induce internal forces in the elements and displacements at the nodal points. Both the internal forces and the nodal displacements are considered as unknowns in the basic theory of

element analysis. The mathematical justification of the theory of finite element method are established, and extensively discussed in the literature (Wilson, 1958, Clough, 1960, Turner, 1960, Martin, 1960, Zienkiewicz, 1967, Desai, 1967, Ural, 1972). It should be emphasized that stresses and deformation computed by finite element analysis are only as good as the assumptions associated with the theory and the material properties used in the analysis.

3.2 Model Development

3.2.1 Two Dimensional Representation of the Room Models.

The room was modelled by using finite the finite element method with two types of analysis. Plane strain model, in which the analysis was done on a vertical plane perpendicular to the room axis. Axisymmetry model, in which the analysis was performed on a longitudinal plane along the room axis. Figure 3.1 shows the configuration of the models relative to the room axis, along with the in situ stress components working on the model planes. Combination of the results produced by these models could approximate a three dimensional finite element model.

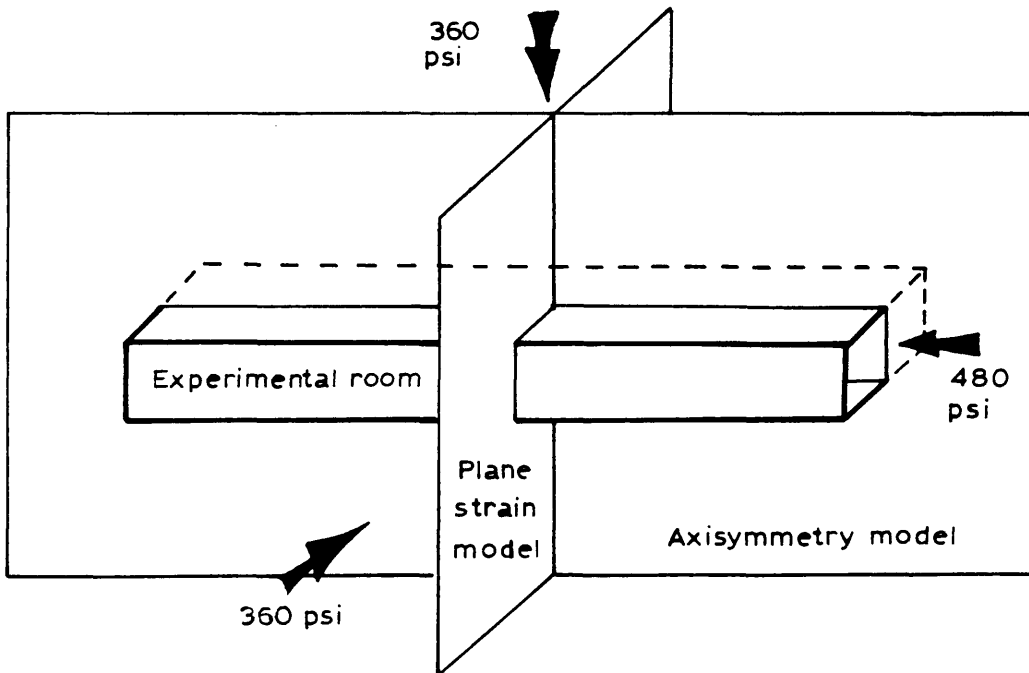


Figure 3.1 Configuration of the Experimental Room Models.

3.2.2 Modeling Procedure.

The following steps have been considered in finite element modelling: (The steps here are restricted to two dimensional finite element modelling.)

a) Define the area of interest to be isolated for structural analysis. (the size of the model to accommodate the excavation, and it should be large enough to minimize the boundaries influence in this area of interest).

b) Determine the geology of the model (rock types, contacts, and the shape).

c) Determine forces acting upon and within the model (stresses and rock density, and forces induced by rock bolts...etc.).

d) Determine the mechanical properties of the rocks (stress-strain relationship of the rock, Poisson's ratio, and the rock strength).

e) Select the model mesh (elements configuration) to delineate the rock contacts, excavation geometry, and other points of interest.

f) Analysis of the finite element model using structural analysis program to obtain deformation associated with the specified loading conditions without the excavation.

g) Loading and analyzing the same model with the excavation to obtain deformations and stresses associated with this condition.

h) Subtracting analysis of the deformations to obtain deformations comparable to the field case.

3.2.3 Modeling Analysis Assumptions.

The experimental room models were analyzed as a continuum media containing no discontinuities. The rock mass was simulated as homogeneous, linearly elastic, and isotropic material. These above mentioned assumptions were based upon the following geological and measurements observations: (geological information source: Rosasco, 1981).

The model material was considered to be one material; this was based upon the lithology of the room: there are three principal rock types encountered in the site; quartz-biotite gneiss, pegmatites, and amphibolites. The quartz-biotite gneiss is the dominant rock type; the pegmatites and amphibolite represent the minor rock types in the room. The different rock type distribution at the room is shown in figure 3.2 which shows that the quartz-biotite gneiss represent more than 90% of the rock type at the site.

The models were treated as continuum media because of the nature of the fractures in the room. The jointing in the room are moderately spaced, low persistence reflected by their length (less than 3 ft.), low interconnection (less than 50% of them terminate in each other), and tight (aperture less than .1mm).

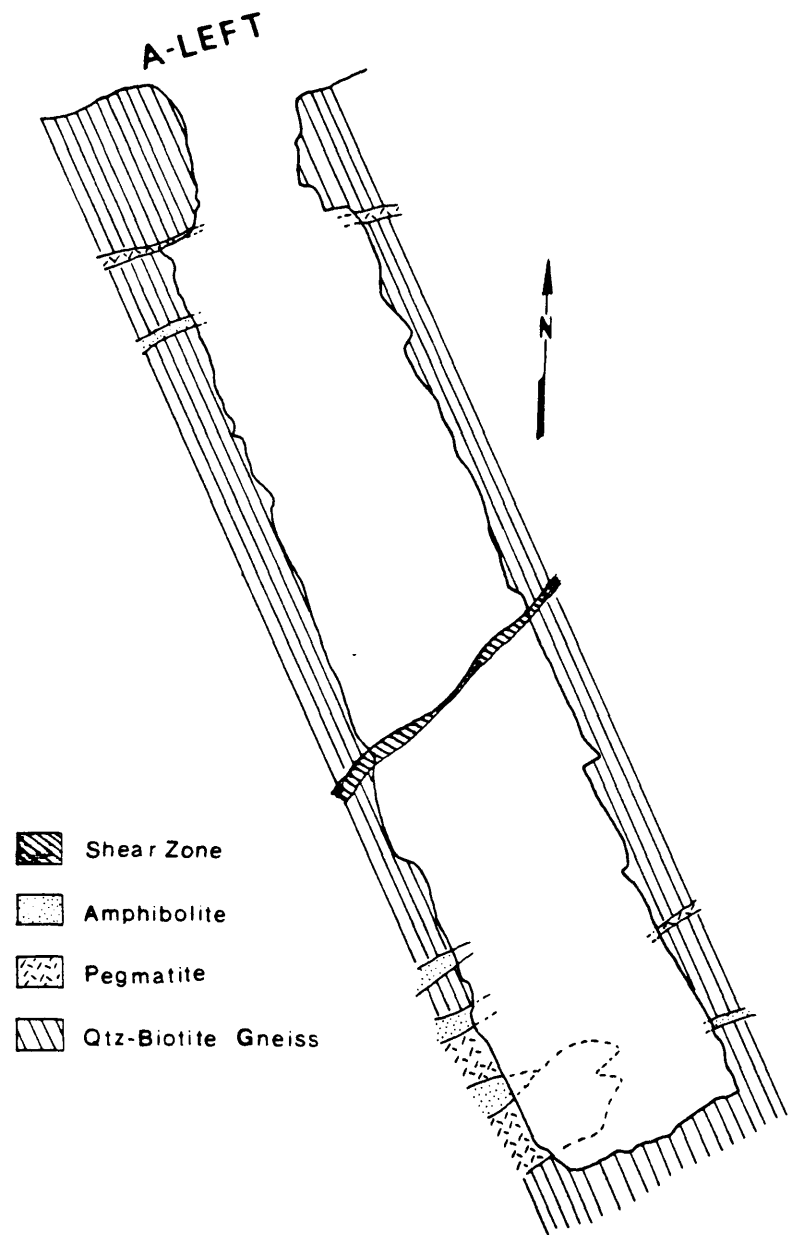


Figure 3.2 Geology of the experimental room.
(Abstract, Rosasco, 1981).

This nature of rock fracturing does not define regular structural blocks, and this was emphasized by the excellent stability of the room. The only shear zone intersected the room (see Figure 3.2) was not introduced to the models development since the displacements observed on both sides of the zone have not displayed any remarkable difference.

The homogeneity of the models material were based upon the high percentage of quartz content in the rock mass, even though it is foliated, the rock mass strength was preserved as mechanically homogeneous.

The isotropy of the model property was maintained, since the rock mass modulus values in the horizontal direction and in the vertical direction have a percentage difference of 15% which can be tolerated according to ASTM specifications.

3.3 Plane Strain Model.

This is a finite element model in which the analysis took place in a vertical plan located at the midsection of the room, and perpendicular to its axis. The model analysis predicted the elastic solution; stresses and deformation of the rock mass due to the room creation in the model plane. Two separate models were developed in respect to their loading conditions.

3.3.1 Plane Strain Model with In Situ Stress Loading.

This particular model was subjected to the in situ stress components working on the model plane. For vertical loading, a pressure of 360 psi was applied on the upper boundary of the model. For horizontal loading a pressure of 360 psi was applied on both vertical boundaries of the model.

The Model Properties

The averaged rock mass modulus (determined by CSM-cell testing) of 4.5×10^6 psi, and Poisson's ratio of 0.22, Appendix A, were assigned to the model elements. A three feet thick zone of 3.9×10^6 psi elastic modulus and $\nu = 0.24$ was surrounding the opening. This zone was introduced to simulate for the damaged zone produced by blasting.

The Model Mesh

The model mesh has a dimension of 135 ft. wide and 100 ft. high. The mesh was formed by 364 elements connected together by 347 nodes. The elements configuration were selected to represent the approximate geometry of the room cross section, the distribution of the rock properties around the excavation. The nodal points above the opening were coordinated to coincide with the anchor positions of the roof extensometer in the field case. The model mesh is shown in Figure 3.3.

Model Results

The model was loaded using the in situ stress field in ways. These loading conditions are given below with each case analysis. The model predictions; stress and displacements, which to be compared with the corresponding field measurements are tabulated for each case.

Case A.

The vertical and horizontal stress components of 360 psi were uniformly distributed on the model boundaries. The specific gravity of model elements was not introduced into the analysis. This loading condition is shown in Figure 3.4.

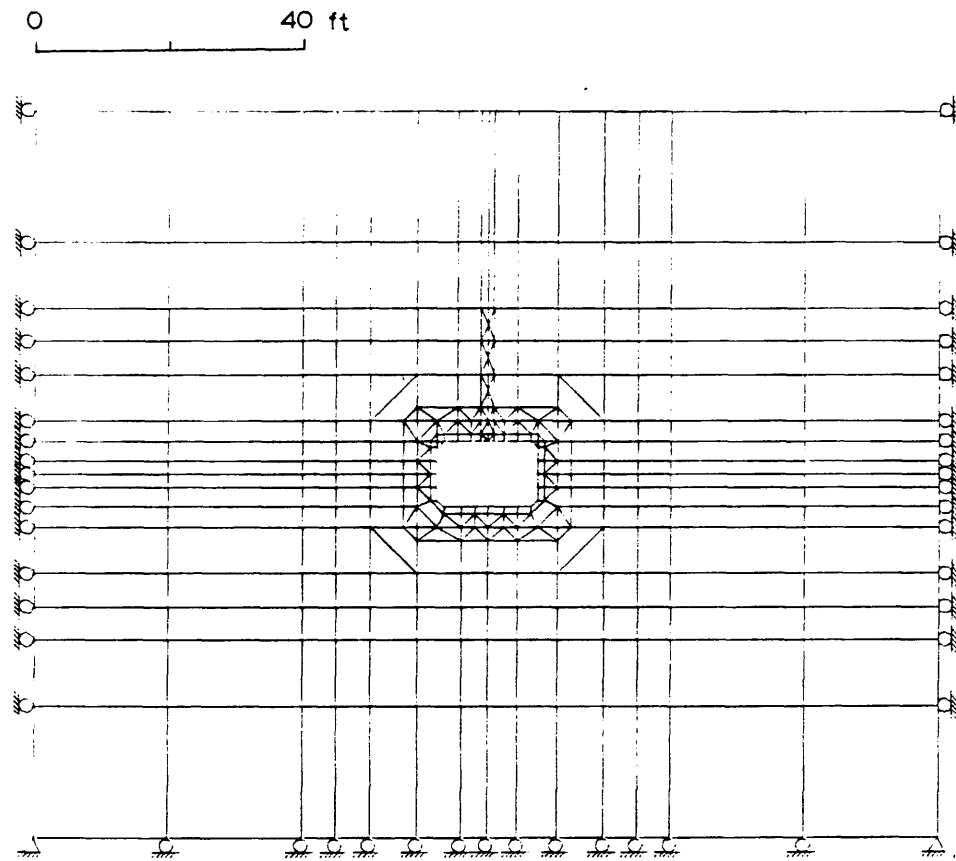


Figure 3.3 In situ stress loading model mesh.

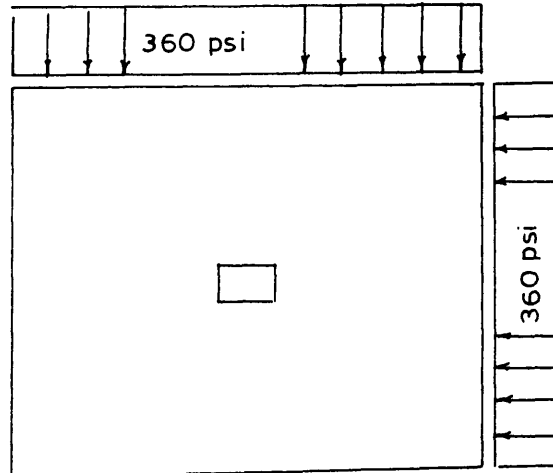


Figure 3. Loading condition (Case A)

Stress and displacements predicted by analysis of

(Case A).

Stress (psi)	Distance from the opening (ft.)					
	1.5	6.5	12.5	17.5	30	50
Radial	38.2	241.2	321.9	340.0	352.9	359.4
Vertical	547.8	566.6	466.9	432.4	405.2	381.5
Deformation in inches						
Roof-floor Convergence	Wall Convergence	Anc.1 (5')	Anc.2 (10')	Anc.3 (15')	Anc.4 (20')	
0.030	0.015	0.013	0.010	0.008	0.007	

Case B.

The loading condition in this case is shown in Figure 3.5. It is assumed that the horizontal stress component was increasing with depth to give 360 psi in the vicinity of

the opening and zero at the surface. The vertical pressure is a combination of gravity loading (rock density = 168 lb/ft.) plus 300 psi applied uniformly at the upper

boundary of the model to give 360 psi at the vicinity of the opening (the component of the in situ field stress).

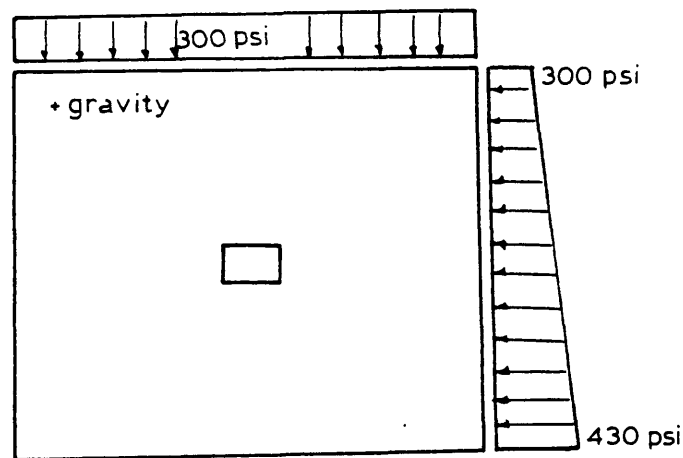


Figure 3.5 Model loading condition (Case B)

The stresses and the displacements produced by this case analysis are as follows:

Stress (psi)	Distance from the opening (ft.)					
	1.5	6.5	12.5	17.5	30	50
Radial	39.1	244.7	324.9	342.3	354.8	359.6
Vertical	565.3	580.3	478.4	444.2	418	396.0
Deformation in inches						
Roof-floor Convergence	Wall Convergence	Anc.1 (5')	Anc.2 (10')	Anc.3 (15')	Anc.4 (20')	
0.030	0.015	0.013	0.010	0.008	0.007	

By comparing the results of the above cases, it can be noticed that the difference of the loading conditions, whether the horizontal stress was uniformly distributed (Case A), or increasing with depth (Case B), and the vertical stress was compensated by gravity loading in Case B. The displacements were the same. There is only a slight effect on the produced stresses which could be insignificant.

The stress distribution around the opening generated by the plane strain model are shown in Figure 3.6, Figure 3.10.

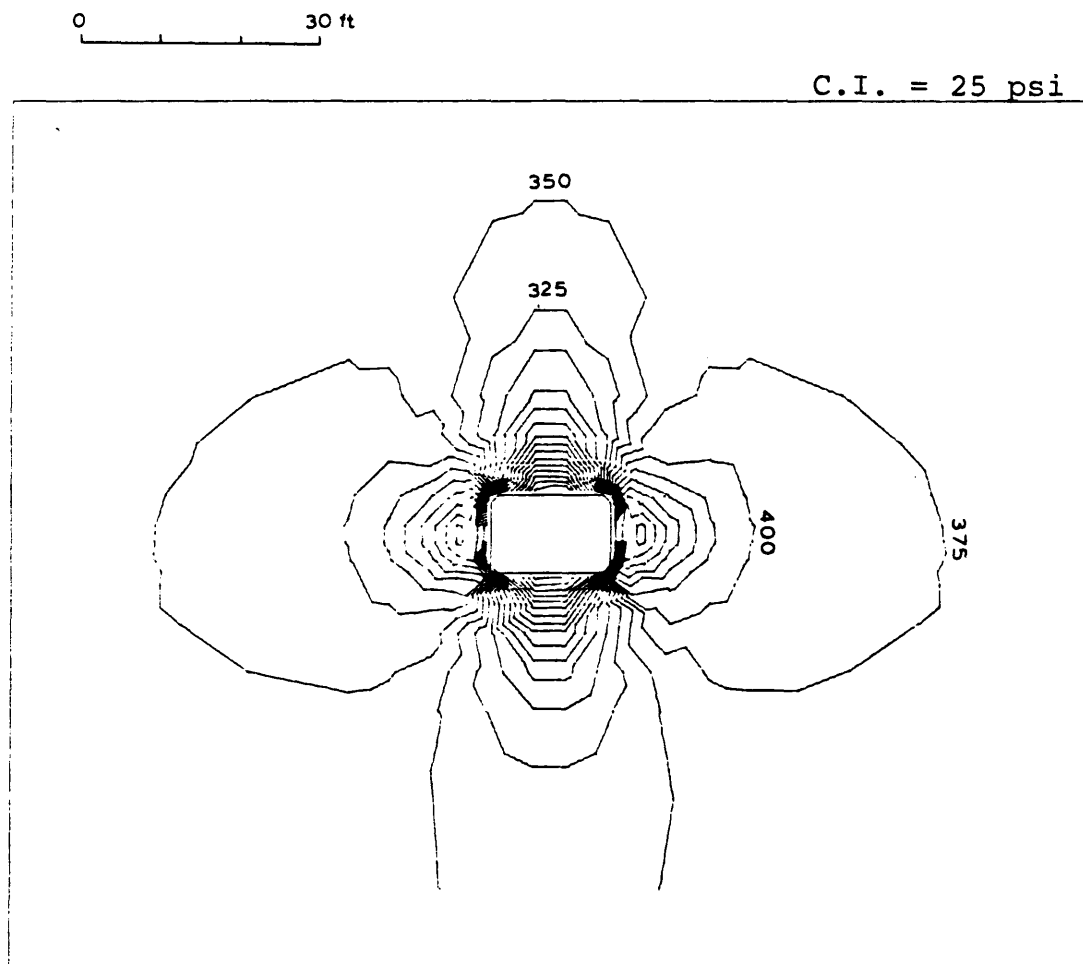


Figure 3.6 Vertical stress contour plot.

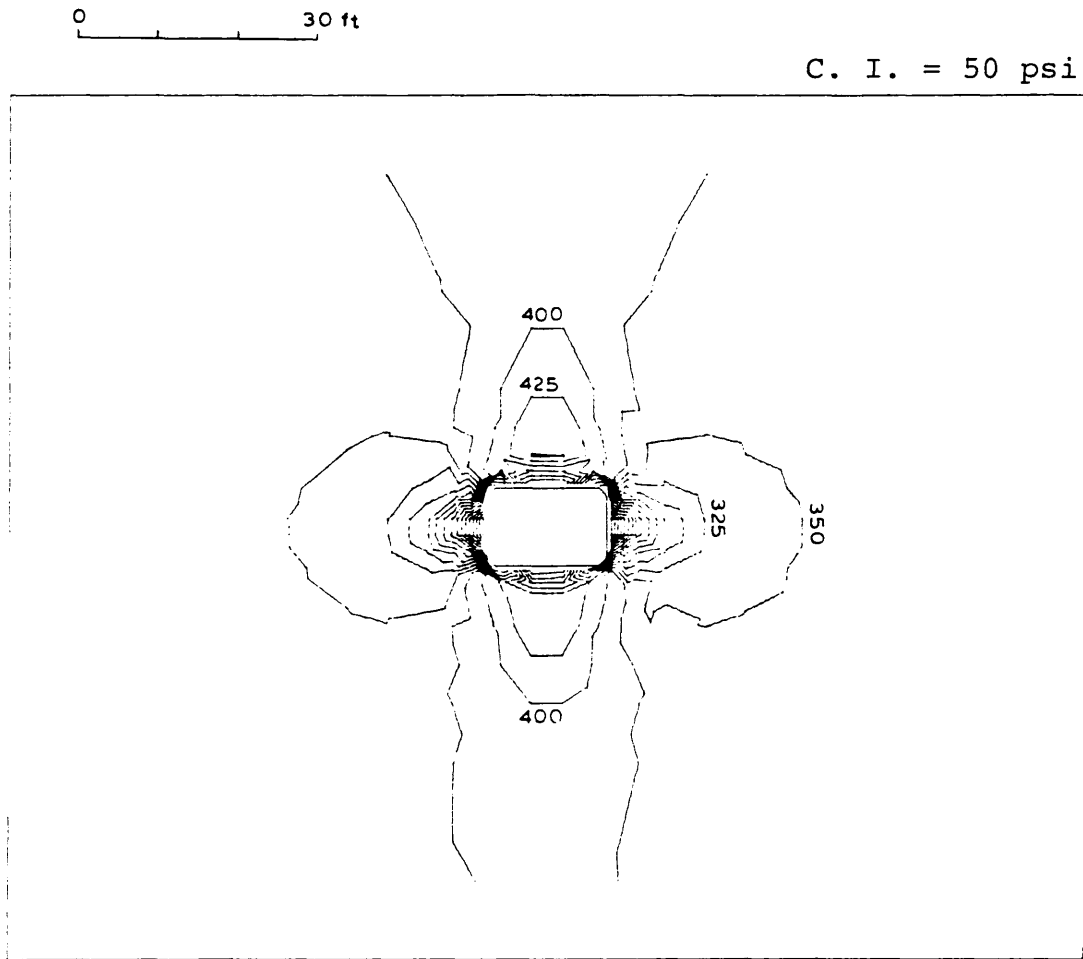


Figure 3.7 Horizontal stress contour plot.

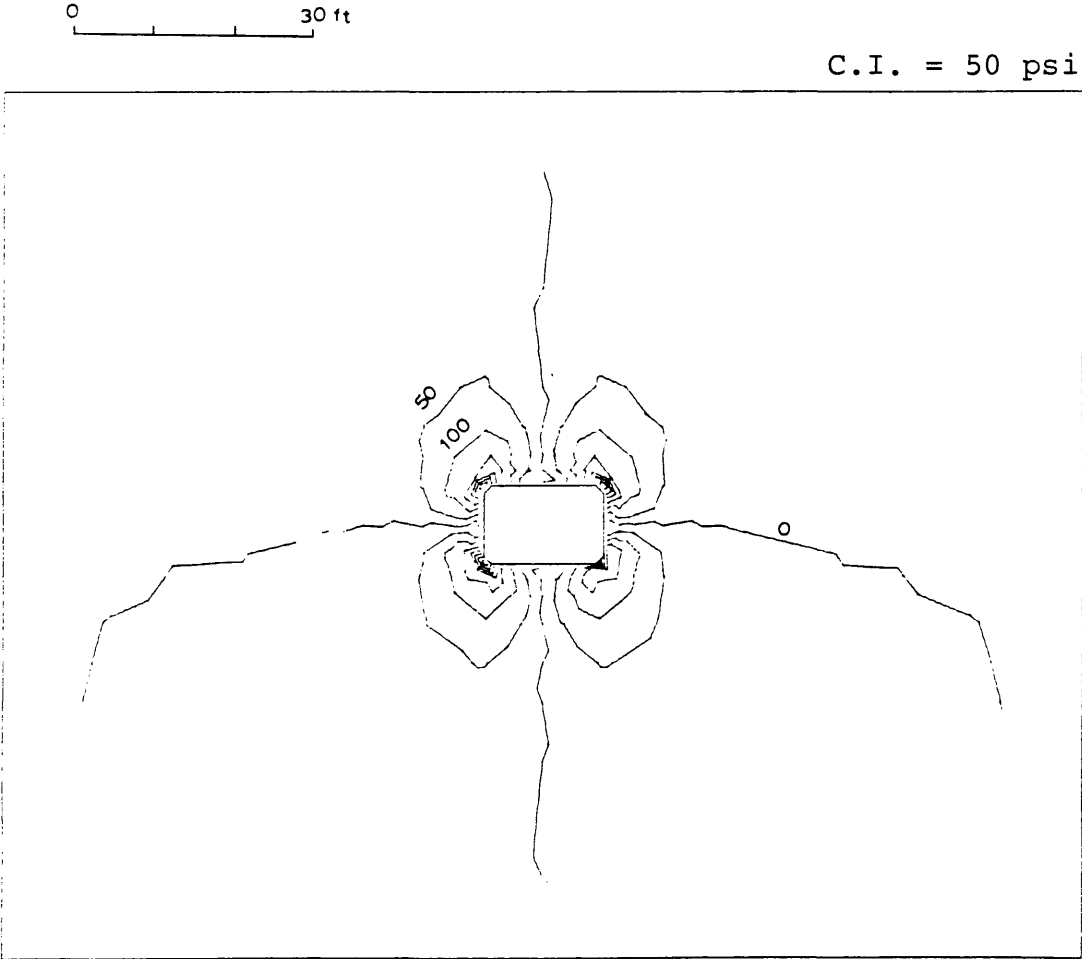


Figure 3.8 Shear stress contour plot.

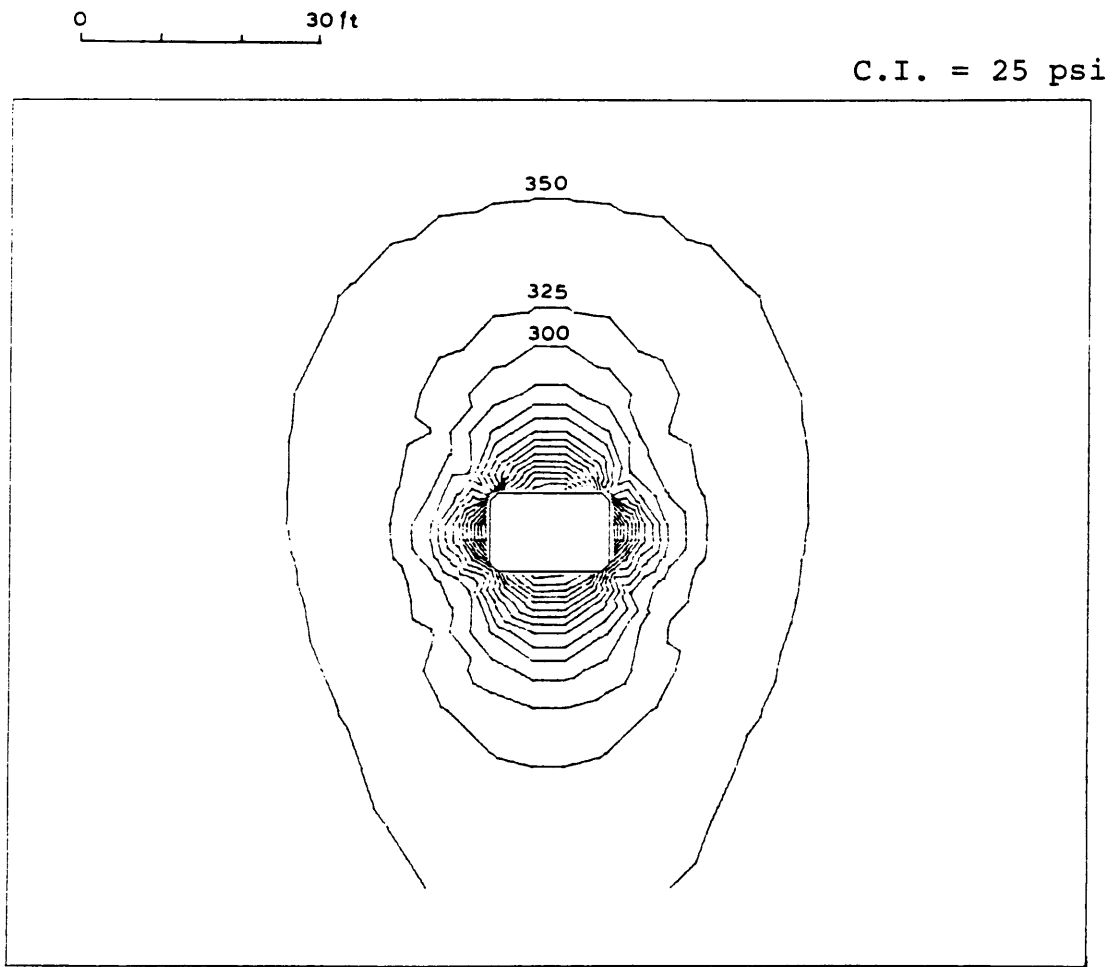


Figure 3.9 Maximum principal stress contour plot.

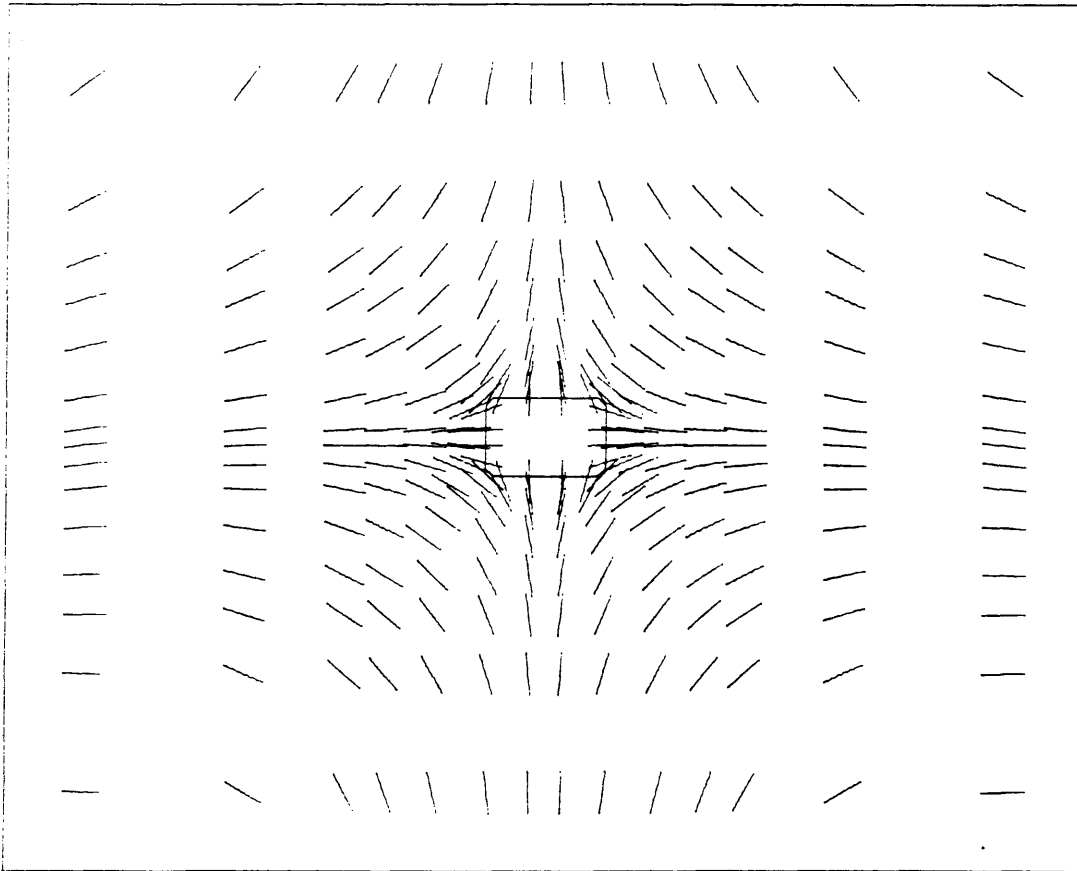


Figure 3.10 Maximum principal stress direction plot.

3.3.2 Plane Strain Model with Gravity Loading.

This model has been developed to analyze the room behavior, if the in situ stress field is not known. The model size in this case was chosen to allow for gravity loading, i.e. the area of interest has extended to the surface of the mountain. The model mesh used for this analysis is shown in Figure 3. The model was analyzed in four different cases: Case 1, Case 2, Case 3 are gravity loading condition with different rock properties, and in Case 4, the horizontal component of the in situ stress field is introduced in the analysis. The results associated with these cases are given below:

Case 1:

The model elastic constant = 4.5×10^6 psi (the average of the rock mass modulus)

Poisson's ratio = 0.22 , The rock density = 168 lb/ft³

Stress (psi)	Distance from the opening (ft.)					
	5	10	15	25	40	50
Radial	103.4	115.2	110.8	104.5	100.0	98.4
Vertical	490.1	389.6	359.5	344.0	336.3	334.3

Deformation in inches

Roof-floor convergence	Wall convergence	Anc. 1 (5ft)	Anc. 2 (10ft)	Anc. 3 (15ft)	Anc. 4 (20ft)
0.024	0.001	0.010	0.008	0.006	0.005

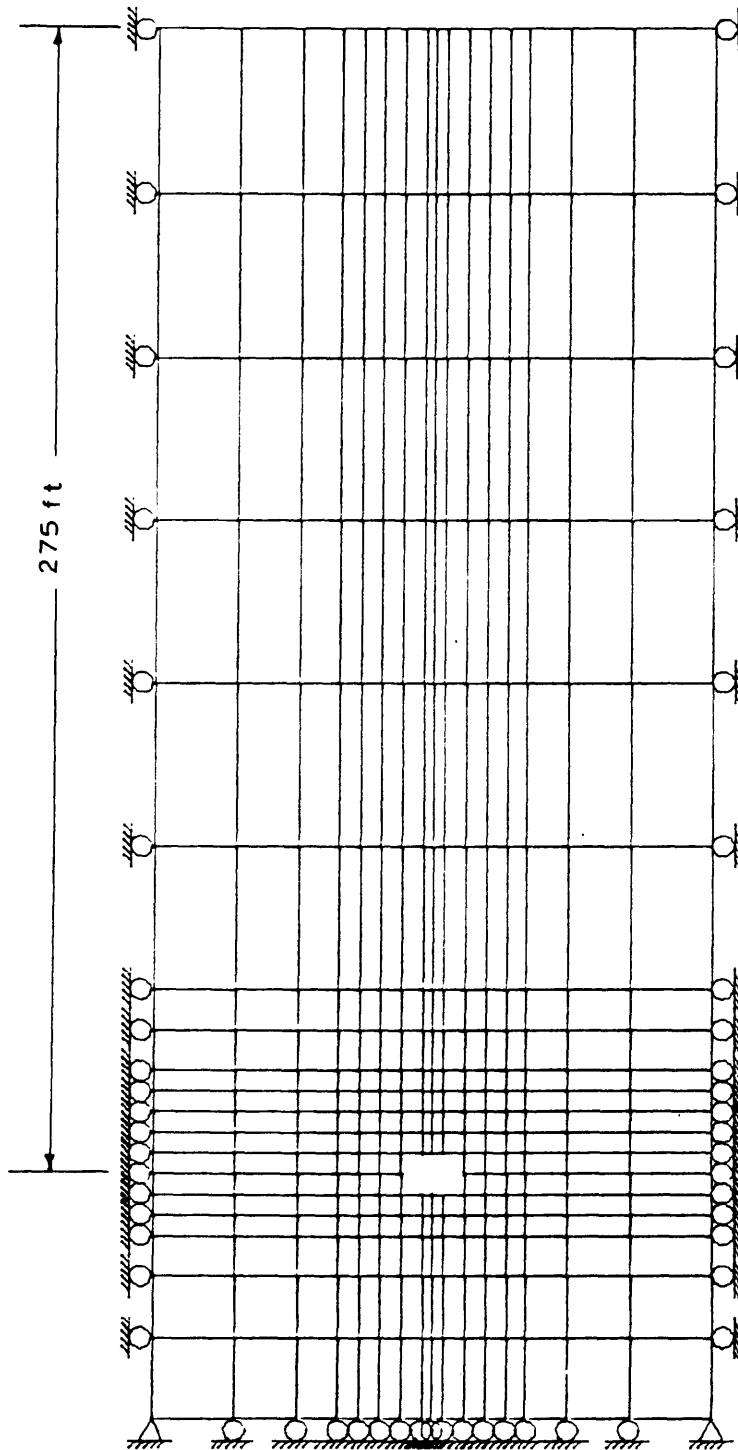


Figure 3.11 Gravity Loading Model Mesh.

Case 2:

The model elastic constant = 9.0×10^6 psi (the average of laboratory elastic constant)

Poisson's ratio = 0.22

Rock density = 168 lb.ft.³

Stress (psi)	Distance from the opening (ft.)					
	5	10	15	25	40	50
Radial	103.4	115.2	110.8	104.5	100.0	98.4
Vertical	490.1	389.6	359.5	344.0	336.3	334.3

Deformation in inches

Roof-floor convergence	Wall convergence	Anc.1 (5ft)	Anc.2 (10ft)	Anc.3 (15ft)	Anc.4 (20ft)
0.013	0.0005	0.005	0.004	0.003	0.003

Comparing the results of Case 1, and Case 2, it can be found that the displacement of the rock mass towards the opening is inversely proportional to the elastic constant used in the analysis, but the change of this constant has no effect on the distribution of the stresses around the opening.

Case 3:

The model elastic constants = 4.5×10^6 psi, $\nu = 0.22$

The opening is surrounded by a 5 ft. zone of rock mass and has an elastic constant of 3.9×10^6 psi.

The model is gravity loaded due to a rock density of
 = 168 lb./ft.³.

Stress (psi)	Distance from the opening (ft.)					
	5	10	15	25	40	50
Radial	113.1	123.8	121.8	118.5	110.4	108.5
Vertical	471.5	391.3	363.2	350.4	336.0	334.5

Deformation is inches.

Roof-floor Convergence	Wall Convergence	Anc.1 (5')	Anc.2 (10')	Anc.3 (15')	Anc.4 (20')
0.026	0.002	0.011	0.008	0.006	0.005

The results of this case have shown that by introducing a zone of lower modulus around the room, the vertical stress component has dropped slightly within the zone thickness, and the horizontal stress component was higher than those obtained in Case 1, and Case 2. Furthermore, the lower modulus zone has increased the displacement of the rock mass which has fallen within this zone thickness, the roof-floor convergence, wall-wall convergence and Anc.1.

Case 4:

In this case the vertical component of topography influence 41.5 psi is simulated as an external pressure applied uniformly on the upper boundary of the model. The horizontal pressure was also introduced to the analysis, and it was assumed to be linearly increasing with depth to

give 360 psi at the vicinity of the opening. This loading condition is shown in Figure 3.12 the model properties as in Case 1.

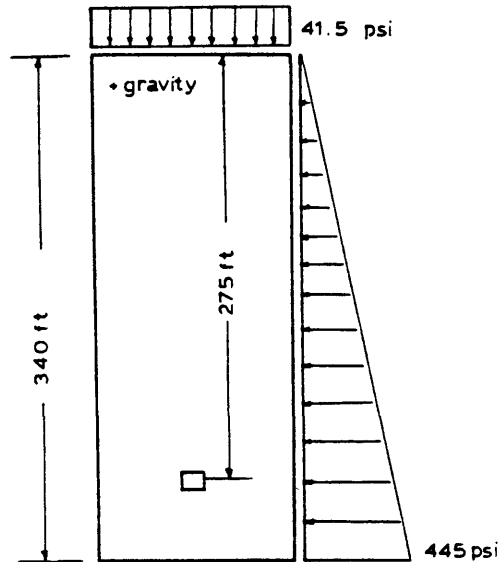


Figure 3.12. Model loading condition, Case 4.

The results produced by Case 4 are given below.

Distance from opening (ft.)						
Stress (psi)	5	10	15	25	40	50
Radial	249.7	308.2	335.6	351.4	358.9	360.4
Vertical	513.5	452.9	422.5	408.5	407.2	409.5
Deformation in inches						
Roof-floor Convergence	Wall Convergence	Anc.1 (5')	Anc.2 (10')	Anc.3 (15')	Anc.4 (20')	
0.027	0.018	0.011	0.008	0.006	0.005	

Comparing the results of Case 4 with those cases where the horizontal stress was applied, it can be seen that the model mesh size has affected both the displacements and the stresses. The difference in the vertical stress component was more remarkable than in the radial component.

General conclusions drawn by comparing all plane strain model displacements:

- a) The roof-floor convergence is ranging between 0.024 to 0.030 inches and it is a summation of the roof sag and the floor heave.
- b) The wall-wall convergence is greatly dependent upon the magnitude of the applied of the horizontal stresses:
For gravity loading = 0.001 inches (Case 1)
For stress loading = 0.015 inches (Case A)
- c) The relative movement of the shallower anchor's positions to the deepest anchor have the same values whether the model was stress loaded or gravity loaded:

	<u>Anc. 1</u>	<u>Anc. 2</u>	<u>Anc. 3</u>
Stress loading	6	3	1
Gravity loading	5	3	1

and the 20 ft. position anchor has displaced 0.006 ± 0.001 inches.

3.4 Axisymmetry Model.

The room excavation technique has been modeled using finite element analysis. This model was analyzed as an

axisymmetry case in which the room will be presented as deepening a hole in a rock mass cylinder. The model can estimate and display the behavior of the rock mass towards the excavation rate.

The Model Configuration.

The model is a vertical plane crossing the room longitudinally and to be rotated around the room long axis to form a rock mass cylinder of 200 ft. long and 120 ft. in diameter. The central part of this cylinder was removed in steps to simulate the rate of advance in the field case, and eventually the room was formed as cylindrical cavity of 12.5 ft. in diameter. The locations of instruments, and the blast faces are marked in this configuration as shown in Figure 3.13.

The Model Mesh.

The model mesh selected for this analysis is shown in Figure 3.14. The mesh was formed by 377 elements connected by 420 nodes. The nodes coordinates were selected to represent the instruments location in the room (convergence stations, and the extensometer's anchors). The elements sizes of the vicinity of the room will allow their removal to represent a blast (face advance).

The nodes at the axis of the room are restrained to any vertical motion.

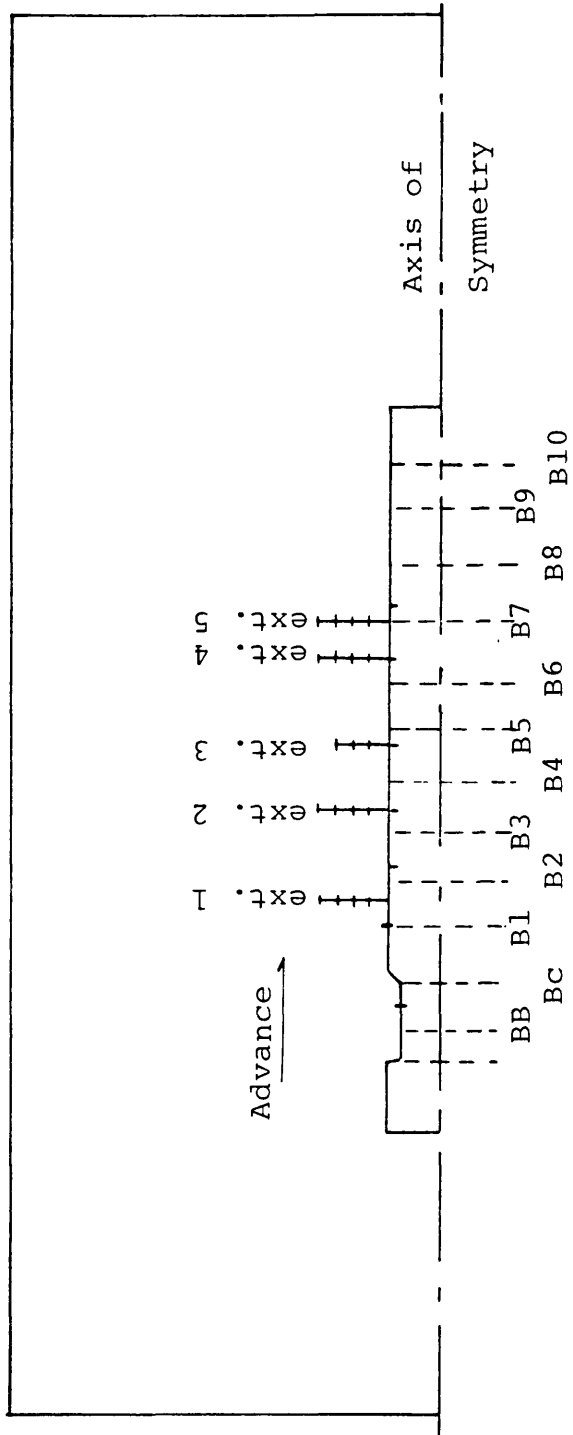


Figure 3.13 Configuration of axisymmetry model.

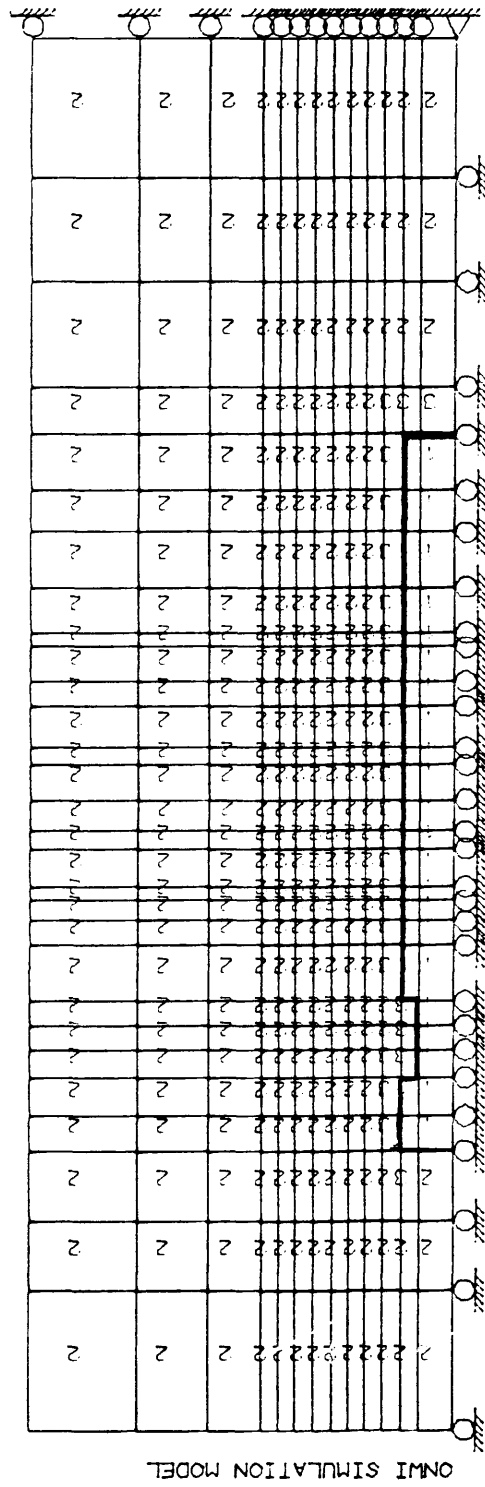


Figure 3.14 Axisymmetry Model Mesh.

The Model Loading Condition.

The in situ stress field components were used to load the model. Three hundred sixty psi was distributed uniformly on the outer boundary of the model representing the horizontal and the vertical in situ stress components. Four hundred eighty psi was applied on the vertical boundary of the model to work parallel to the room axis. These loading conditions combinations will put the axisymmetry model under triaxial stress field.

The Model Properties.

The average rock mass modulus (4.5×10^6 psi) was assigned to the model elements prior to the room excavation. During the room excavation a zone of 2.5 ft. of 3.9×10^6 psi elastic constant was surrounding the excavation after each blast.

Axisymmetry Model Results.

The results produced by this model are the displacements representing the convergence stations, and the displacements of the extensometer's anchors following each blast.

Since the room excavation has been simulated as a hole (cross-section is a circle, radius = 6.25 ft.) in a rock mass cylinder, two points should be taken into consideration:

- a) the results from the model would be strictly an approximation of the actual case;
- b) the roof-floor convergence, and the wall-convergence will be equal in a circular model.

The displacements predicted by this analysis are given in Tables 3.1 through 3.6 for the room convergence and the extensometers. The position where the instrument is exposed, i.e. the face just past the instrument is marked, and also the instrument installation time is given in these tables.

Table 3.1 Axisymmetry Model Results.(Total convergence x 10^{-3} inches)

Blast	C1	C2	C3	C4	C5	C6	C7
BA	1.2	0	0	0	0	0	0
BB	6.4←	1.4	0	0	0	0	0
BC	9.4	3.2	0	0	0	0	0
B 1	10.2*	14.2←	1.6	1.4	0	0	0
B 2	10.6	16.2*	3.2	3.4	1.2	0	0
B 3	10.6	17.0	14.6←*	14.2←	2.6	0	0
B 4	10.6	17.4	17.0	15.4*	14.6←	1.4	0
B 5	10.6	17.6*	18.4	17.8	17.4	2.0	2.4
B 6	11	17.6	18.6	18.6	18.2*	14.6←*	3.6
B 7	11	17.8	18.6	18.8	18.6	17.4	15.6←
B 8	11	17.8	18.8	19.0	19.0	18.2	17.8*
B 9	11	17.8	18.8	19.0	19.2	18.6	18.4
B10	11	17.8	18.8	19.0	19.2	18.8	18.8

←: Station's location was exposed.

*: Convergence station is installed (data missed to be recorded by the instrument).

BA, BB, and BC: Regular blasts to drive the room entry.

The above given displacement predictions have shown the following:

- a) The convergence predicted for C1 was the minimum with a final convergence of 0.011 inches.
- b) The final convergence calculated for stations C2 to C7 have the same value 0.019 ± 0.001 inches.
- c) The biggest displacement occurred at the instrument position once it was exposed to the room.
- d) The convergence increases with the advance during the next three blasts only, and any more advance had no significant effect on the instrument's position and the convergence reading was stabilized.

The predicted movements of the extensometers' anchors by the model is given in Tables 3.2 through 3.6. The movements given in the tables are the total displacement which occurred at the anchor positions during the excavation.

(The movements x 10^{-3} inches)

Table 3.2 Axisymmetry Model Results.

(Extensometer No. 1)

Blast	Anc.1	Anc.2	Anc.3	Anc.4	Remarks
BA	0	0	0	0	
BB	0.7	0.4	0.3	0.3	
BC	1.2	0.9	0.7	0.6	
B 1	2.7	1.8	1.2	1	Position exposed
B 2	4.5	2.8	1.9	1.4	Instrument installed
B 3	5.1	3.4	2.3	1.9	
B 4	5.3	3.6	2.5	2.1	
B 5	5.5	3.8	2.8	2.3	
B 6	5.6	3.9	2.9	2.4	
B 7	5.6	4	3	2.5	
B 8	5.6	4	3	2.5	
B 9	5.6	4	3	2.5	
B10	5.6	4	3	2.5	

Table 3.3 Axisymmetry Model Results.

(Extensometer No. 2)

Blast	Anc.1	Anc.2	Anc.3	Anc.4	Remarks
BA	0	0	0	0	
BB	0	0	0	0	
BC	.4	.4	.3	.3	
B 1	.8	0.7	0.6	.6	
B 2	1.5	1.2	0.9	.9	
B 3	3.4	2.2	1.6	1.3	Position exposed
B 4	5.4	3.6	1.9	1.8	Instrument installed
B 5	5.5	3.7	2.4	1.9	
B 6	5.6	3.8	2.9	2.4	
B 7	5.7	4.0	3.1	2.6	
B 8	5.8	4.1	3.2	2.6	
B 9	5.8	4.1	3.2	2.6	
B10	5.8	4.1	3.2	2.6	

Table 3.4 Axisymmetry Model Results.

(Extensometer No. 3)

Blast	Anc.1	Anc.2	Anc.3	Remarks
BA	0	0	0	
BB	0	0	0	
BC	0	0	0	
B 1	.2	.4	.3	
B 2	.6	0.6	0.6	
B 3	1.1	1.1	0.9	
B 4	3.3	2.7	2.1	Position exposed
B 5	4.3	3.2	2.3	
B 6	5.3	3.6	2.6	Instrument installed
B 7	5.5	4.0	3.0	
B 8	5.7	4.1	3.1	
B 9	5.7	4.2	3.2	
B10	5.7	4.2	3.2	

Table 3.5 Axisymmetry Model Results.

(Extensometer No. 4)

Blast	Anc.1	Anc.2	Anc.3	Anc.4	Remarks
BA	0	0	0	0	
BB	0	0	0	0	
BC	0	0	0	0	
B 1	0	0	0	0	
B 2	0	.3	.2	.4	
B 3	0.4	.5	.4	.5	
B 4	0.8	0.9	.8	0.9	
B 5	1.5	1.4	1.4	1.2	Position exposed
B 6	3.4	2.4	1.8	1.6	Instrument installed
B 7	4.9	3.4	3.2	2.1	
B 8	5.4	3.8	3.5	2.4	
B 9	5.5	3.9	3.6	2.6	
B10	5.6	4.2	3.8	2.7	

Table 3.6 Axisymmetry Model Results.

(Extensometer No. 5)

Blast	Anc.1	Anc.2	Anc.3	Anc.4	Remarks
BA	0	0	0	0	
BB	0	0	0	0	
BC	0	0	0	0	
B 1	0	0	0	0	
B 2	0	0	.2	.2	
B 3	0	.5	.3	.3	
B 4	.7	.9	.7	.8	
B 5	1.4	1.1	1.1	1.1	
B 6	1.8	1.7	1.3	1.2	
B 7	4.2	3.0	2.1	1.7	Position exposed
B 8	5.2	3.7	2.7	2.1	Instrument installed
B 9	5.3	4.0	2.9	2.4	
B10	5.5	4.1	3.1	2.6	

The displacements calculated by axisymmetry model for the extensometer's anchors have shown the following:

- a) The anchors behavior towards the advance rate were qualitatively and quantitatively the same for all extensometers, their movements were gradually increasing as the face advanced. They stabilized approximately 23 ft; i.e. three rounds or faces past the instrument's position.
- b) The final relative movement of the shallower anchors were similar for all extensometers and they can be averaged to:

Anchor	Displacement $\times 10^{-3}$ inches
Anchor 1	3
Anchor 2	1.5
Anchor 3	0.7

The stresses component's calculated by the axisymmetry model are the radial and the tangential components, i.e. the horizontal components perpendicular and parallel to the room axis. Table 3.7 gives the final stress components magnitudes versus the distance from the room wall.

Table 3.7 Axisymmetry Model Results.

(stresses versus depth)
(+) compression

Distance from the opening (ft.)	Stresses in psi	
	Radial	Tangential
1.25	55	586
3.75	191	527
6.25	248	472
8.75	280	440
11.25	300	420
13.75	314	406
16.25	324	397
18.75	331	390
23.75	341	381
32.5	351	373
48	358	365

3.5 Model Validation.

Model validation can be accomplished by comparing the predicted results with those corresponding measurements in the field case. Since there are two different types of models in this study, the models' results should be combined to give the correct predicted data to be used in such comparisons. Even though the type of the analysis and the loading conditions were different for both models, their results can be fairly comparable:

	Plane Strain Model		Axisymmetry Model			
Applied Stresses	$\sigma_x = \sigma_y = 360$ psi		$\sigma_x = \sigma_y = 360$ psi $\sigma_z = 480$ psi			
Room Geometry	Rectangular 15 x 10 ft.		Circular 12.5 ft. in dia.			
Convergence	Roof-floor 0.030 Wall-wall 0.015		0.019 inches			
Relative anchor movement	Anc. 1: 0.005 Anc. 2: 0.003 Anc. 3: 0.001		0.003 0.002 0.001			
Calculated stresses	(Distance, ft.)	σ_H	σ_V	σ_H	σ_V	
	1.5	39	548	55	580	
	6.5	245	566	248	472	
	12.5	325	467	310	410	
	17.5	352	432	327	395	
	30	355	405	351	373	
	50	360	381	358	365	

The above comparison has shown a slight difference between the two models. This can be mainly due to the difference in the room geometry analyzed by both models.

The predictions of the plane strain model are considered to be more acceptable to be compared with the field measurements, because the room geometry was adequately simulated in this model, so that the models validation will be based upon this fact and the axisymmetry model results (especially the displacement) will be adjusted to give the final displacements given by the plane strain model.

Models validation comprises stresses comparison and displacements comparison.

3.5.1 Stress Validation.

The comparison between the stresses (predicted and measured) can best be shown by a graphical representation of both. The predicted stresses are the radial (horizontal and perpendicular to the room axis), and the vertical components. The source of the predicted stresses is the plane strain model.

The measured stress components using CSIRO cell and USBM gage were used in this validation.

Figure 3.15 shows the measured vertical stress component and the calculated stress component at different distances from the room contour, and Figure 3.16 shows the radial stresses.

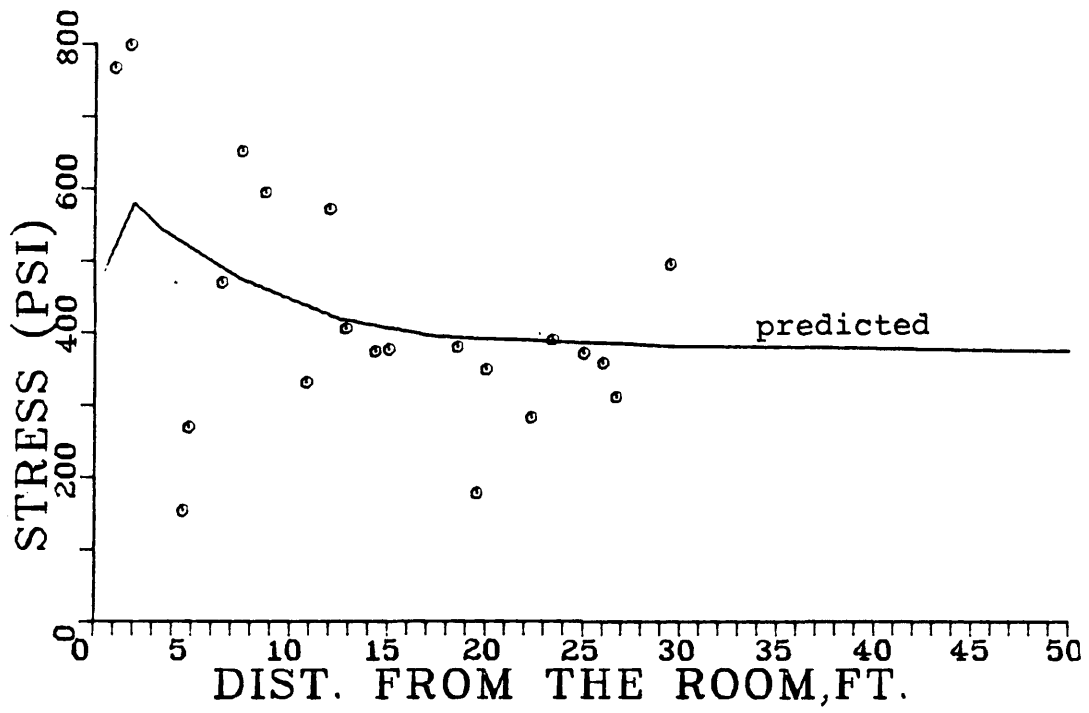


Figure 3.15 Vertical stress component (measured and predicted).

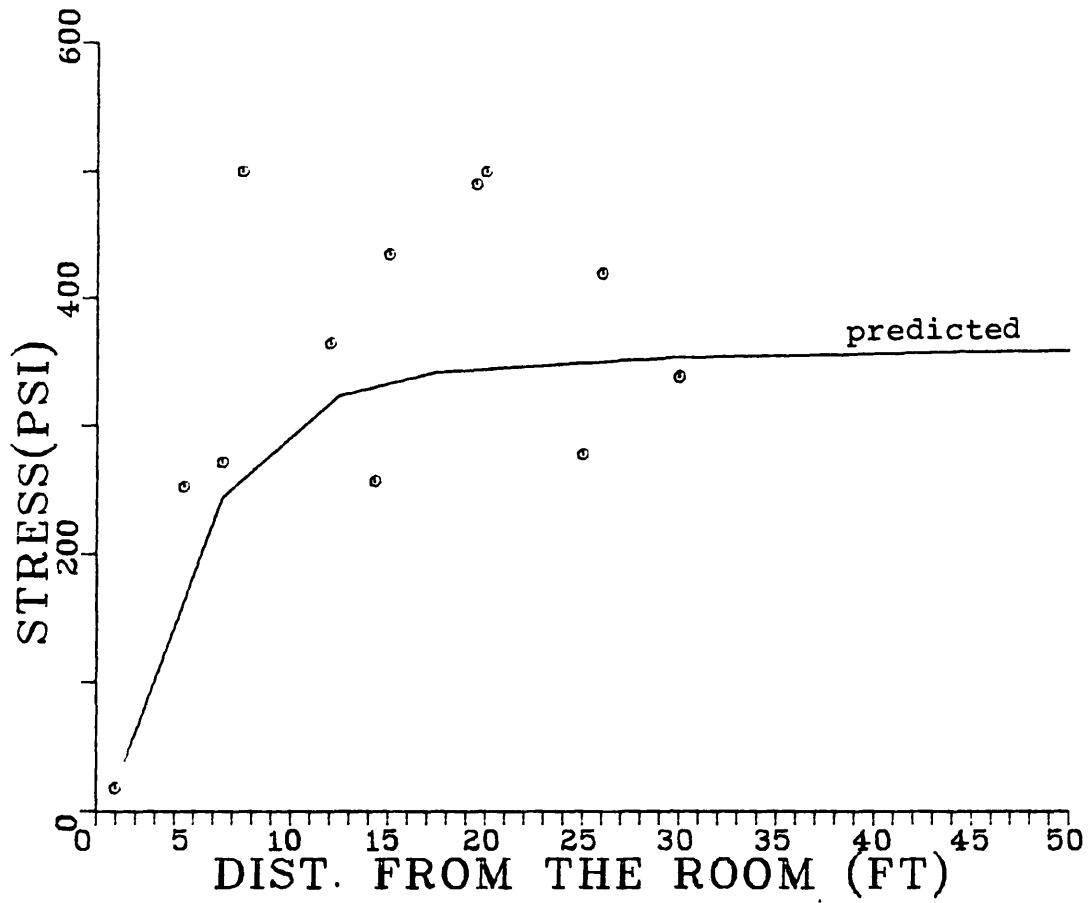


Figure 3.16 Radial stress component (measured and predicted).

It can be concluded from graphical comparison of the stresses, the stress change away from the room contour can best be simulated by the finite element analysis, even though the idealized approximation used in the analysis.

3.3.2 Displacements Validation.

The comparison between the predicted displacements and the measured displacements is not a direct comparison of numbers. The predicted displacements produced by the plane strain model is the final elastic movements of the rock mass towards the opening, and this is corresponding to the final stabilized movement calculated by the axisymmetry model. Since the calculated displacements by the plane strain model are more accurate than those produced by the axisymmetry model because of the room geometry, the displacements produced by the axisymmetry model will be adjusted as follows: the room was simulated as hole of 12.5 ft. in the axisymmetry model, which is the diameter resulting from the averaging of the real cross section dimensions of the room, 15 x 10 ft. Comparing the final convergence values predicted by the models, it is found:

	<u>Plane St. Model</u>	<u>Axi. Model</u>
Roof-floor Conv.	0.030	0.020
Wall-wall Conv.	0.015	0.020

It can be seen that the average convergence calculated by both models is nearly the same; hence, to adjust the final roof-floor convergence predicted by the axisymmetry model all values should be multiplied by a factor of 1.5 to give a final convergence of 0.030 inches, and the wall-wall convergence readings predicted by the axisymmetry model was reduced by a factor of 75% to agree with the final results of the plane strain model. Similarly, the displacements produced by the axisymmetry model for the extensometer's anchor were treated the same way. The multiplication factors used to adjust the anchor's displacement predicted by the axisymmetry model were found as follows:

Anchor	Predicted displacement by plane strain model (inches)	Predicted displacement by axisymmetry model (inches)
Anc.1	0.013	0.0058
Anc.2	0.010	0.0042
Anc.3	0.008	0.0032
Anc.4	0.007	0.0027

The factors were found by dividing the displacements predicted by the plane strain model by the displacements predicted by the axisymmetry model. These factors are listed below:

for Anc. 1 = 2.24

Anc. 2 = 2.38

Anc. 3 = 2.50

Anc. 4 = 2.59

It should be mentioned that the above calculations were just a rough approximation method to adjust the axisymmetry model results, and to compensate for the room geometry defect in the axisymmetry model.

After the above adjustments were made, the displacements now should be put in the form to be compared with the field measurements; i.e. subtracting the data which have not been recorded by the instruments in the field case, and predicted by the model. The final predicted displacements to be compared with the field measurements are given in Tables 3.8 through Table 3.10, followed by the actual field measurements.

Table 3.9 Predicted Relative Movement of the Roof Comparable to the Field Measurements $\times 10^{-3}$ inches.

Predicted Values										
Extensometer No. 1										
Advance	B1	B2	B3	B4	B5	B6	B7	B8	B9	B10
Anc. 1	-	-	.2	.2	.2	.2	0	0	0	0
Anc. 2	-	-	.2	.2	.2	.2	.2	.2	.2	.2
Anc. 3	-	-	-.2	-.2	0	0	0	0	0	0
Extensometer No. 2										
Anc. 1	-	-	-	-	0	0.9	-2	-2	-2	-2
Extensometer No. 3										
Anc. 1	-	-	-	-	-	-	-.4	-.2	-.4	-.4
Anc. 2	-	-	-	-	-	-	0	0	0	0
Extensometer No. 4										
Anc. 1	-	-	-	-	-	-	2.2	2.7	2.5	2.5
Anc. 2	-	-	-	-	-	-	1.1	1.3	1.1	1.6
Anc. 3	-	-	-	-	-	-	2.0	2.0	1.8	2.0
Extensometer No. 5										
Anc. 1	-	-	-	-	-	-	-	-	0.4	-.4
Anc. 2	-	-	-	-	-	-	-	-	0	-.2
Anc. 3	-	-	-	-	-	-	-	-	-.2	-.2

It can be seen from the above comparison tables that the predicted displacements and the measured displacements were not in a good agreement with each other. This kind of result can be expected in such kind of step by step comparison for the following reasons:

- a) The displacements given by the model were the elastic response of the rock mass, unlike the displacements measured at the field which included non-elastic displacements due to movements along the joints.
- b) The measured displacements magnitudes were varied relative to the blasting time, i.e. the reading changes by time which thing can not be introduced in such models.
- c) The idealized assumptions associated with the models development.
- d) The late installation of the field instrumentation.

It can be concluded from the displacements comparison that the model predictions were lower than the field measurements and the agreement between them is poor.

3.4 Model Application.

Application of any mathematical model is a final step which varies from one case to another depending upon the interest of the investigation and the planned future work in the field case. The level of confidence of the model application results is totally dependent upon the agreement between computed results and the real measurements, i.e. model validation. In this particular case, the stress distribution around the room and perpendicular to the radial NX-boreholes is of interest to many other investigations, and since the model stresses predictions were highly agreeable with those corresponding measurements, the other predicted stresses which have no corresponding field data can be sorted out to be used with the same level of confidence.

The NX-radial boreholes configuration in the room are shown in Figure 3.17.

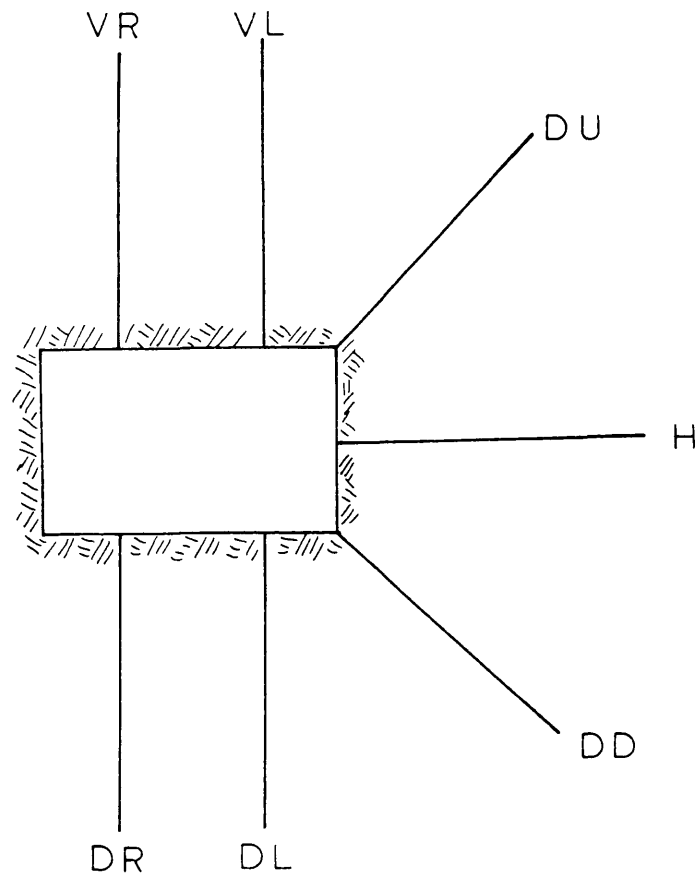


Figure 3.17. NX-Radial Boreholes Configuration.

The components of stresses predicted by the plane strain model in two dimensional representation, perpendicular and parallel to the NX-boreholes axis are given below:

Explanation:

Dist.: Distance measured from the hole mouth.

σ_p : Predicted stresses perpendicular to the hole axis

σ_L : Predicted stresses along the borehole

τ_{PL} : Shear stresses on PL plane

(+): Compressive stress, (-) tensile stress.

Borehole H

Dist., ft.	.5	2	4	7.5	12.5	17.5
σ_p	486	533	548	484	427	403
σ_L	-3	91	192	282	328	344
τ_{PL}	-5	-16	-21	-25	-23	-23

Borehole DU

Dist., ft.	.5	1.7	3.5	5.2	8.5	12.5	17.5
σ_p	811	576	530	445	436	402	394
σ_L	128	214	275	303	312	320	322
τ_{PL}	-30	-30	-29	-25	-23	-21	-21

Borehole DD

Dist. ft.	.5	2	5	8.5	13	18.5
σ_P	804	572	493	415	411	383
σ_L	140	226	287	315	351	367
τ_{PL}	35	-8	-14	-8	1	9

Due to the symmetry of the model the predicted stress for boreholes VR and VL are the same, and also for boreholes DR and DL.

Borehole VR or VL

Dist., ft.	.5	2	4	7.5	12.5	17.5
σ_P	354	380	431	411	391	374
σ_L	74	149	209	260	296	319
τ_{PL}	-95	-125	-119	-84	-52	-35

Borehole DR or DL

Dist., ft.	.5	2	4	7.5	12.5	17.5
σ_P	401	400	437	433	426	417
σ_L	39	110	188	243	281	302
τ_{PL}	69	99	90	49	-7	5

Other applications of the model can possibly be achieved such as, applying variable lateral pressures on a cavity in the room floor to simulate an action of radioactive waste material.

4. SUMMARY AND CONCLUSIONS

4.1 Summary.

The experimental room was excavated using the full face advance method with controlled blasting techniques. Different displacement monitoring instruments were installed during the excavation. The position of the instrumentation stations was controlled by the excavation scheduling and the blasting throw. In situ stresses were measured using the USBM gage and the CSIRO cell in three parallel holes of a maximum depth of 30 ft. The rock mass modulus of deformation was determined every foot in 42 NX-4 radial boreholes drilled from the room. NX-CSM cell was built for the modulus determination. The finite element method was used to describe the rock mass response during and after the excavation by two different types of analysis, plane strain modeling and axisymmetry modeling. The field measurements were used to develop and validate the models.

4.2 Field Measurements Conclusion.

Rock Mass Response.

The measured displacements of the rock mass during the excavation were variable, and they are mainly deformations associated with jointing, either opening or closing. The magnitude and the rate of these deformations

have not reflected any serious instability of the rock mass around the room. The relationship between the deformation and the advance rate was not clearly demonstrated by the instrumentations output due to late installation and the jointed nature of rock mass.

In Situ Stresses.

It is concluded from in situ stress data that the results obtained by using both the USBM gage and the CSIRO cell are of great agreement, and the in situ stress field is a combination of topographic stress, gravity, and tectonic stresses. The measurements have also proven the existence of a near stress field which has been created due to the room excavation. The orientation of the principal stresses at the site did not display an obvious relationship with the jointing orientation at the site, while the orientation of measured stresses was controlled considerably by the local jointing features and the rock type at the measuring position.

Rock Mass Modulus.

It is concluded from the rock mass modulus of deformation values determined by the CSM-cell that the pre-existing jointing at the site is predominantly controlling their values; hence, these values can be used with great reliability to detect fractures in the boreholes.

The modulus, 15 ft. around the room, had been averaged in six sections crossing the room to the same value reflecting the consistence of the rock type and the similarity of the structural features. Measurements have shown higher zones of the modulus located within the near stress field, unlike values close to the room contour which have been lowered by the blast damage. The values also show that there is a slight difference between the modulus in the vertical direction and in the horizontal direction.

4.3 Modeling Conclusion.

As a result of modeling analysis it is concluded that the approximate behavior of the rock mass can best be predicted using the finite element method of structural analysis. However, the method results are critically dependent on the accuracy of the input data, its assumptions and the correct interpretation of the output information. The input data for modeling analysis were obtained from the field measurements, rock properties and loading conditions. The assumptions used in the analysis were based upon geological and field measurement information, even though they have idealized the model development, their effect on the model results were noticeable on the predicted displacements and not on the predicted stresses.

The plane strain model has given a good estimation of the stresses distribution around the room and the final elastic displacements of the rock mass to be used in the axisymmetry model analysis. The axisymmetry model results have described the response of the rock mass (displacements) versus the advance rate more qualitatively than quantitatively because the displacements recorded at the field case were a combination of elastic and nonelastic movements which cannot be predicted by any type of models.

4.4 Recommendation for Future Work.

1. The technique of determining the in situ stress field by overcoring process is well known. Different types of gages were used as strain monitoring element in this technique: CSIRO cell is one of those gages which has been recently introduced to measure the strain relieved by overcoring process. More studies could be made to investigate its technique and the results:
 - a. Developing a technique to check the bond between the cell and the rock before the overcoring operation;
 - b. For more fractured rock mass, smaller cell size would be more convenient to be placed between the closed spacing joints;
 - c. The possibility of recovering the cell from the overcores would give the opportunity of using the cell more than one time, and reduce the cost;
 - d. Biaxial compression testing on the overcores produce three elastic constants for the stress calculations, study should be conducted to justify the optimum modulus and can be used for this analysis.
2. The relationship between the rock mass modulus of deformation determined by the CSM cell and the degree of fissuration of the rock mass is qualitatively clear.

Laboratory tests should be conducted to quantify this relationship; i.e. to define the relationship between the rock mass modulus and the joints spacing, joints orientation, and joints aperture. In addition, the stress factor should be introduced to the test to investigate its effect on both the joints and the modulus at the same time.

3. A three dimensional finite element analysis can be applied to the problem. More precise results can be obtained if the analysis include major structural features of the rock mass at the situ.

REFERENCES

- Cox, R. M., Jr., Rock behavior during experimental room excavation in Idaho Springs. Gneiss, Ph.D. thesis, Colorado School of Mines, T-1283, 1971, 215 p.
- Chitombo, G. P., 1981, Personal communication.
- Fitzhugh, T. L., Abel, J. F., Jr., Nichols, T. C., Jr., the relation of geology to stress changes caused by underground excavation in crystalline rock at Idaho Springs, Colorado. Geological survey professional paper no. 965, 1976, 47 p.
- Gary Van Huffel, Geology of CSM Experimental mine, Miami tunnel Clear Creek County, Colorado, senior thesis, Geology, 468 p., April, 1975.
- Geokon, Inc., Field Manual for CSIRO hollow inclusion gauge, 1981, 30 p.
- Goodman, R. E., Methods of geological engineering in discontinuous rocks, West Publishing Co., St. Paul, Minn. 1976.
- Holmberg, R., Hard rock excavation at the CSM/ONWI test site using Swedish blast design techniques, ONWI report no. 2, 1981.
- Hooker, V. E., Bickel, D. L., Aggson, J. R., In situ determination of stresses in mountainous topography. Bureau of Mines RI 7654, 1972, 19 p.
- Hustrulid, W. A., The CSM cell - a borehole device for determining the modulus of rigidity of rock. The 5th U.S. rock mechanics symposium, 1972, 181-225 pp.
- Irad Gage, Inc., N. H., Installation/instruction manual model REF convergence meter, RMC multipoint C-anchor, sonic probe.
- Moench, R. H., Geology of Precambrian rocks, Idaho Springs district, Colorado: U.S. Geol. Survey Bull., 1982-A, 1964, 70 p.

- Moench, R. H. and Drake, A. A., Jr., Economic geology of the Idaho Springs district, Clear Creek and Gilpin counties, Colorado: U.S. Geol. Survey Bull., 1208 1966, 91 p.
- Obert, L., and Duval, W. I., Rock mechanics and the design of structures in rock: New York, John Wiley and Sons, Inc., 1967, 650 p.
- Panek, L. A., Effect of rock fracturing on the modulus, as determined by borehole dilation tests, Proceedings of the second congress of the International Society for Rock Mechanics, vol. 1, Beograd, 1970, pp. 383.
- Pariseau, W. G., A two dimensional finite element approach to the evaluation of underground coal mine stability, Interpretation of rock mechanics data, vol. I, prepared under contract no. H0220077, for USBM, June, 1978, 172 p.
- Rosasco, P., Graduate student in CSM Geology Department, and subcontractor CSM/ONWI test facility at CSM Experimental Mine, 1981, personal communication.
- Tadolini, S.C., and Dolinar, D. R., In situ stress determination ONWI test facility, Edgar Mine, Idaho Springs, Colorado, USBM Progress Report 10027, July, 1981.
- Wentworth, D. H., 1966, Some factors influencing strain, relief overcoring M.Sc. thesis, Colorado School of Mines, T-1097, 136 p.
- Willoughby, D. F. and Hovland, H. J., Finite element analysis of stages of excavation of Helms underground powerhouse, The 19th U.S. Rock Mechanics Symposium, 1978, pp. 159 to 00. 164.
- Worothicki, G. and R. J. Wolton, Triaxial hollow inclusion gauges for determination of rock stresses in situ. I.S.R.M. Conference, Sydney, Australia, 1976, 12 pp.

APPENDIX A

Rock Properties

A.1 Uniaxial compressive testing.

These tests had been carried out to determine the elastic constants of the rock, variation of the elastic constants with different directions and the compressive strength of the rock.

Ninety seven samples were selected to represent three orthogonal directions, two diagonal directions, and the major rock types. Some samples were tested in USBM laboratories. The samples are numbered according to the direction of the borehole relative to the axis of the room.

- (L) samples represent the rock in the longitudinal boreholes parallel to the axis of the room (S20E)
- (V) samples represent the vertical boreholes (up or down)
- (H) samples represent the horizontal boreholes and perpendicular to the room axis (N70E)
- (D) samples represent the diagonal boreholes

Samples were picked up from NX-cores having 1.865 in. in diameter. Table A.1 shows sample orientation, dimension, rock type, elastic constants, and the rock strength.

Explanation for Table A.1

GN = granite biotite gneiss

Peg = pegmatites

BGN = biotite gneiss

L/D = height to diameter ratio of the sample

E = elastic modulus of the rock x 10^6 psi

ν = Poisson's ratio

σ_c = compressive strength, psi

Sp.gr = specific gravity

Table A.1. Uniaxial Compressive Test Results

Sample No.	Rock Type	L/D	E	ν	σ_c	Sp.gr	Depth in the Borehole, ft.
H 1	GN	2.04	4.67	0.30	10,660	2.70	10
H 2	GN	2.04	7.00	0.28	11,700	2.64	5
H 3	GN	1.99	8.50	0.29	13,100	2.68	7.5
H 4	GN	2.05	12.0	0.16	16,050	2.77	6
H 5	GN	2.12	13.70	0.21	12,730	2.74	11
H 6	GN	2.00	7.50	0.25	19,600	2.73	14.5
H 7	GN	2.52	6.20	0.24	8,000	2.70	1.5
H 8	GN	2.51	9.20	0.29	13,000	2.67	2.5
H 9	GN	2.51	7.20	0.19	11,700	2.77	4.5
H10	Peg	2.48	8.10	0.26	19,000	2.59	7
H11	GN	2.54	5.40	0.18	11,560	2.71	3
H12	GN	2.51	9.30	0.17	22,850	2.68	13
H13	GN	2.49	8.90	-	22,230	2.67	17
H14	GN	2.49	8.80	0.31	21,600	2.79	21
H15	GN	2.07	7.80	0.21	14,200	2.72	24
H16	GN	2.00	11.80	0.24	13,850	2.67	24.5
H17	GN	2.09	10.30	0.21	16,860	2.72	25
H18	GN	1.99	9.20	-	17,800	2.70	26
L 1	GN	2.12	4.88	0.18	13,820	2.73	24.5
L 2	GN	2.13	7.45	0.26	17,340	2.72	32
L 3	GN	2.16	5.80	0.30	13,530	2.71	41
L 4	GN	2.09	7.50	0.16	21,000	2.66	48
L 5	GN	2.00	12.2	0.32	18,730	2.69	55
L 6	GN	2.10	6.05	0.16	18,960	2.78	63
L 7	BGN	2.22	10.4	0.28	16,120	2.79	80
L 8	BGN	2.17	9.68	0.32	17,020	2.77	82
L 9	Peg	2.11	7.13	0.28	14,120	2.54	90

(Table A.1. continued)

Sample No.	Rock Type	L/D	E	ν	σ_c	Sp.gr	Depth in Borehole,
L10	GN	2.25	11.50	0.19	19,000	2.74	47
L11	GN	2.20	10.23	0.22	27,230	2.74	11
L12	GN	2.24	11.09	0.21	20,630	2.70	61
L13	GN	2.31	10.78	0.19	21,440	2.68	71
L14	BGN	2.01	4.97	0.23	5,860	2.92	82
L15	Peg	1.91	6.97	0.32	12,500	2.58	91
L16	GN	2.33	10.19	0.21	13,200	2.63	92
L17	GN	2.11	9.24	0.17	32,760	2.71	32
L18	Peg	2.22	8.05	0.27	15,130	2.56	72
L19	GN	2.32	8.41	0.22	14,640	2.77	59
L20	Peg	2.34	7.88	0.25	16,070	2.54	97
L21	Peg	2.18	7.74	0.34	12,830	2.49	100
L22	Peg	2.18	8.2	0.28	16,030	2.52	102
L23	GN	2.28	10.8	0.22	24,040	2.73	23
L24	Peg	2.11	7.75	0.26	16,020	2.55	104
L25	Peg	2.00	7.12	0.31	14,700	2.53	103
V 1	GN	2.00	10.2	0.21	23,230	2.68	7
V 2	GN	2.01	8.22	0.35	11,000	2.69	4.5
V 3	GN	2.05	9.33	0.12	15,100	2.75	14
V 4	GN	2.06	10.22	0.21	13,870	2.71	17
V 5	GN	1.94	8.5	0.17	7,140	2.73	11
V 6	BGN	2.00	10.6	0.23	23,970	2.81	10.5
V 7	Peg	2.13	8.9	0.25	18,910	2.57	13
V 8	Peg	2.12	6.6	0.33	17,130	2.55	7.5
V 9	Peg	2.13	9.00	0.32	11,350	2.51	12
V10	GN	1.96	9.29	0.20	11,360	2.76	1
V11	GN	1.93	5.22	0.30	9,350	2.68	10

(Table A.1. continued)

Sample No.	Rock Type	L/D	E	ν	σ_c	Sp.gr	Depth in Borehole,
V12	GN	2.02	10.57	0.19	29,000	2.74	47
V13	GN	1.98	6.82	0.20	11,000	2.72	18
V14	GN	2.21	7.78	0.23	17,500	2.68	1.5
V15	Peg	2.05	8.53	0.29	14,600	2.58	7
V17	GN	2.13	11.02	0.22	21,140	2.65	15
V18	GN	1.98	10.43	0.23	22,880	2.67	7
V19	GN	1.99	8.82	0.20	17,100	2.76	10
V20	GN	2.15	8.97	0.26	13,600	2.77	11
V21	Peg	2.10	7.01	0.31	12,800	2.56	13
V22	Peg	1.96	9.30	0.28	20,520	2.52	11
V23	GN	2.25	9.12	0.19	17,100	2.73	3
V24	GN	2.08	9.61	0.18	18,060	2.74	4
V25	GN	2.09	8.89	0.25	17,230	2.65	11.5
V26	GN	2.08	5.92	0.17	8,060	2.97	6
V27	GN	2.06	8.37	0.21	15,200	2.63	17.5
V28	GN	2.10	9.96	0.19	18,690	2.67	18
D 1	GN	2.35	8.33	0.21	20,650	2.72	11
D 2	GN	2.33	10.95	0.20	18,760	2.67	12
D 3	GN	2.06	10.65	0.18	12,800	2.72	9
D 4	GN	2.34	8.58	0.23	21,600	2.68	5.5
D 5	GN	2.24	9.20	0.19	29,100	2.73	7
D 6	GN	1.98	10.71	0.20	32,260	2.72	14.5
D 7	GN	2.61	13.04	0.18	23,600	2.72	4
D 8	GN	2.33	7.32	0.20	9,160	2.68	9
D 9	GN	2.15	9.38	0.21	12,500	2.66	4
D10	Peg	2.08	7.76	0.30	13,100	2.56	15
D11	GN	2.23	8.18	0.15	11,350	2.66	14

(Table A.1. continued)

Sample No.	Rock Type	L/D	E	ν	σ_c	Sp.gr	Depth in the Borehole, ft.
D12	GN	2.07	9.7	0.27	16,300	2.78	11
D13	GN	2.06	9.6	0.21	19,600	2.71	8
D14	GN	2.31	8.30	0.26	12,300	2.72	8
D15	Peg	2.10	9.34	0.26	18,000	2.63	3
D16	GN	2.07	8.56	0.22	16,300	2.71	13
D17	GN	2.06	9.08	0.22	14,660	2.72	6
D18	GN	2.10	6.76	0.21	11,200	2.76	7
D19	GN	2.09	8.84	0.20	21,000	2.72	8
D20	Peg	2.11	7.9	0.19	13,750	2.56	2
D21	GN	2.07	10.34	0.21	23,530	2.67	15
D22	GN	2.09	6.04	0.25	10,260	2.80	1
D23	GN	2.05	8.4	0.19	17,000	2.73	5
D24	GN	2.12	9.80	0.23	18,700	2.70	11
D25	GN	2.17	10.2	0.18	14,800	2.73	7
D26	GN	2.16	8.11	0.24	16,600	2.68	9

Total of 97 samples.

Table A.2 shows the averaged elastic values for the major rock types, and the rock strength.

Table A.2. Summary of Uniaxial Compressive Testing Results.

Rock Type: Granite Biotite Gneiss				
Sample Direction	Ex10 ⁶ psi	ν	σ_c ,psi	Sp.gr
Longitudinal (L)	8.98	0.214	19,790	2.714
Vertical (v)	8.88	0.216	15,590	2.710
Horizontal (H)	8.61	0.240	15,150	2.709
Diagonal (D)	9.13	0.210	17,130	2.712
Average	8.9	0.22	16,910	2.711
St. Dev.	0.19	0.012	1,815	0.002
Pegmatites				
Average	7.96	0.285	15,360	2.55
St. Dev.	0.79	0.036	2,490	0.032

A.2 Biaxial Compressive Testing.

Biaxial compressive tests were conducted of all sound pieces of the cores produced by overcoring processes from the tested holes. The testing device is a biaxial chamber of 8 inches length and 6 inches in diameter. The device is shown in Figure A.1. Maximum pressure of 1,000 psi was used to test the cores containing the CSIRO gages, and a constant pressure of 600 psi was applied to test the cores with USBM borehole gage.

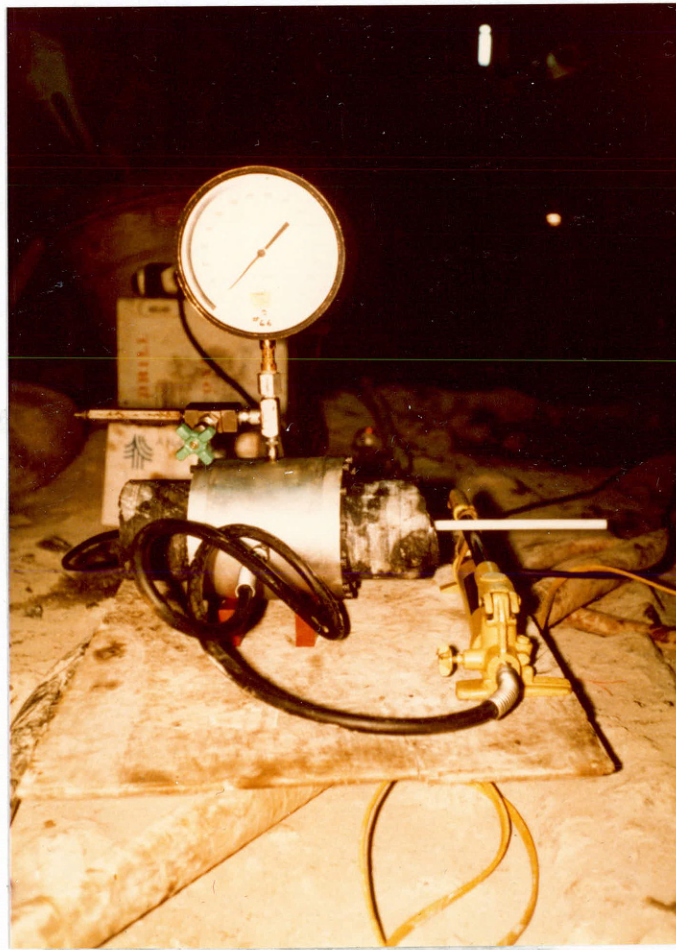


Figure A.1 Biaxial compression chamber.

Biaxial compressive testing on the cores containing CSIRO gages produce three elastic constants and two Poisson's ratios. The strain versus the applied pressure equations were found using the least square method. The results of tests produced by using the USBM borehole gage were analyzed by Tadolini of the USBM.

Table A.3 gives the results of biaxial compressive testing. The following expressions are used:

E_2 = Elastic modulus using ϵ_2 (CSIRO gage)

E_6 = Elastic modulus using ϵ_6 (CSIRO gage)

E_8 = Elastic modulus using ϵ_8 (CSIRO gage)

ϵ_2 , ϵ_6 & ϵ_8 strain recorded by circumferential strain gages

ν_{12} = Poisson's ratio using ϵ_1 and ϵ_2

ν_{78} = Poisson's ratio using ϵ_7 and ϵ_8

E_1 and E_7 axial strain

\bar{E} = average elastic modulus

E_{\max} = maximum elastic modulus using USBM gage

E_{\min} = minimum elastic modulus using USBM gage

Table A.3 Biaxial Test Results

Hole 1					
Test No.	Depth (ft.)	Elastic Constant $\times 10^6$ (psi)	\bar{E}	Poisson's Ratio	Gage Used
H1	12	$E_2 = 8.7$ $E_6 = 7.9$ $E_8 = 8.5$	8.4	$\nu_{12}=0.35$ $\nu_{78}=0.27$	CSIRO
Hole 2					
T1	1	$E_2 = 13.6$ $E_6 = 9.2$ $E_8 = 12.1$	11.6	$\nu_{12}=0.52$ $\nu_{78}=0.66$	CSIRO
T2	4.5	$E_2 = 7.0$ $E_6 = 5.7$ $E_8 = 2.75$	5.15	$\nu_{12}=0.32$ $\nu_{78}=0.17$	CSIRO
T3	7.5	$E_2 = 8.9$ $E_6 = 7.9$ $E_8 = 8.2$	8.33	$\nu_{12}=0.42$ $\nu_{78}=0.45$	CSIRO
T4	15	$E_2 = 9.4$ $E_6 = 8.4$ $E_8 = 11.5$	9.7	$\nu_{12}=0.42$ $\nu_{78} = -$	CSIRO
TA	3	$E_{\max} = 8.9$ $E_{\min} = 8.99$	8.44		USBM
TB	13	$E_{\max} = 11.0$ $E_{\min} = 9.4$	10.2		USBM
TC	17	$E_{\max} = 9.8$ $E_{\min} = 8.76$	9.23		USBM
TD	21	$E_{\max} = 10.1$ $E_{\min} = 8.18$	9.14		USBM

TA, TB, TC and TD six inches overcores collected from hole 2 to be tested elastic modulus determination. They do not belong to positions where stresses have been measured.

Table A.3 (continued)

Hole 3					
Test No.	Depth (ft.)	Elastic Constant $\times 10^6$ (psi)	\bar{E}	Poisson's Ratio	Gage Used
R 3	2.8	$E_{\max} = 8.01$ $E_{\min} = 6.87$	7.44		USBM
R 5	4.8	$E_{\max} = 10.23$ $E_{\min} = 6.3$	8.26		USBM
R 6	8.75	$E_{\max} = 6.46$ $E_{\min} = 6.00$	6.23		USBM
R10	12.8	$E_{\max} = 7.80$ $E_{\min} = 2.73$	5.22		USBM
P 2	14.3	$E_2 = 9.51$ $E_6 = 10.905$ $E_8 = 10.22$	10.21	$\nu_{12} = 0.237$ $\nu_{78} = 0.282$	CSIRO
R12	17.4	$E_{\max} = 8.94$ $E_{\min} = 7.2$	8.07		USBM
R13	18.4	$E_{\max} = 8.26$ $E_{\min} = 5.14$	6.7		USBM
P 3	19.5	$E_2 = 11.34$ $E_3 = 9.69$ $E_4 = 9.91$	10.3	$\nu_{12} = .38$ $\nu_{78} = .42$	CSIRO
R15	23.0	$E_{\max} = 10.0$ $E_{\min} = 8.10$	9.05		USBM

(continued)

Table A.3 (continued)

Hole 3					
Test No.	Depth (ft.)	Elastic Constant $\times 10^6$ (psi)	\bar{E}	Poisson's Ratio	Gage Used
R16	27.8	$E_{\max} = 11.85$ $E_{\min} = 8.94$	10.39		USBM
R17	27.8	$E_{\max} = 10.86$ $E_{\min} = 8.07$	9.47		USBM
P 5	30	$E_2 = 15.06$ $E_6 = 12.75$ $E_8 = 13.6$	13.8	$\nu_{12} = .28$ $\nu_{78} = .16$	CSIRO

A.3 Triaxial Compressive Tests.

These tests were conducted over five groups of samples taken from the overcores. Each group represents the same piece of the overcore. The relationship between the failure strength of the rock and the confining stress is shown in Figure A.1. The results of tests are given in Table A.4.

Table A.4 Triaxial Test Results

Confining Stress (psi)	Failure Strength (psi)					Average Group
	Group 1	Group 2	Group 3	Group 4	Group 5	
0	10950	11000	9750	15840	11670	11840
500	14350	19850	14400	21540	16730	17370
1000	15000	22800	19650	24300	21000	20550
1500	17500	27800	24790	26360	25740	24440

The results suggest the following:

- a. Failure strength (psi) = 12997 + 7.89 confining stress (psi), i.e. $\sigma_1 = 12997 + 7.89 \sigma_3$
- b. The shear strength = 2314.0 psi
- c. Angle of internal friction (ϕ) = 50.8°.

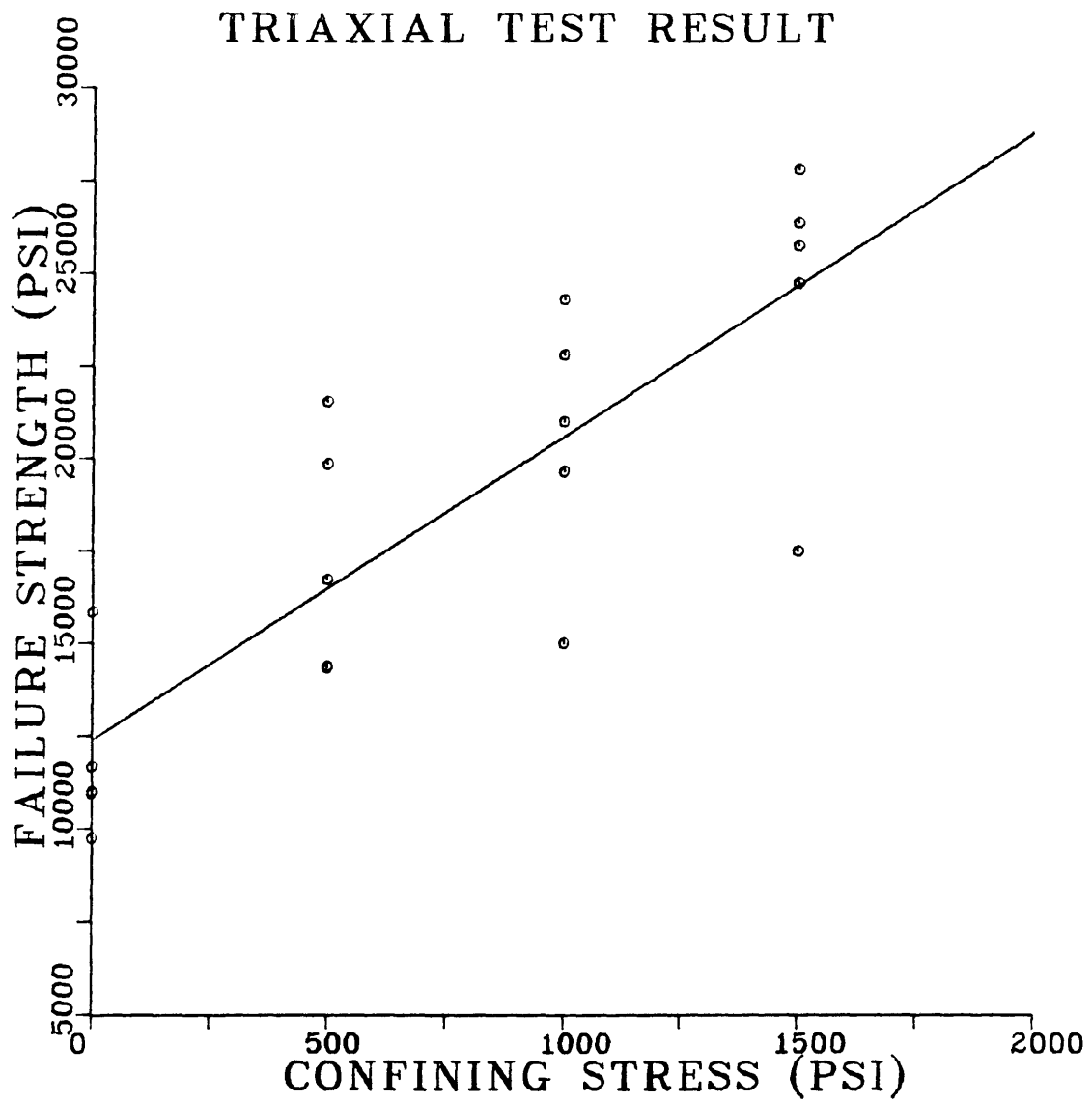


Figure A.1 Triaxial Test Results.

A.4 Brazilian Test.

Indirect tension tests were conducted on ten NX-cores samples. The parameters of the samples and the results are given in Table A.5. (All samples have a diameter of 1.864 in.)

Table A.5 Brazilian Test Results

Sample	Thickness (in.)	Failure Load (lb)	Tensile Strength (psi) σ_T
1	0.725	6,500	3,390
2	0.980	9,500	3,660
5	1.150	5,000	1,640
4	1.000	6,330	2,160
5	0.926	6,700	2,470
6	1.250	7,060	1,930
7	0.844	5,850	2,370
8	0.875	6,060	2,370
9	1.250	9,815	2,680
10	1.156	7,100	2,100
Average tensile strength: 2,476 psi \pm 595			

The tensile strength was calculated using the equation:

$$\sigma_T = \frac{2P}{\pi t D}$$

where: P = failure load (lb)

t = sample thickness, in.

D = sample diameter, in.

APPENDIX B

In Situ Stress

B.1 CSIRO Data Reduction Program. (source, Terratic, 1980)

```

140 PRINT "THIS PROGRAM COMPUTES THE PRINCIPAL STRESSES AND      "
150 PRINT "THEIR DIRECTION COSINES FROM ANY NUMBER OF BOREHOLE  "
160 PRINT "STRAINS MEASURED WITH THE CSIRO STRESS CELL.  THE    "
170 PRINT "PROPER CORRECTION FACTORS K1,K2,K3,ANDK4 SHOULD BE   "
180 PRINT "INPUT AS A DATA STATEMENT"
190 PRINT "INPUT NUMBER OF STRAIN READINGS TO BE AVERAGED"
200 INPUT D1
210 DIM K(4),E(D1),C(D1),A(D1)
220 DIM F(D1,6),U(D1,1)
230 PRINT "INPUT ELASTIC MODULUS (IN MPA) AND POISSON'S RATIO"
240 INPUT B6,B7
250 PAGE
260 PRINT "INPUT ";D1;" STRAIN READINGS AND THEIR ORIENTATION"
270 PRINT "ANGLES THETA AND PHI."
280 PRINT
290 PRINT "NOTE:POSITIVE Z-AXIS IS VERTICAL DOWNWARD"
300 PRINT "      POSITIVE X-AXIS IS DUE NORTH"
310 PRINT "      POSITIVE Y-AXIS IS DUE EAST"
320 PRINT "THETA IS THE ANGLE WHICH DEFINES THE CIRCUMFERENTIAL"
330 PRINT "ORIENTATION OF THE OBSERVED STRAIN; IT IS MEASURED AS"
340 PRINT "THE POSITIVE ANGLE IN THE CLOCKWISE DIRECTION (WHEN"
350 PRINT "VIEWED IN THE POSITIVE Z DIRECTION) FROM THE POSITIVE"
360 PRINT "X-AXIS IN THE X-Y PLANE.  PHI IS THE ANGLE WHICH      "
370 PRINT "DEFINES THE AXIAL ORIENTATION OF THE OBSERVED STRAIN;"
380 PRINT "IT IS MEASURED AS THE (+) ANGLE FROM THE (+) Z"
390 PRINT "DIRECTION TO THE VECTOR WHICH IS TANGENT TO THE      "
400 PRINT "BOREHOLE AND PJINTS IN THE DIRECTION OF CLOCKWISE      "
410 PRINT "ROTATION.  THE PROGRAM ASSUMES THAT PHI IS 0,45,90,OR  "
415 PRINT "135 DEGREES.  "
420 FOR N=1 TO D1
430 INPUT E(N),C(N),A(N)
440 NEXT N
450 PAGE
460 FOR N=1 TO 4
470 READ K(N)
480 NEXT N
490 FOR N=1 TO D1
500 REMARK PERFORM MULTIPLE LINEAR REGRESSION TO DETERMINE THE
510 REMARK STRESSES FROM STRAINS AND THEIR STATISTICAL VARIATION.
520 B1=COS(2*C(N))
530 B2=COS(2*A(N))
540 B3=SIN(2*C(N))
550 B4=SIN(2*A(N))
560 B5=B7^2
570 F(N,1)=(B5-1)*B1*(1-B2)*K(2)+0.5*(K(1)-B7)-0.5*(K(1)+B7)*B2
580 F(N,2)=(1-B5)*B1*(1-B2)*K(2)+0.5*(K(1)-B7)-0.5*(K(1)+B7)*B2

```



```

590 F(N,3)=0.5*(1-K(4)*B7)+0.5*(1+K(4)*B7)*B2
600 F(N,4)=2*(B5-1)*B3*(1-B2)*K(2)
610 F(N,5)=2*(1+B7)*COS(C(N))*B4*K(3)
620 F(N,6)=-2*(1+B7)*SIN(C(N))*B4*K(3)
630 U(N,1)=E(N)*B6
640 NEXT N
650 DIM G(6,D1),H1(6,6),I(6,6),J(6,1),L(1,D1),M(1,1),O(1,6)
660 DIM S(6,1),V(6,6),R(1,1)
670 G=TRN(F)
680 H1=G MPY F
690 I=INV(H1)
700 J=G MPY U
710 S=I MPY J
720 L=TRN(U)
730 M=L MPY U
740 R=INV(M)
750 B6=DET
760 O=TRN(S)
770 L=O MPY G
780 M=L MPY U
790 R=INV(M)
800 B9=DET
810 D9=(B8-B9)/(D1-6)
820 V=I*D9
830 REMARK DETERMINE PRINCIPAL STRESSES AND THEIR DIRECTIONAL
840 REMARK COSINES FROM THE PREVIOUSLY DETERMINED STRESSES.
850 DIM T(3,3),P(3,3)
860 T(1,1)=S(1,1)
870 T(2,1)=S(4,1)
880 T(3,1)=S(6,1)
890 T(1,2)=S(4,1)
900 T(2,2)=S(2,1)
910 T(3,2)=S(5,1)
920 T(1,3)=S(6,1)
930 T(2,3)=S(5,1)
940 T(3,3)=S(3,1)
950 D3=T(1,1)+T(2,2)+T(3,3)
960 D4=T(1,1)*T(3,3)+T(2,2)*T(3,3)+T(1,1)*T(2,2)
970 D5=T(2,3)^2+T(1,2)^2+T(1,3)^2
980 D4=D4-D5
990 P=INV(T)
1000 D5=DET
1010 D8=0
1020 PRINT "THE PRINCIPAL STRESSES WILL NOW BE DETERMINED BY      "
1030 PRINT "SOLVING THE CUBIC EQUATION WHOSE REAL ROOTS ARE THE    "
1040 PRINT "PRINCIPAL STRESSES USING THE NEWTON-RAPHSON ITERATION."
1050 N=1
1060 DIM Z(3)
1070 PRINT "INPUT TRIAL STRESS VALUE."
1080 INPUT D2
1090 DEF FNS(D2)=D2^3-D3*D2^2+D4*D2-D5

```

```
1100 DEF FND(D2)=3*D2^2-2*D3*D2+D4
1110 D7=FNS(D2)
1120 IF D7>1.0E-6 THEN 1150
1130 IF D7<-1.0E-6 THEN 1150
1140 GO TO 1170
1150 D2=D2-FNS(D2)/FND(D2)
1160 GO TO 1110
1170 PRINT "YOU HAVE FOUND ONE OF THE THREE SOLUTIONS, NAMELY:";D2
1180 PRI " ";D8;" SEPERATE SOLUTIONS HAVE BEEN DETERMINED AND REC."
1190 PRINT "DO YOU WISH TO SAVE THIS VALUE ALSO? Y=1, N=0"
1200 INPUT B1
1210 IF B1<>1 THEN 1250
1220 D8=D8+1
1230 Z(N)=D2
1240 N=1+N
1250 PRINT "DO YOU WISH TO FIND ANOTHER SOLUTION? Y=1, N=0"
1260 INPUT B1
1270 PAGE
1280 IF B1=1 THEN 1070
1290 IF Z(1)>Z(2) THEN 1360
1300 IF Z(1)>Z(3) THEN 1460
1310 IF Z(2)>Z(3) THEN 1500
1320 B1=Z(3)
1330 B2=Z(2)
1340 B3=Z(1)
1350 GO TO 1530
1360 IF Z(1)>Z(3) THEN 1410
1370 B1=Z(3)
1380 B2=Z(1)
1390 B3=Z(2)
1400 GO TO 1530
1410 IF Z(2)>Z(3) THEN 1560
1420 B1=Z(1)
1430 B2=Z(3)
1440 B3=Z(2)
1450 GO TO 1530
1460 B1=Z(2)
1470 B2=Z(1)
1480 B3=Z(3)
1490 GO TO 1530
1500 B1=Z(2)
1510 B2=Z(3)
1520 B3=Z(1)
1530 Z(1)=B1
1540 Z(2)=B2
1550 Z(3)=B3
1560 DIM W(3),X(3),Y(3),H2(3,3),H3(3,3),H4(3,3)
1570 FOR N=1 TO 3
1580 CALL "IDN",H2
1590 LET H3=H2*Z(N)
1600 LET H3=T-H3
```

```

1610 FOR D2=1 TO 3
1620 FOR D3=1 TO 3
1630 LET H4=H3
1640 FOR D4=1 TO 3
1650 H4(D4,D3)=0
1660 H4(D2,D4)=0
1670 NEXT D4
1680 H4(D2,D3)=1
1690 H4=INV(H4)
1700 H2(D2,D3)=DET
1710 NEXT D3
1720 NEXT D2
1730 H2=TRN(H2)
1740 D5=1
1750 B1=SQR(H2(1,D5)^2+H2(2,D5)^2+H2(3,D5)^2)
1760 IF B1>0.01 THEN 1820
1770 D5=D5+1
1780 IF D5=4 THEN 1800
1790 GO TO 1750
1800 D5=1
1810 B1=1000
1820 W(N)=H2(1,D5)/B1
1830 X(N)=H2(2,D5)/B1
1840 Y(N)=H2(3,D5)/B1
1850 NEXT N
1860 PAGE
1870 REMARK DATA OUTPUT
1880 PRINT "MEASURED STRAINS, THETA, PHI"
1890 PRINT
1900 FOR N=1 TO D1
1910 PRINT USING "+1D.6D,3X,+3D,3X,+3D":E(N),C(N),A(N)
1920 NEXT N
1930 PRINT
1940 PRINT "MODULUS=";B6;" MPA POISSON`S RATIO=";B7
1950 PRINT
1960 PRINT "DETERMINED STRESSES (MPA)"
1970 PRINT
1980 DIM Q(6)
1990 FOR N=1 TO 6
2000 Q(N)=SQR(V(N,N))
2010 NEXT N
2020 PRINT USING 2030:"Sx","SD","Sy","SD","Sz","SD"
2030 IMAGE 6 (3X,3A,4X)
2040 PRINT USING 2050:S(1,1),Q(1),S(2,1),Q(2),S(3,1),Q(3)
2050 IMAGE 3(+4D.2D,2X,3D.2D,4X)
2060 PRINT USING 2030:"Txy","SD","Tyz","SD","Txz","SD"
2070 PRINT USING 2050:S(4,1),Q(4),S(5,1),Q(5),S(6,1),Q(6)
2080 PRINT
2090 PRINT "PRINCIPAL STRESSES (MPA), DIRECTION COSINES"
2100 PRINT
2110 PRINT USING 2120:"SIGMA","L","M","N"

```

```
2120 IMAGE(2X,5A,9X,1A,9X,1A,9X,1A)
2130 FOR N=1 TO 3
2140 PRINT USING 2150:Z(N),W(N),X(N),Y(N)
2150 IMAGE 4(+4D.2D,2X)
2160 NEXT N
2170 END
2180 DATA 1.12,1.13,1.08,0.91
```

B.2 Stresses Due to Topography. (Hooker, 1972)

A vertical section of 2,000 ft. width was analyzed for the gravitational stresses due to topographic highs. Hooker's approach was used in this analysis. The section has a bearing of S23E and is extended on both sides of the room. The section has been divided into six layers of 40 ft. thicknesses. The configuration of this section is shown in Figure B.1. The normal stresses σ_x , σ_y and the shear stress τ_{xy} at the site, due to subsequent layers are given by the following equations:

$$\sigma_x = - \frac{\gamma h}{\pi} (\theta_2 - \theta_1 + \sin (\theta_2 - \theta_1) \cos (\theta_2 + \theta_1))$$

$$\sigma_y = - \frac{\gamma h}{\pi} (\theta_2 - \theta_1 - \sin (\theta_2 - \theta_1) \cos (\theta_2 + \theta_1))$$

$$\tau_{xy} = - \frac{\gamma h}{\pi} (\sin \theta_2 + \theta_1) \sin (\theta_2 - \theta_1)$$

γ = the weight density of the rock = 168 lb/ft³

h = the thickness of the layer

θ_1 and θ_2 are defined as shown in Figure B.1

The overburden depth above the test site is 275 ft. and it is also the average overburden depth between the two ends of the room,

$$\frac{295 + 255}{2} = 275 \text{ ft.}$$

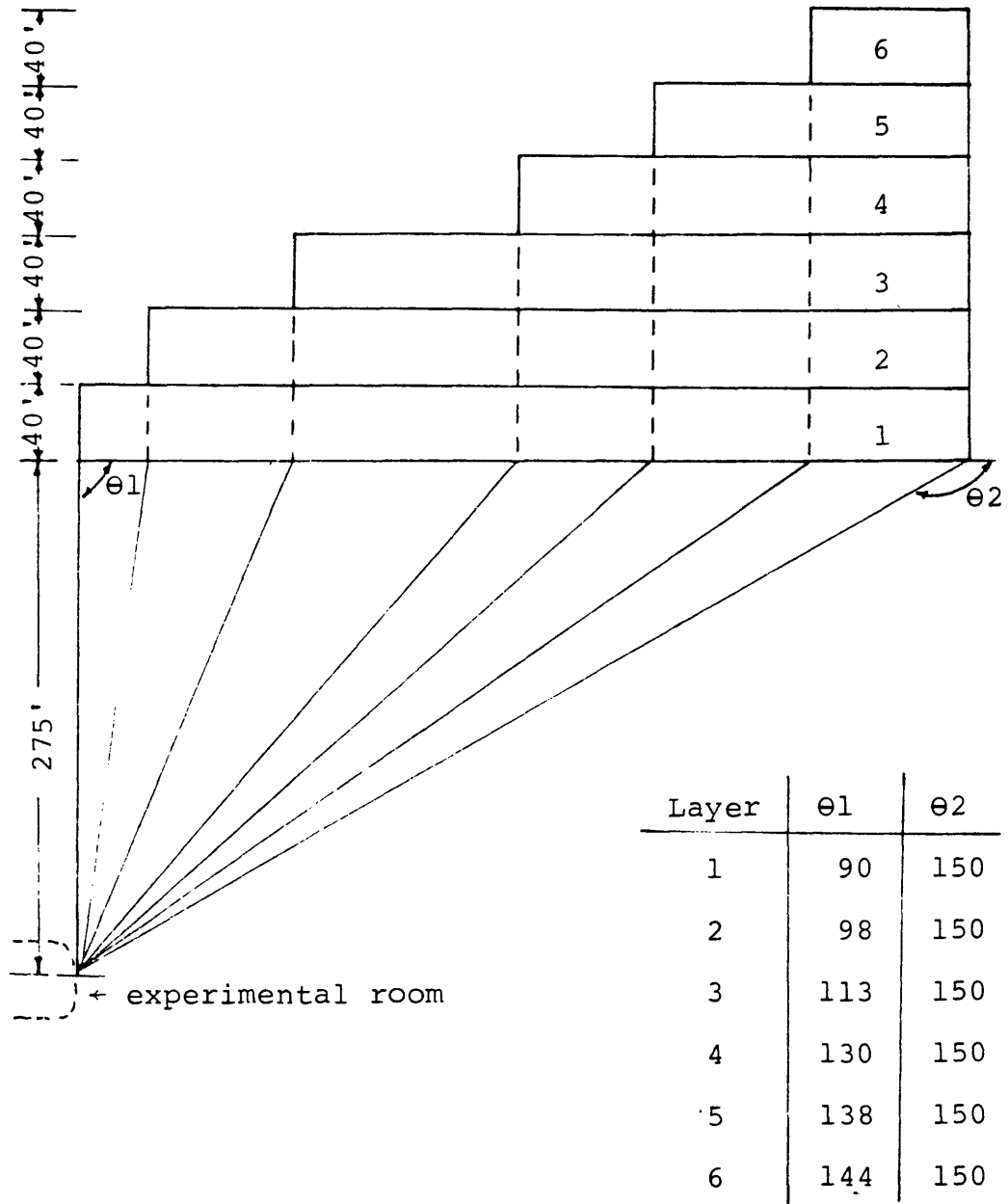


Figure B.1 Configuration of distributed load of mountainous topograph.

Table B.1 gives the influence of topography on stresses components.

Table B.1 Stresses Due to Topography
(stresses in psi, (+) stress is compressive)

Layer	Stresses (psi)		
	σ_x	σ_y	τ_{xy}
1	22.3	9.9	-11.6
2	18.1	9.9	-11.3
3	10.1	9.1	- 8.9
4	3.4	5.9	- 4.4
5	1.9	4.3	- 2.9
6	0.5	1.5	- 0.9
Total	56.4	40.6	-39.9

The vertical influence and Poisson's effect due to topography in horizontal plane yields:

$$\sigma_x \text{ total} = 275 \left(\frac{168}{144} \right) + 40.6 = 361.4 \text{ psi}$$

$$\sigma_y \text{ total} = \left(\frac{0.22}{1-0.22} \right) (361.4) \left(\frac{168}{144} \right) + (56.4) = 175.3 \text{ psi}$$

$$\tau_{xy} = 39.9 \text{ psi}$$

B.3 USBM Borehole Gage Deformation Measurements.

12 Deformation Measurements

Least Squares Plane Strain Solution

<u>Set</u>	<u>Deformation (Micro in.)</u>	<u>Angle of Measure</u>	<u>Elastic Modulus</u>
1	-181	90.	7.E06
2	-119	150.	7.E06
3	-438	30.	7.E06
4	-110	90.	6.7E06
5	- 31	150.	6.7E06
6	-401	30.	6.7E06
7	- 46	90.	6.7E06
8	- 94	150.	6.7E06
9	-220	30.	6.7E06
10	- 58	90.	9.0E06
11	- 84	150.	9.0E06
12	-252	30.	9.0E06

Poisson's ratio = 0.2

Stress components with respect to X, Y

Coordinate system

Sigma X = 496. Sigma Y = 320 TAU XY = -179

Secondary principal stresses (psi)

P = 208. Q = 607 THETA = 32

Precision of data -

Deformation sum of squares

Residual sum of squares = 4.5339 E-8

Multiple correlation coefficient squared = 0.916948

Standard deviation of the fitted data = 7.0976 E-5

Standard error of stress components

SE(X) = 61. (psi) SE(Y) = 61. psi SE(XY) = 36. psi

C11 = 7.390116 E+11

C22 = 7.390116E + 11

C12 = 2.599225E + 11

Standard error of angle

SE(θ) = 5. Deg.

B.4 CSIRO Strain Measurements for Stress Calculations

12 CSIRO Positions
(strain $\times 10^{-6}$ μ in/in)

Strain Gage	Test No.					
	H1	T1	T2	T3	T4	T5
1	52	-80	40	60	48	51
2	257	350	187	135	89	75
3	232	276	79	93	89	-
4	58	-	73	80	61	71
5	231	186	79	-	74	-
6	246	228	54	128	133	170
7	-	-80	40	-	48	51
8	278	150	-	191	-	78
9	112	-	-	63	93	87
Strain Gage	T6	P1	P2	P3	P4	P5
1	42	14	-	66	-	20
2	150	160	155	30	110	158
3	40	63	114	112	35	113
4	135	126	66	-	70	186
5	135	-	66	127	35	157
6	146	160	155	30	107	260
7	42	40	24	52	25	90
8	160	74	160	44	135	158
9	66	42	74	36	70	44

The overcoring strain readings are given in Tables B.2 to B.13.

Table B.2 Overcoring Strain Reading

Test No. H1

Depth 12 ft.

C/L position 8 inches

Reading	Gauge output (microstrain)								
	1	2	3	4	5	6	7	8	9
Initial	2000	2000	2000	2000	2000	2000	2000	2000	2000
5 min. water	1996	1982	2002	1967	1980	1984	1997	1981	2000
10 min. water	1998	1982	1992	1980	1989	1984	1996	1997	1997
0 in.	1996	1985	1992	1972	1982	1986	2000	1977	2001
1 in.	2000	2986	1987	1966	1983	1983	2000	1982	2004
2 in.	1993	1984	1989	1976	1982	1986	2002	1978	2000
3 in.	1994	1980	1988	1974	1980	1982	2000	1975	2000
4 in.	1996	1976	1992	1970	1979	1981	2004	1968	1991
5 in.	2006	1965	1995	1974	1988	1972	2018	1951	1986
6 in.	2037	1952	2024	1980	2026	1968	2044	1939	1991
7 in.	2089	1949	2084	1996	2113	1991	2087	1953	2030
8 in.	2098	2009	2185	2006	2225	2110	2045	2073	2088
9 in.	2000	2196	2255	1973	2246	2197	1978	2205	2114
10 in.	1962	2292	2282	1991	2235	2228	1955	2277	2106
11 in.	1990	2292	2290	2022	2220	2202	1968	2282	2099
12 in.	2017	2268	2280	2034	2214	2190	1974	2263	2092
13 in.	2038	2253	2260	2039	2209	2189	1978	2252	2089
14 in.	2050	2244	2239	2033	2209	2197	1985	2240	2092
15 in.	2050	2238	2224	2038	2212	2214	1993	2250	2101
16 in.	2050	2242	2222	2041	2220	-230	2000	2255	2109
17 in.	2049	2235	2205	2040	2221	2238	2004	2251	2116
18 in.	2047	2234	2198	2040	2221	2256	2006	2260	2122
19 in.	2055	2255	2202	2060	2238	2285	2019	2279	2142
20 in.	2055	2255	2202	2060	2238	2285	2019	2279	2142

Table B.3
OVERCORING STRAIN READING

Test No. 1

C/L position 13 inches

Reading	Gauge Output (Microstrain)								
	1	2	3	4	5	6	7	8	9
Initial	0	0	0	0	0	0	0	0	0
5 min. water	- 10	- 6	- 9	- 7	- 7	- 11	- 8	- 8	-14
10 min. water	- 10	- 7	- 8	- 7	- 13	- 11	-10	- 8	-13
1 inch	- 10	- 9	- 12	-10	- 13	- 11	-15	- 18	-14
2 "	- 12	- 11	- 15	-12	- 13	- 13	-20	- 23	-18
3 "	- 15	- 12	- 12	-16	- 14	-18	- 20	- 30	-20
4 "	- 12	- 13	- 11	-18	- 16	- 17	- 17	- 31	-22
5 "	- 20	- 14	- 10	-29	- 22	- 16	- 32	- 32	-25
6 "	- 23	- 12	- 12	-18	- 23	- 18	- 32	- 34	-27
7 "	- 26	- 11	- 11	-12	- 25	- 20	- 33	- 40	-29
8 "	- 22	- 11	- 11	-16	- 25	- 23	- 34	- 42	-32
9 "	- 28	- 13	- 13	-20	- 19	- 27	- 33	- 44	-40
10 "	- 29	- 16	- 13	-24	- 13	- 34	- 24	- 59	-50
11 "	- 28	- 33	+ 23	-22	+ 30	- 30	- 30	- 50	-52
12 "	- 29	- 16	+ 58	-30	+ 35	+115	- 35	+ 35	-66
13 "	- 32	+ 20	+100	- 40	+ 45	+220	-120	+125	-60
14 "	-125	+260	+218	- 40	+160	+226	- 92	+162	-73
15 "	-100	+340	+264	- 20	+168	+215	- 88	+140	-68
16 "	- 87	+338	+266	- 22	+170	+216	- 92	+140	-72
17 "	- 87	+340	+266	- 26	+172	+215	- 88	+138	-72
18 "	- 86	+336	+266	- 22	+170	+216	- 90	+138	-74
19 "	87	+335	+266	- 26	+174	+218	- 92	+138	-74
20 "	- 90	+336	+266	- 26	+172	+218	- 90	+135	-76

Table B.4

OVERCORING STRAIN READING

Test No. 2 - 4.5 ft.

C/L position 10 inches

Reading	Gauge Output (Microstrain)								
	1	2	3	4	5	6	7	8	9
Initial	0	0	0	+900	+600	595	0	0	0
5 min. water	0	0	0	900	598	594	0	0	0
10 min. water	-14	- 31	+ 23	889	587	588	-12	+26	-21
2 inch	-18	- 47	+ 20	883	582	572	-28	+41	-45
3 "	-24	- 38	+ 12	892	584	577	-19	+18	-30
5 "	-20	- 28	+ 15	896	583	578	-18	- 8	-25
6 "	-24	- 50	18	887	586	570	+12	-14	-37
7 "	-25	- 46	19	885	596	570	18	-17	32
9 "	-26	- 44	32	916	640	583	28	-24	40
10 "	-25	- 24	48	920	650	599	30	-37	50
11 "	-23	+ 3	62	929	671	613	33	-53	62
12 "	-50	+120	80	930	672	632	30	-62	70
13 "	-60	+156	92	398	674	645	32	-70	78
14 "	-50	+150	101	943	676	638	33	-74	77
15 "	-54	+157	102	952	670	636	32	-90	65
16 "	-54	+159	100	956	665	634	36	-94	65
17 "	-53	155	93	950	664	638	40	-91	68
18 "	-52	153	103	949	662	634	36	-87	77
19 "	-52	146	100	952	663	637	36	-85	78
20 "	-52	143	93	950	666	636	36	-81	78
21 "	-50	144	94	953	664	634	38	-84	76
22 "	-52	+148	103	953	666	+650	+50	-84	-80

Table B. 5

OVERCORING STRAIN READING

Test No. 3 - 7.5 ft.

C/L position 9 inches

Reading	Gauge Output (Microstrain)								
	1	2	3	4	5	6	7	8	9
Initial	0	915	170	400	0	200	0	875	200
5 min. water	0	921	188	390	8	213	0	906	206
10 min. water	0	909	182	400	6	224	0	896	215
1.5 inches	18	895	186	400	0	211	1	939	213
3 "	25	903	206	391	1	214	0	942	206
4 "	30	900	200	392	0	198	0	935	212
6 "	45	908	207	395	17	195	0	941	215
7 "	45	910	207	398	0	198	0	943	221
8.5 "	65	912	228	438	35	225	20	983	233
10 "	30	1022	248	500	23	278	-30	1048	240
11.5 "	25	1066	250	499	8	392	- 1	1098	280
13 "	34	1053	260	495	15	369	- 1	1081	279
14.5 "	43	1044	275	488	0	352	0	1091	278
16 "	48	1042	283	485	1	342	- 6	1086	303
17 "	52	1030	275	480	0	378	0	1078	278
18.5 "	55	1044	290	480	0	369	0	1096	300
20 "	60	1042	276	426	0	342	0	1106	282
21.5 "	60	1046	284	480	0	336	0	1104	291
23 "	60	1044	272	504	16	344	73	1098	300

Table B.6

OVERCORING STRAIN READING

Test No. 4 - 15 ft.

C/L position 10 inches

Reading	Gauge Output (Microstrain)								
	1	2	3	4	5	6	7	8	9
Initial	0	0	0	0	0	0	0	0	0
5 min. water	+ 4	- 8	-11	-14	- 16	- 12	-13	+ 17	- 13
10 min. water	0	- 11	-11	-14	- 16	- 13	-13	+ 16	- 13
0 inches	- 7	- 6	-12	-13	- 16	- 8	-12	+ 9	- 9
1.5 "	- 5	- 6	-13	-10	- 19	- 10	-12	+ 8	- 8
2.5 "	- 6	- 10	-12	- 4	- 10	- 12	-10	+ 8	- 8
4 "	-10	- 12	-10	- 6	+ 20	- 14	- 3	+ 3	- 4
5 "	+10	- 16	- 9	+ 6	+ 30	- 12	+20	+ 27	+ 27
6 "	+12	- 12	+20	+14	+ 46	+ 12	+24	+ 77	+ 46
7.5 "	+15	+ 20	+50	+23	+ 50	+ 60	+33	+107	+ 66
8 "	+23	+ 78	+70	+29	+ 62	+ 99	+44	+146	+ 75
11 "	+33	+124	+75	+36	+ 55	+118	+39	+184	79
12.5 "	+43	+114	+76	+46	+ 52	109	+39	+183	82
14 "	+45	+102	+74	+45	+ 58	104	+38	+186	84
15 "	+54	+ 92	+69	+46	+ 58	100	+43	+184	85
16 "	+61	+ 84	+75	+44	+ 54	119	+44	+186	84
17.5 "	+55	+ 78	+78	+47	+ 81	120	+43	+188	87
19 "	+57	+ 77	+66	+48	+ 95	129	+56	+203	93
20 "	+52	+ 76	+70	+61	+ 97	131	+64	+206	103
21 "	+55	+ 84	+85	+70	+102	132	+71	+195	116
22.5 "	+60	+ 87	+91	+72	+103	132	+77	187	127
24 "	+60	+104	+89	+72	+100	134	+79	203	131

Table B.7
Overcoring Strain Reading
 Test No. 5 - 20 ft.
 C/L position 11 inches

Reading	Gauge output (microstrain)								
	1	2	3	4	5	6	7	8	9
Initial	0	1000	500	0	0	1000	0	500	0
5 min. water	-14	979	481	-19	- 19	983	+13	484	-12
10 min. water	-18	971	478	-19	- 29	982	+ 7	488	-13
1.5	-15	980	476	-13	- 21	980	-20	480	-14
3	-23	970	471	-14	- 23	956	-15	428	-18
4	-17	976	476	-20	- 18	966	-12	423	-19
5.5	-20	981	480	-13	- 15	971	-14	480	-18
7	-17	988	484	-14	- 13	978	-13	482	-15
8.5	-14	980	482	-15	- 11	980	-10	485	-13
10	-13	983	483	-17	- 7	984	- 8	488	-18
11.5	+50	1012	+517	-18	+ 42	1008	+43	+570	+40
13	38	1050	+590	+26	+ 90	1066	+66	+572	+93
14.5	34	1055	578	+40	+182	1122	+48	+561	+97
15.5	35	1041	580	+44	201	1149	+55	+566	+68
17	37	1044	599	+52	218	1158	+56	+570	+67
18.5	38	1046	598	+55	212	1151	+57	+566	+68
20	37	1046	601	+48	216	1145	+58	+565	+70
21.5	+32	1049	606	+50	220	1153	+58	+568	+78
23	+38	1050	602	+52	+222	+1123	+58	+573	+76

Table B.8 Overcoring Strain Reading
Test No. 6 (T6) 26 ft.

C/L Position 9 inches

Depth (inches)	Strain Readings (Microstrain)								
	1	2	3	4	5	6	7	8	9
Init.	50	750	0	100	800	400	0	0	0
5 min.	53	748	4	95	794	397	0	8	0
10 min.	53	744	6	94	796	397	-8	12	-10
2	50	738	-2	95	798	394	-8	13	-6
4	52	743	-8	92	790	400	-6	15	-8
6	55	746	-9	90	820	402	0	46	13
8	60	780	0	105	900	480	10	88	43
10	75	840	66	188	942	560	25	167	62
12	98	877	50	230	940	552	40	180	58
14	94	894	47	228	930	544	34	175	58
15	93	899	44	226	931	548	32	177	57
18	96	896	48	227	932	542	35	176	59
20	94	894	46	227	931	544	34	175	58

Table B.9 Overcoring Strain Readings

Test P-1, 6.5 ft.

C/L Position 11 inches

Bit Depth	Strain Readings (microstrain)								
	1	2	3	4	5	6	7	8	9
Init.	0	0	0	0	0	0	0	0	0
1	0	-10	-10	- 7	- 8	- 2	2	6	-12
2	4	- 7	- 6	- 6	5	00	10	- 2	0
3	- 2	- 3	-10	-10	- 4	- 2	-16	0	0
4	-12	-10	- 8	-14	- 10	4	-20	-10	-10
5	-17	- 2	- 8	-12	- 10	0	-12	- 8	- 8
6	-14	- 6	-13	-13	- 5	- 4	- 8	- 9	-12
7	- 5	-13	-16	-16	- 4	- 5	- 3	-10	- 6
8	- 2	-15	-14	- 4	- 10	-12	- 4	-12	- 4
9	5	-12	3	- 2	- 12	134	5	- 4	4
10	8	44	46	120	-170	208	30	100	60
11	11	155	94	128	-190	214	35	126	68
12	20	189	82	138	-156	209	28	100	42
13	18	162	80	138	-184	172	20	56	38
14	16	156	62	136	-170	160	23	74	39
15	12	154	64	124	-200	145	22	74	45
16	15	168	68	120	-180	152	25	70	42
17	12	160	65	124	-168	160	30	88	42
18	13	162	63	130	-150	154	20	74	41
19	14	145	64	121	-200	162	22	76	43
20	16	162	63	126	- 80	159	21	74	39

Table B.10 Overcoring Strain Readings
 Test P-2 - Depth 14.3'

Bit Depth (in.)	Output (microstrain)								
	1	2	3	4	5	6	7	8	9
0	0	0	0	0	0	0	0	0	0
1	2	0	-2	1	-1	1	-2	-3	-4
2	8	12	4	6	-6	1	-3	-4	-8
3	-2	20	4	7	-2	5	-4	-8	-7
4	8	1	-2	-5	-4	1	0	-6	-7
5	6	-4	-3	-1	-5	-1	4	-10	-7
6	4	-1	-2	-3	2	-1	17	-10	-7
7	8	-4	-5	0	20	-5	32	-13	-8
8	19	-6	2	1	40	-11	18	-10	-5
9	29	-10	22	3	60	-5	-8	-13	-8
10	24	-7	56	11	68	45	-6	-13	-6
11	-16	35	98	34	73	115	8	17	0
12	-28	114	120	42	73	150	8	94	34
13	-24	188	128	60	68	161	20	140	46
14	-12	190	118	68	66	161	24	156	61
15	-8	192	114	70	68	155	24	160	70
16	-8	160	116	66	66	155	24	160	74
17	-8	156	112	66	66	150	24	160	74
18	-8	146	114	60	63	155	24	160	78
19	-8	155	116	66	62	154	24	160	74
20	-8	155	114	58	63	149	28	154	74

Table B. 11 Overcoring Strain Readings
 Test P-3 - Depth 19.6 ft.

Bit Depth (in.)	Output (microstrain)								
	1	2	3	4	5	6	7	8	9
0	0	0	0	0	0	0	0	0	0
1	0	- 6	4	- 2	2	- 2	7	-4	0
2	-1	-12	12	- 2	14	- 9	11	-6	1
3	1	- 6	28	- 2	30	-10	21	-2	7
4	13	-21	54	- 1	43	1	35	9	20
5	17	- 4	76	- 9	94	20	40	45	33
6	34	20	100	-17	114	33	44	50	30
7	52	19	110	- 4	124	36	58	38	33
8	73	20	96	-12	127	32	59	31	36
9	67	16	108	-12	125	32	56	28	33
10	67	14	108	- 6	126	30	53	36	36
11	71	14	104	- 6	122	30	53	38	36
12	66	22	104	- 2	118	30	51	44	34
13	65	19	104	- 2	120	30	52	43	35
14	66	28	104	- 2	119	24	47	44	34
15	70	20	104	2	116	26	47	44	34
16	66	16	105	2	118	28	48	40	36
17	68	20	100	13	120	30	50	36	36
18	66	21	99	1	120	26	55	34	36
19	73	19	103	- 2	104	22	56	31	36
20	66	20	104	3	100	18	49	31	37

Table B.12 Overcoring Strain Readings
 Test P-4 - Depth 25 ft.

Bit Depth (in.)	Output (microstrain)								
	1	2	3	4	5	6	7	8	9
0	0	0	0	0	0	0	0	0	0
1	-7	-2	-1	3	0	13	-5	-8	4
2	-7	-1	-4	4	3	29	-5	34	16
3	1	-2	5	6	5	35	7	55	49
4	3	44	13	35	36	59	9	78	58
5	6	63	14	45	30	88	9	131	59
6	1	77	22	82	34	113	10	135	63
7	1	109	39	78	35	112	12	139	67
8	2	124	35	76	35	109	20	139	68
9	-2	107	33	36	30	117	25	135	69
10	-2	102	26	72	26	107	21	137	69
11	-5	113	39	74	32	96	27	130	71
12	-2	107	23	66	25	95	27	132	71
13	5	101	27	59	20	93	31	135	77
14	0	91	35	52	33	107	35	143	68
15	8	108	33	70	40	107	43	142	72
16	13	107	33	72	34	103	50	139	77
17	15	97	31	72	34	94	33	131	69
18	17	97	29	62	34	89	31	135	77
19	17	91	33	62	30	91	60	121	83
20	27	91	28	60	28	77	81	115	87

Table B.13 Overcoring Strain Readings
 Test P-5 - Depth 29.5'

Bit Depth (in.)	Output (microstrain)								
	1	2	3	4	5	6	7	8	9
0	0	0	0	0	0	0	0	0	0
1	-2	12	14	10	12	4	2	-2	10
2	2	2	6	-2	10	6	4	3	6
3	8	4	18	9	16	8	6	3	6
4	14	6	16	11	17	11	11	5	8
5	10	7	20	13	18	11	13	8	10
6	17	9	21	12	21	11	13	8	14
7	14	-2	20	13	21	9	18	7	16
8	25	-4	22	16	18	2	40	9	25
9	40	3	36	16	29	-2	62	7	33
10	38	14	51	28	45	-6	71	9	40
11	35	62	60	50	62	28	14	13	42
12	30	122	74	104	96	136	-22	28	41
13	-7	144	90	134	137	216	-16	104	43
14	0	160	98	154	152	258	2	162	45
15	6	158	102	176	157	262	4	171	48
16	10	170	106	188	162	268	8	164	44
17	14	162	110	189	160	261	8	158	44
18	17	168	113	187	156	260	9	151	44
19	20	174	113	184	153	261	3	158	38
20	16	166	113	169	146	256	-2	156	32
21	17	170	113	186	138	252	-2	144	29
22	22	178	113	167	136	244	-2	140	24

APPENDIX C

CSM Cell System

C.1 CSM Cell System.

The system components are shown in Figure C.1

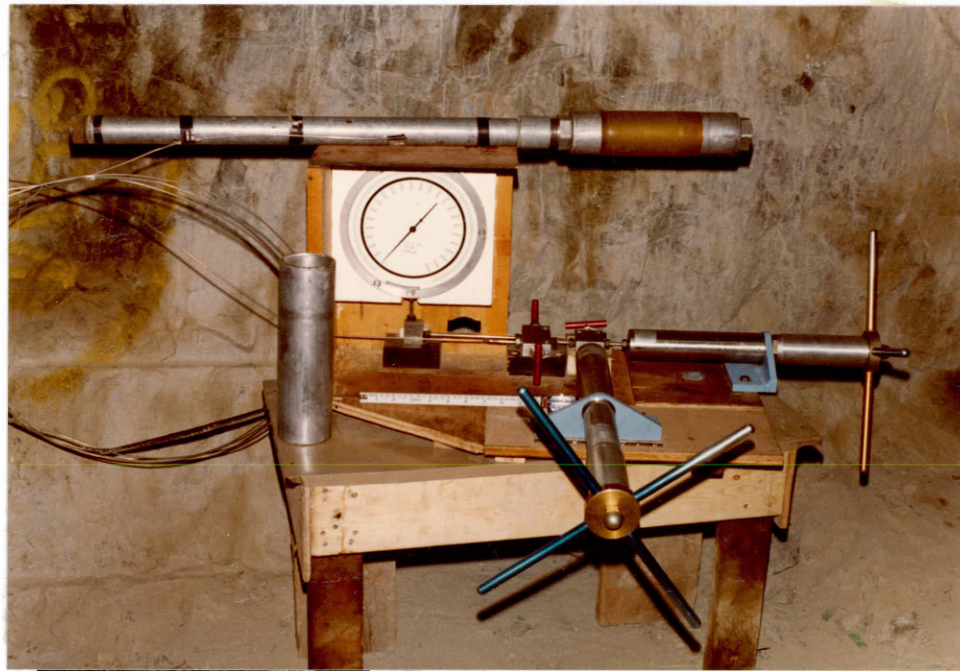


Figure C.1 CSM Cell System.

C.2 CSM-Cell Calibration.

The CSM-cell system was tested in the laboratory to examine its testing procedures and the results.

An aluminum block of 12x12x12 inches was used as a testing material of known elastic properties. The CSM-cell with another calibration cylinder was used to find the elastic properties of the block. The following are the parameters of both the block and the calibration cylinder used in the test.

	Block	Calib. Cylinder
Material	Aluminum	Aluminum
Inner radius (inches)	1.5	1.5
Outer radius (inches)	-	1.744
Elastic modulus (psi)	10.7×10^6	10.7×10^6
Poisson's ratio	0.31	0.31
Hole length (ft.)	1.0	1.25

The system specifications:

Cell membrane length: 6.5 inches

Liquid volume expelled/turn: 0.0435 in.^3

The testing has been carried out in the following sequence; the cell was calibrated three times in the calibration cylinder; the block was tested two times, and the cell then recalibrated three times. The data associated with these tests is given below:

Turns	Pressure in psi		
	Test 1	Test 2	Test 3
20	642	664	690
	758	782	808
21	872	898	925
	990	1017	1042
22	1108	1135	1160
	1222	1255	1276
23	1342	1375	1395
	1465	1499	1515
24	1582	1615	1635
	1700	1749	1755
25	1825	1863	1875
	1942	1980	1995
26	2064	2100	2115
	2180	2219	2238
27	2290	2328	2360
	2390	2430	2483
28	2508	2549	2605
	2625	2668	2724
29	2743	2787	2844
Slope (Mm) psi/turn	234.39	236.62	239.75

Testing the Al-block			Calib. in the Cylinder		
Turns	Pressure psi		Pressure psi		
	Test 4	Test 5	Test 6	Test 7	Test 8
20	450	685	547	610	635
	608	845	667	731	756
21	768	1000	788	852	878
	927	1165	908	972	1000
22	1085	1325	1030	1095	1121
	1245	1485	1150	1215	1243
23	1404	1645	1267	1333	1365
	1563	1805	1390	1455	1485
24	1722	1965	1510	1575	1608
	1881	2130	1631	1695	1730
25	2038	2284	1750	1817	1850
	2198	2442	1870	1938	1975
26	2358	2605	1992	2060	2095
	2516	2764	2112	2180	2215
27	2675	2925	2233	2300	2338
	2835	3085	2353	2420	2460
28	2993	3240	2474	2542	2581
	3154	3400	2594	2660	2700
29	3310	3566	2714	2784	2824
	-	-	2835	2904	2946
	-	-	2955	3025	3067
Slope psi/turn	317.94	319.85	240.82	241.41	243.21

The pressure-volume relationship for tests are found:

Calibration (before) Mm

Test 1: 234.39

Test 2: 236.62

Test 3: 239.75

The average = 236.92 psi/turn

Block testing Mt

Test 4: 317.94

Test 5: 319.85

The average = 318.89 psi/turn

Calibration data (after) Mm

Test 6: 240.82

Test 7: 241.41

Test 8: 243.21

The average = 241.81

The stiffness of the calibration cylinder (Mc) is calculated by the formula given in this appendix, $M_t = 777.046$

The stiffness of the pressuring system (Ms) can be calculated as follows:

$$M_s = \frac{M_c \times M_m}{M_c - M_m}$$

and, hence, the pressure volume relationship (Mr) for the block alone will be

$Mr = \frac{Ms Mt}{Ms - Mt}$ from which the modulus of rigidity of the block could be determined by the equation:

$$Gr = Mr \frac{\pi \times 6.5 \times (1.5)^2}{0.0435}$$

$$Gr = 1056.225 \times Mr$$

and the modulus of elasticity from the relationship:

$$Er = 2(1 + \nu) Gr$$

where ν is the Poisson's ratio of the block material.

By performing the above calculations the elastic modulus of the block is found.

a) Using Mm is the average of calibration slopes, before and after testing

$Mm = (236.92 + 241.81) \div 2 = 239.36$ and Mt the average of tests in the block $Mt = 318.89$

The calculated modulus = 11.3×10^6 psi

b) Using Mm is the average of the calibration slopes, before the block testing

$Mm = 236.92$

$Mt = 318.89$

The calculated modulus = 13.7×10^6 psi.

c) Using Mm is the average of the calibration tests, after the block testing $Mm = 241.81$, $Mt = 318.89$

the calculated modulus = 9.12×10^6 psi.

d) It can be noticed that the relationship between

the pressure-volume were increasing slightly during the testing, so that the following modulus calculation will be made to show the correct data processing:

$$M_m = 239.75 \text{ (Test 3)}$$

$$M_t = 317.94 \text{ (Test 4)}$$

$$\text{The calculated modulus} = 10.6 \times 10^6 \text{ psi}$$

$$\text{or } M_m = 240.82 \text{ (Test 6)}$$

$$M_t = 319.85 \text{ (Test 5)}$$

$$\text{The calculated modulus} = 10.6 \times 10^6 \text{ psi}$$

$$\text{or } M_m = \text{average of test 3 and test 4} = 240.28$$

$$M_t = \text{average of test 5 and test 6} = 318.86$$

$$\text{the calculated modulus} = 10.7 \times 10^6 \text{ psi}$$

The above calculation has shown that, because of the gradual increasing of the system stiffness, the calibration stiffness M_m and testing stiffness M_t are critical values in the modulus calculation, so that these two values should be carefully determined to find the correct modulus.

The result of the above CSM-cell testing that:

- a) The cell calibration should be done before and after the material testing;
- b) The calibration stiffness M_m values to be used in the calculation were the last value before the block testing and the first value after the testing.
- c) The above two values can be averaged for the modulus calculation if one test was done, or the difference

between these values can be normally distributed over the number of tests and give correct results also.

d) The maximum error shown by the above calculation was 28% resulting from using the calibration stiffness Mm before the block testing.

C.3 Rock Mass Modulus Results.

The rock mass modulus results for rings 2 through 6 are shown in Tables C.1 through C.5 and Figures C.2 through C.6.

Depth (ft)	H	VR	VL	DR	DL	DU	DD
19	-	3.32	3.35	-	-	-	-
18	-	3.09	2.67	-	-	-	-
17	-	3.14	3.13	-	-	-	-
16	-	3.42	3.42	-	-	-	-
15	-	4.01	3.31	-	-	-	-
14	5.3	3.12	4.16	5.43	-	2.25	-
13	4.41	4.24	3.32	4.98	6.13	5.43	5.99
12	4.51	5.77	6.28	5.52	7.62	6.16	6.01
11	2.94	5.13	6.32	5.67	7.65	5.49	4.78
10	4.31	4.42	6.44	4.6	8.02	4.02	4.78
9	5.43	5.14	6.42	6.13	2.57	3.52	6.18
8	5.92	5.04	6.55	6.71	2.11	1.74	6.98
7	6.21	5.00	10.09	5.48	2.12	2.43	6.36
6	2.44	4.53	10.3	5.49	1.69	4.75	6.06
5	4.79	4.9	9.59	4.59	5.73	5.46	4.58
4	3.84	1.99	7.59	2.5	6.97	6.1	5.64
3	2.43	5.31	4.62	1.59	7.65	5.26	5.54
2	3.47	8.03	5.84	1.72	4.84	3.07	5.10
1	4.51	6.16	2.66	3.86	6.54	3.91	3.62

Table C.1 Rock Mass Modulus

(Ring No. 2)

 $E_r \times 10^6$ psi

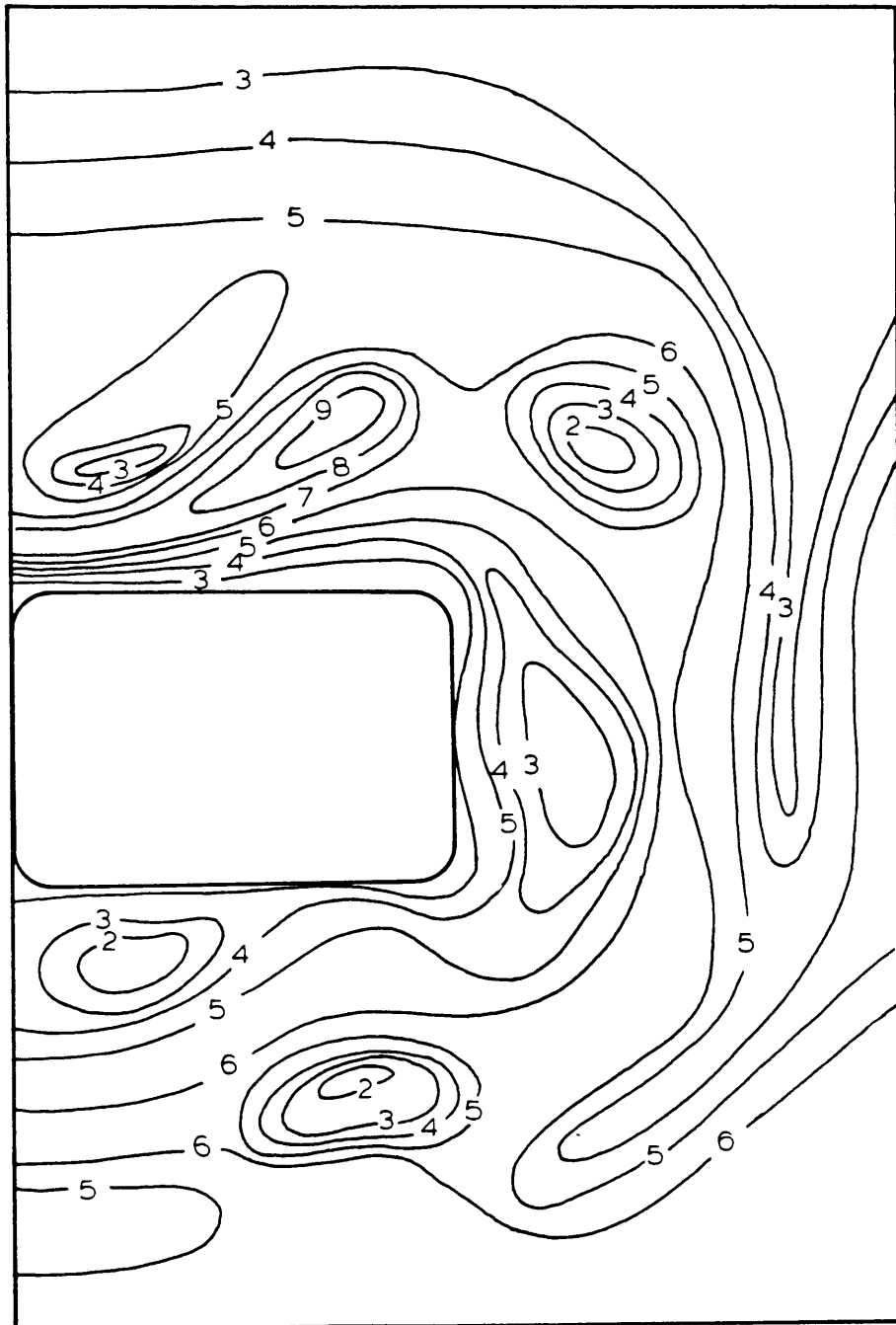


Table C.2 Rock Mass Modulus

(Ring No. 3)

 $E_r \times 10^6$ psi

Depth (ft)	H	VR	VL	DR	DL	DU	DD
19	-	3.01	-	-	-	-	-
18	-	2.96	2.30	-	-	-	-
17	-	2.29	2.21	-	-	-	-
16	-	2.30	2.25	-	-	-	-
15	-	2.83	2.83	-	-	-	-
14	3.92	2.42	3.6	7.0	7.0	3.83	3.32
13	3.89	2.73	4.56	6.8	7.03	3.24	3.58
12	4.34	3.60	4.44	5.4	4.44	3.53	2.83
11	5.48	2.40	3.86	5.22	5.22	2.87	2.86
10	4.87	3.53	1.89	5.83	3.21	5.42	1.59
9	5.02	2.28	2.88	5.03	2.92	3.87	1.38
8	3.05	0.95	3.86	4.87	3.86	3.6	1.44
7	4.59	1.5	3.74	4.81	5.86	3.46	2.8
6	5.90	1.5	3.2	6.0	7.04	3.50	1.87
5	6.05	1.59	2.77	5.9	7.09	3.72	3.24
4	4.57	1.47	2.81	5.9	7.03	3.94	3.50
3	3.89	2.44	2.91	5.87	7.3	5.3	6.4
2	3.87	4.12	4.5	4.18	4.99	6.30	2.43
1	4.45	3.18	2.8	3.03	2.01	2.89	3.13

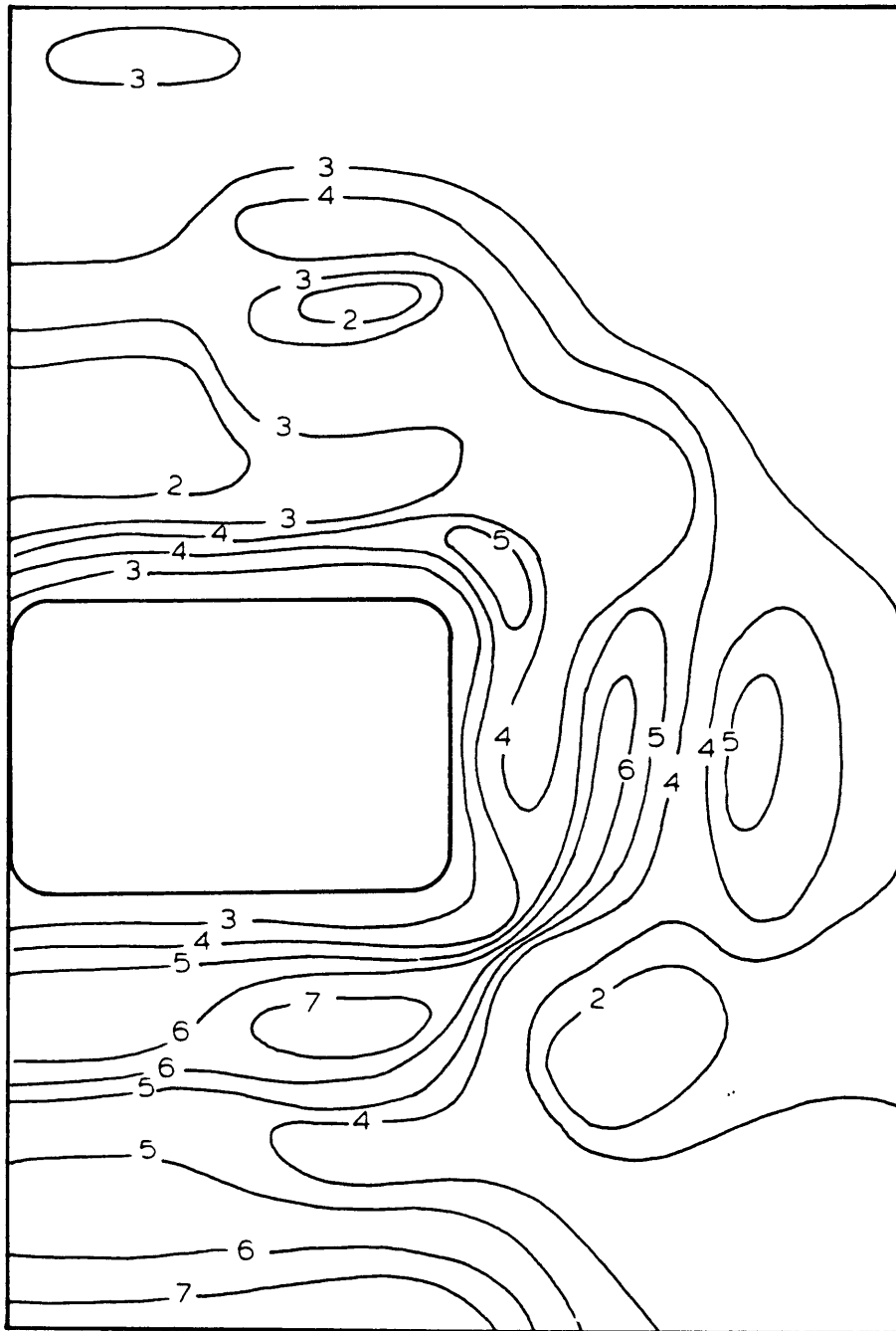
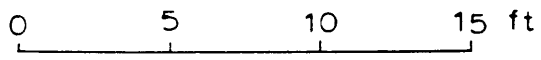


Table C.3 Rock Mass Modulus

(Ring No. 4)

 $E_r \times 10^6$ psi

Depth (ft)	H	VR	VL	DR	DL	DU	DD
19	-	-	-	-	-	-	-
18	-	6.02	5.88	-	-	-	-
17	-	5.39	5.39	-	-	-	-
16	-	5.40	5.08	-	-	-	-
15	-	4.84	5.15	4.36	5.2	-	-
14	3.2	4.84	5.15	4.4	4.7	4.02	5.62
13	6.6	4.84	5.41	4.4	4.4	4.16	5.66
12	5.56	4.20	5.40	4.57	5.44	4.53	4.65
11	5.49	3.84	3.62	7.0	5.87	4.74	5.13
10	7.07	3.87	3.17	7.9	5.4	4.4	5.66
9	6.87	3.89	3.89	7.1	6.10	4.51	7.16
8	6.89	0.86	3.90	7.08	4.87	5.83	6.13
7	6.28	0.95	3.62	3.87	5.42	6.2	5.5
6	6.19	3.01	4.25	5.48	5.23	5.46	3.16
5	6.10	3.73	4.09	3.46	4.5	4.67	5.5
4	6.98	3.63	6.5	6.48	6.2	7.89	11.3?
3	5.45	3.77	5.67	4.77	2.13	9.5	6.65
2	3.89	3.57	6.20	2.12	3.44	6.52	4.24
1	3.25	3.09	3.73	3.16	2.62	6.4	2.61

Table C.4 Rock Mass Modulus

(Ring No. 5)

 $E_r \times 10^6$ psi

Depth (ft)	H	VR	VL	DR	DL	DU	DD
19	-	-	-	-	-	-	-
18	-	3.14	2.87	-	-	-	-
17	-	3.56	2.43	-	-	-	-
16	-	2.46	2.54	-	-	-	-
15	-	2.55	2.56	4.09	-	-	-
14	5.69	2.89	2.43	5.01	2.12	5.13	5.02
13	6.03	3.54	3.13	4.68	2.02	4.84	4.87
12	3.87	3.68	3.89	4.71	1.07	3.5	4.84
11	4.42	4.11	3.90	4.62	3.31	3.31	4.78
10	7.22	5.06	5.07	3.32	2.59	3.14	2.87
9	6.46	4.77	3.01	4.89	2.43	4.47	4.89
8	6.32	4.24	3.37	4.75	3.7	4.81	4.75
7	6.13	4.12	3.39	4.11	2.49	4.34	4.29
6	6.03	5.58	5.52	4.70	.80	4.82	3.05
5	6.66	4.14	1.19	5.25	.53	3.11	2.19
4	5.02	4.64	1.68	4.9	.70	4.81	3.03
3	6.03	3.60	3.68	5.73	6.80	3.5	5.7
2	4.88	4.62	3.09	4.64	0.56	5.03	4.85
1	2.88	3.11	2.34	2.42	1.02	4.94	4.67

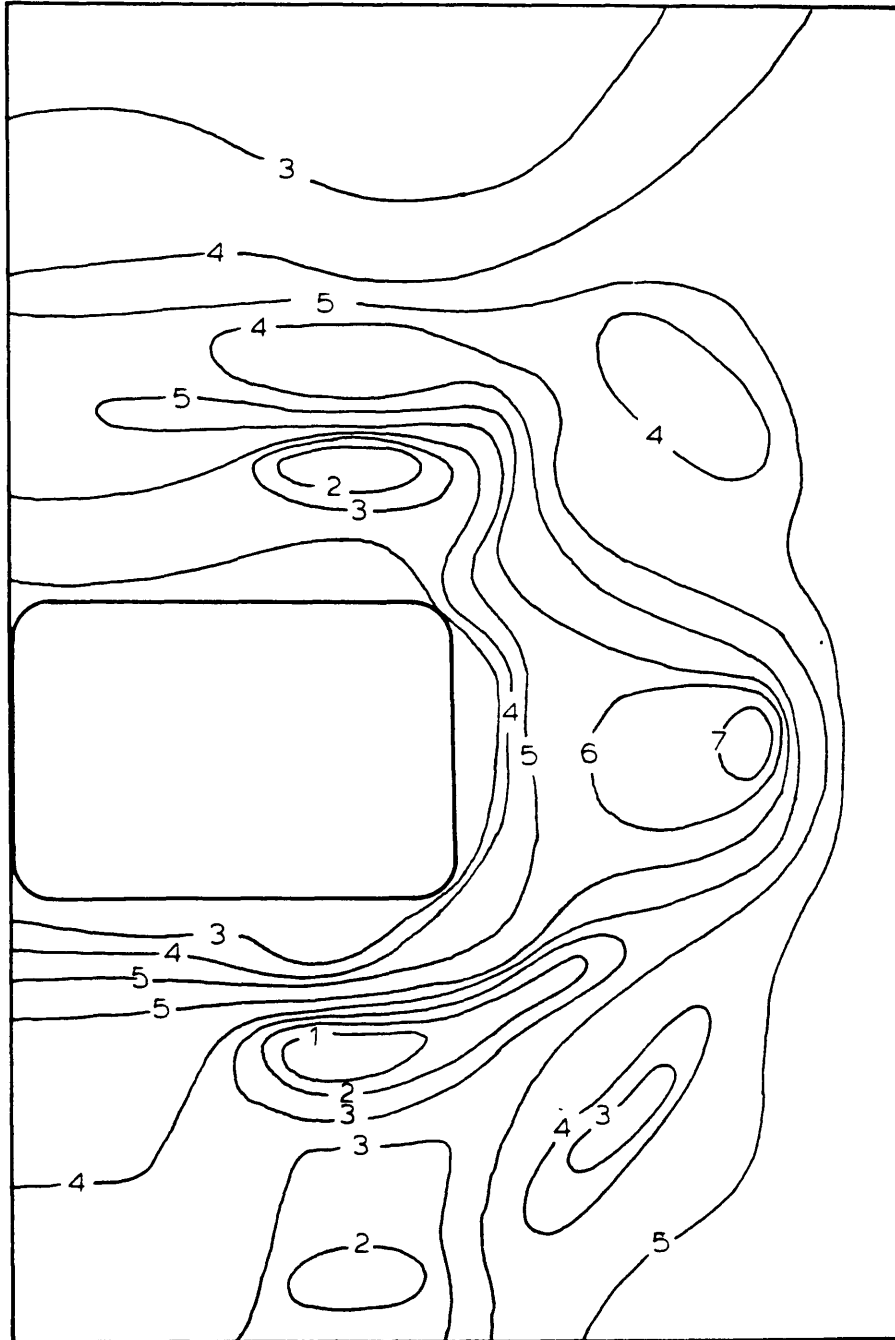
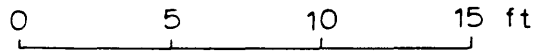
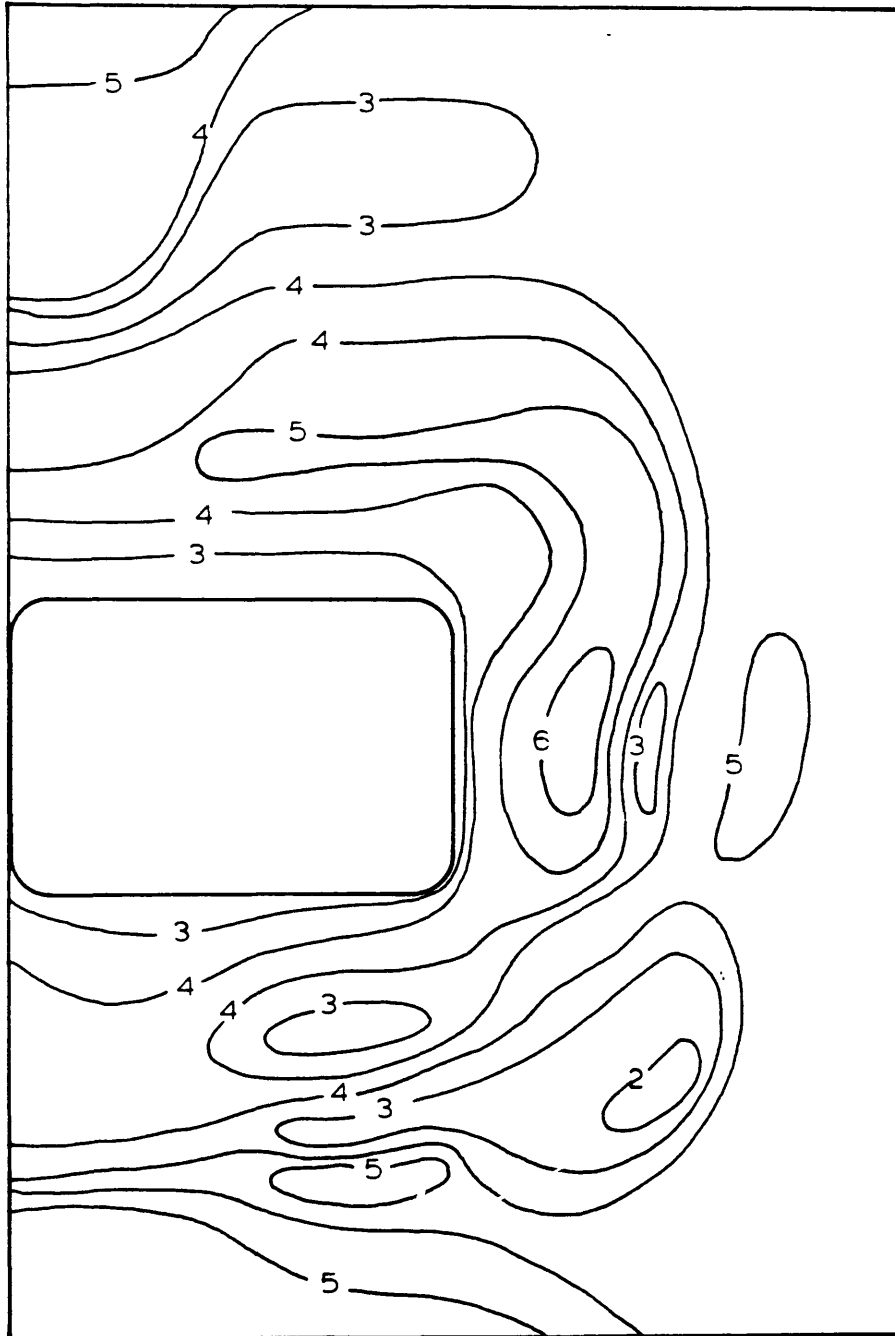
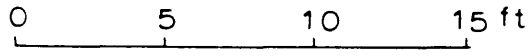


Table C.5 Rock Mass Modulus

(Ring No. 6)

 $E_r \times 10^6$ psi

Depth	H	VR	VL	DR	DL	DU	DD
19	-	5.01	3.36	-	-	-	-
18	-	5.23	3.26	-	-	-	-
17	-	4.76	3.11	-	-	-	-
16	-	4.82	2.78	-	-	-	-
15	-	4.92	2.78	-	-	-	-
14	4.98	4.14	2.34	4.78	5.22	4.76	3.65
13	4.63	4.42	2.72	5.14	4.93	4.22	3.34
12	4.87	4.85	3.94	5.23	4.82	4.64	4.41
11	5.24	4.37	4.58	5.21	3.21	3.79	2.09
10	5.36	4.25	3.75	4.98	5.14	4.22	0.81
9	4.66	2.50	3.49	3.78	5.13	5.12	2.11
8	4.58	4.50	4.35	4.50	2.35	4.88	2.23
7	3.65	4.78	4.28	4.33	4.25	4.26	2.35
6	2.72	4.52	4.85	4.23	3.28	5.22	3.23
5	6.11	4.33	5.49	4.12	2.22	4.66	4.56
4	5.82	3.88	4.18	4.16	2.75	3.41	4.85
3	6.14	4.30	4.14	3.33	4.29	3.81	2.98
2	5.65	3.24	2.21	3.53	3.78	4.62	4.73
1	4.75	2.53	3.77	2.68	4.16	4.41	4.55



C.4 Mathematical Analysis of CSM Cell System. (Hustrulid, 1972)

The system has been modelled using the equations for a thick wall cylinder whose inner surface is acted upon by a uniform pressure (P). The radial displacement of the inner surface is given by:

$$u = \frac{(1+\nu)(1-2\nu)}{E(R^2-r^2)} Pr^3 + \nu_r E_z + \frac{(1+\nu) PR^2 r}{E(R^2-r^2)} \quad (1)$$

where:

u = displacement of inner radius

P = internal pressure (psi)

R = outer radius (in)

r = inner radius (in)

E = Young's modulus (psi)

ν = Poisson's ratio

E_z = strain in axial direction

equation (1) may be rewritten as:

$$u = \frac{(1+\nu)}{E} Pr \left\{ \frac{1+r^2/R^2}{1-r^2/R^2} - \frac{2\nu r^2/R^2}{1-r^2/R^2} \right\} - \nu r E_z \quad (2)$$

Letting $B = r^2/R^2$ equation (2) becomes:

$$u = \frac{(1+\nu)}{E} Pr \left\{ \frac{1+B}{1-B} - \frac{2\nu B}{1-B} \right\} - \nu r E_z \quad (3)$$

For cylinders having a finite length such as those used to calibrate the cell E_z is generally not zero. Under plane strain conditions as would be encountered using the cell in a borehole it will be zero. For our purposes equation (3) can be approximated by:

$$u = \frac{(1+\nu)}{E} Pr \left\{ \frac{1+B}{1-B} - \frac{2\nu B}{1-B} \right\} \quad (4)$$

Since the modulus of rigidity G is given by:

$$G = \frac{E}{2(1+\nu)}$$

equation (4) becomes:

$$u = \frac{Pr}{2G} \left\{ \frac{1+B}{1-B} - \frac{2\nu B}{1-B} \right\} \quad (5)$$

when testing a borehole in a mine $B \rightarrow 0$, and equation (4) can be written as:

$$u = \frac{(1+\nu)}{E} Pr \quad (6a)$$

or,

$$u = \frac{Pr}{2G} \quad (6b)$$

In this case the approximation made in deriving equation (4) becomes exact.

Assume that an internal pressure (P_1) is applied over a length (L) in the calibration cylinder (the subscript c will be used to denote the calibration cylinder values).

G_c = modulus of rigidity

r_c = inner radius

B_c = (ratio of inner to outer radius)²

Using equation (5) the displacement of the hole wall would be:

$$u_1 = \frac{P_1 r_c}{2G_c} \left\{ \frac{1+B_c}{1-B_c} - \frac{2\nu_c B_c}{1-B_c} \right\} \quad (7a)$$

If the applied pressure (P_2) instead of (P_1) the displacement would be

$$u_2 = \frac{P_2 r_c}{2G_c} \left\{ \frac{1+B_c}{1-B_c} - \frac{2\nu_c B_c}{1-B_c} \right\} \quad (7b)$$

The change in the hole volume (ΔV_c) when the pressure is changed from P_1 to P_2 is given by:

$$V_c = \pi L \{ (r_c + u_2)^2 - (r_c - u_1)^2 \} \quad (8)$$

equation (8) can be rewritten as:

$$\Delta V_c = \pi L (u_2 - u_1) (2r_c + u_1 + u_2) \quad (9)$$

since normally:

$$u_1 < r \text{ \& } u_2 < r$$

thus:

$$\Delta V_c = 2 L r_c (u_2 - u_1) \quad (10)$$

Substitution of equations (7a) and 7b) into (10) results in:

$$\Delta V_c = \frac{\pi L}{G_c} r_c^2 (P_2 - P_1) \left\{ \frac{1+B_c}{1-B_c} - \frac{2\nu_c B_c}{1-B_c} \right\} \quad (11)$$

or:

$$\frac{P}{V_c} = \frac{G_c}{\pi L r_c^2 \left[\frac{1+B_c}{1-B_c} - \frac{2V_c B_c}{1-B_c} \right]} \quad (12)$$

It is observed that the volume change of the hole is directly proportional to the pressure change. The total volume of the system can be varied using the pressure generator.

The change in volume of the chamber is given by

$$V_m = n\gamma$$

where:

n = no. of turns

γ = volume per turn

The total system consists of:

1. the pressure generator;
2. the tubing valves and other plumbing;
3. the pressurizing fluid
4. the cell
5. the borehole in which the device is inserted.

As the pressure is increased in the system, the tubing and that portion of the pressure generator in which the fluid is contained expands elastically. The change of volume for each of these is given below.

For the steel tubing:

$$\Delta V_t = \frac{\pi L_t r_t^2}{G_t} (P_2 - P_1) \frac{(1+B_t)}{(1-B_t)} + \frac{2V_t B_t}{1-B_t} \quad (13)$$

For the pressure generator:

$$\Delta V_g = \frac{\pi L_g r_g^2}{G_g} (P_2 - P_1) \frac{(1+B_g)}{(1-B_g)} - \frac{2V_g B_g}{1-B_g} \quad (14)$$

The length (L_g) of the pressure generator will vary directly with the number of turns as shown below:

$$L_g = L_i - \frac{n\gamma}{A_g} \quad (15)$$

where:

L_i = initial chamber length

A_g = cross sectional area of the chamber.

The fluid being compressible will also change in volume with the pressure. The compressibility by definition is given by:

$$K = \frac{V_1 - V_2}{V_1} / P_2 - P_1 \quad (16a)$$

where:

K = compressibility coefficient (pressure⁻¹)

V_1 = initial fluid volume

V_2 = final fluid volume

or:

$$\Delta V_f = - V_1 (P_2 - P_1) K \quad (16b)$$

If some air is trapped in the pressurizing system, an additional volume term must be included. The pressure

volume relationship for air which will be assumed is given below:

$$P_1 V_3 = P_2 V_4 \text{ for isothermal conditions} \quad (17)$$

where:

$$V_3 = \text{volume of air at a pressure } P_1$$

$$V_4 = \text{volume of air at a pressure } P_2$$

equation (17) can be rewritten as

$$V_a = V_4 - V_2 = V_3 \frac{P_1}{P_2} - 1 \quad (18)$$

It is convenient to write (V_3) present at (P_1) in terms of the volume of fluid at that same pressure:

$$V_3 = X V_1 \quad (19)$$

where:

$$X = \text{constant}$$

thus:

$$V_a = X V_1 \frac{P_1}{P_2} - 1 \quad (20)$$

In the use of the CSM cell, the system pressure and the turns through which the piston in the pressure generator is advanced are recorded. The reduction in volume in the pressure generator is balanced by other volume changes in the system.

$$\gamma \Delta n = V_m = \Delta V_c + \Delta V_t + \Delta V_g - \Delta V_f - \Delta V_a \quad (21)$$

by substituting the appropriate values into equation (21)

one finds the volume-pressure relationship is truly linear only if there is no air present in the system (i.e., $x=0$).

If $x = 0$ the relationship becomes:

$$\begin{aligned} \gamma \Delta n = (P_2 - P_1) \pi \left\{ \frac{L_t r_t^2}{G_t} \left[\frac{1+B_t}{1-B_t} - \frac{2v_t B_t}{1-B_t} \right] + \frac{L_g r_g^2}{G_g} \left[\frac{1+B_g}{1-B_g} - \frac{2v_g B_g}{1-B_g} \right] \right. \\ \left. + \frac{L_r^2}{G} \left[\frac{1+B}{1-B} - \frac{2vB}{1-B} \right] + v_1 \frac{k}{\pi} \right. \end{aligned} \quad (22)$$

The relationship between the change in volume $\gamma \Delta n$ and the change in pressure $(P_2 - P_1)$ is now linear. For particular closed system:

$$\begin{aligned} \frac{L_t r_t^2}{G_t} \left[\frac{1+B_t}{1-B_t} - \frac{2v_t B_t}{1-B_t} \right] + \frac{L_g r_g^2}{G_g} \left[\frac{1+B_g}{1-B_g} - \frac{2v_g B_g}{1-B_g} \right] + v_1 \frac{k}{\pi} \\ = C_0 \text{ (constant)} \end{aligned} \quad (23)$$

Theoretical C_0 can be calculated. In reality, however, all of the components of the system have not been included in the above analysis (values, fittings, etc.) and it is more convenient to determine the behavior of the pressurizing system experimentally.

Let the volume change of the entire pressurizing system (including values, etc.) be given as:

$$\Delta V_s = \Delta V_t + \Delta V_g - \Delta V_f - DV_a + \delta \quad (24)$$

where

V_s = volume change due to a change in pressure of ΔP

δ = volume change not included in the terms.

$$\Delta V_t, \Delta V_g, \Delta V_f \text{ and } DV_a$$

Equation (21) can be written in the modified form given below:

$$\Delta V_m = \Delta V_c + \Delta V_s \quad (25)$$

Dividing each side of equation (25) by ΔP one obtains:

$$\frac{\Delta V_m}{\Delta P} = \frac{\Delta V_c}{\Delta P} + \frac{\Delta V_s}{\Delta P} \quad (26)$$

The value $\Delta P/\Delta V_c$ for the calibration cylinder can be calculated using equation (12) and $\Delta P/\Delta V_m$ is measured for calibration cylinder and the pressurizing system, substituting:

$$M_m = \frac{\Delta P}{\Delta V_m}, M_c = \frac{\Delta P}{\Delta V_c}, M_s = \frac{\Delta P}{\Delta V_s} \quad (27)$$

into equation (26) and solving for M_s

$$M_s = \frac{M_m - M_c}{M_c - M_m} \quad (28)$$

If an experiment is then performed in which the CSM cell is used in any other cylinder of unknown modulus, the pressure volume relationship (M_r) for that cylinder can be found from

$$M_r = \frac{M_r M_s}{M_s - M_r} \quad (29)$$

where

$$M_r = (\Delta P/\Delta V_r) \text{ for the unknown rock or material}$$

$M_T = (\Delta P / \Delta V)_T$ for the unknown material plus the pressurizing system.

r = subscripts denoting rock or material properties.

Since, however,

$$M_r = \left(\frac{\Delta P}{\Delta V} \right)_r = \frac{G_r}{\pi L r^2 \left\{ \frac{1+B_r}{1-B_r} - \frac{2v_r B_r}{1-B_r} \right\}} \quad (30)$$

the unknown modulus of rigidity becomes:

$$G_r = M_r \pi L r^2 \left\{ \frac{1+B_r}{1-B_r} - \frac{2v_r B_r}{1-B_r} \right\} \quad (31)$$

The volume change is measured by the number of turns of the pressure generator piston rather than as an absolute volume. For volume displacement of per turn, the required equations become:

$$M_c = \frac{\Delta P}{\Delta r} = \frac{\gamma G_r}{\pi L r_e^2 \left\{ \frac{1+B_c}{1-B_c} - \frac{2v_c B_c}{1-B_c} \right\}} \quad (32)$$

$$M_r = \frac{\Delta P}{\Delta n_r} = \frac{\gamma G_r}{\pi L r^2 \left\{ \frac{1+B_r}{1-B_r} - \frac{2v_r B_r}{1-B_r} \right\}} \quad (33)$$

$$G_r = \frac{M_r \pi L r^2}{\gamma} \frac{1+B_r - 2v_r B_r}{1-B_r} \quad (34)$$

Now, of course, M_m and M_r are measured in terms of the pressure change per turn and M_s is calculated in similar units. Equation (34) will find the modulus of rigidity of

a cylinder of rock. In a borehole in a large rock mass, equation (34) becomes:

$$G_r = \frac{M_r \pi L r_r^2}{\gamma} \quad (35)$$

C.5 CSM-Cell Field Raw Data.

I. Ring No. 1 - Borehole H

Turns	C. B. 1	C. B. 2	14	13	12	11	10
1	1023	970	600	705	615	615	675
2	1250	1212	905	938	920	915	965
3	1485	1455	1200	1170	1225	1230	1267
4	1720	1693	1500	1405	1530	1535	1572
5	1950	1935	1803	1637	1835	1830	1390
6	2190	2180	2102	1870	2140	2145	2200
7	2428	2423	2400	2105	2444	2450	2580
8	2671	2665	2698	2336	2750	2755	2830
9	2915	2907	3003	2570	3055	3060	3132
10	3159	3150	3300	2800			

Turns	9	8	7	6	5	4	3
1	590	560	710	643	445	610	530
2	865	820	1000	920	685	770	785
3	1160	1105	1295	1220	960	950	1060
4	1465	1385	1605	1530	1250	1140	1350
5	1770	1680	1920	1840	1555	1320	1650
6	2085	1975	2250	2160	1865	1530	1950
7	2400	2260	2570	2485	2190	1730	2260
8	2720	2550	2905	2800	2510	1930	2570
9	3030	2850	3215	3118	2800	2140	2880
10					3113	2350	3185

Ring No. 1 (contd.)

Borehole VR

Turns	2	1	C. B.	C. B.	C. B.		
1	465	505	500	590	650		
2	730	780	740	820	890		
3	1020	1070	970	1055	1135		
4	1320	1370	1200	1285	1375		
5	1630	1670	1435	1525	1612		
6	1940	1980	1670	1760	1860		
7	2260	2305	1910	2000	2005		
8	2585	2610	2155	2250	2350		
9	2900	2875	2390	2480	2590		
10	3218	3182	2633	2720	2832		

Borehole VR

Turns	18	17	16	15	14		
1	690	525	580	520	665		
2	1003	810	810	755	960		
3	1310	1095	1065	1025	1270		
4	1631	1385	1335	1310	1585		
5	1950	1665	1620	1615	1900		
6	2270	1954	1905	1925	2220		
7	2590	2235	2200	2235	2540		
8	2910	2525	2484	2550	2838		
9		2800	2755	2862	3135		
10		3088	3025				

Ring No. 1 (contd.) - Borehole VR

Turns	13	12	11	10	9	8	7
1	685	470	480	430	430	515	690
2	975	715	740	710	725	740	1000
3	1280	1000	1015	1000	1020	980	1310
4	1590	1290	1290	1305	1315	1245	1630
5	1900	1590	1540	1600	1620	1515	1950
6	2220	1890	1780	1910	1925	1800	2270
7	2535	2200	1990	2220	2230	2085	2590
8	2852	2500	2240	2520	2530	2360	2905
9	3170	2807	2490	2818	2805	2625	3220
10		3117	2745	3180	3105	2895	

Turns	6	5	4	3	2	1	C. A.
1	540	630	670	485	430	520	500
2	850	950	975	770	655	830	743
3	1170	1270	1280	1060	915	1150	1000
4	1490	1580	1585	1350	1045	1470	1235
5	1810	1910	1890	1645	1325	1800	1480
6	2130	2230	2210	1950	1605	2120	1730
7	2460	2550	2520	2240	1885	2440	1975
8	2785	2880	2835	2540	2165	2770	2215
9	3106	3200	3142	2834	2445	3080	2440
10	3426		3437		2725		2682

Ring No. 1 (contd.)
 Borehole VR Borehole DR

Turns	C.A.	C.B.	C.B.	15	14	13	12
1	420	611	595	540	580	610	490
2	660	860	850	834	870	900	810
3	900	1105	1097	1135	1175	1200	1125
4	1140	1350	1343	1450	1490	1515	1430
5	1385	1600	1590	1744	1785	1815	1750
6	1630	1845	1840	2030	2965	2090	2370
7	1880	2092	2090	2324	2365	2395	2685
8	2130	2340	2335	2615	2655	2680	3005
9	2375	2590	2590	2910	2952	2982	3310
10	2630	2836	2837	3205	3245	3273	

Turns	11	10	9	8	7	6	5
1	540	500	450	558	450	555	445
2	835	790	770	840	730	833	750
3	1140	1095	1085	1115	1000	1112	1060
4	1450	1400	1300	1400	1280	1395	1370
5	1745	1700	1720	1680	1555	1680	1690
6	2030	2000	2045	1970	1835	1970	2010
7	2325	2295	2365	2255	2110	2270	2325
8	2620	2600	2680	2570	2360	2565	2645
9	2900	2905	3000	2855	2660	2850	2960
10	3197				2935	3138	

Ring No. 1 (contd.)

Borehole DR

Turns	4	3	2	1	C.A.	C.A.	
1	543	530	490	575	490	490	
2	860	845	815	885	875	750	
3	1125	1155	1135	1195	1130	1000	
4	1495	1470	1450	1505	1375	1245	
5	1820	1790	1775	1820	1620	1500	
6	2150	2115	2100	2138	1873	1750	
7	2475	2445	2420	2460	2120	2000	
8	2800	2765	2750	2770	2370	2250	
9	31230	3090	3085	2930	2619	2500	
10	-	3250	3410	3244	2868	2750	

Borehole DL

Turns	C.B.	C.B.	13	12	11	10	10
1	490	490	435	490	710	800	750
2	875	750	745	785	1040	1130	1090
3	1130	1000	1060	1085	1370	1462	1425
4	1375	1245	1365	1400	1685	1775	1735
5	1620	1500	1470	1690	2010	2100	2070
6	1873	1750	1980	2000	2330	2422	2385
7	2120	2000	2280	2300	2650	2740	2710
8	2370	2250	2580	2615	2980	3070	3035
9	2619	2500	2880	2920	3300	3395	3355
10	2868	2750					

Ring No. 1 (contd.)

Borehole DL

Turns	9	8	7	6	5	4	3
1	770	620	520	573	570	700	660
2	1070	940	830	893	893	1000	970
3	-	1252	1145	1205	1210	1300	1275
4	1680	1567	1450	1520	1525	1600	1585
5	1980	1877	1755	1830	1840	1900	1885
6	2295	2187	2060	2140	2150	2210	2190
7	2595	2502	2350	2455	2460	2500	2480
8	2910	2807	2660	2760	2770	2800	2770
9	3200	3117	2950	3070	3070	3100	3070
10							

Borehole DD

Turns	2	1	C.A.	C.A.	C.B.	C.B.	14
1	535	610	630	600	590	560	640
2	845	905	880	855	820	800	925
3	1050	1209	1120	1110	1060	1045	1215
4	1390	1510	1365	1355	1305	1280	1530
5	1570	1820	1610	1600	1550	1520	1840
6	1880	2120	1855	1845	1795	1765	2088
7	2380	2425	2105	2095	2033	2010	2380
8	2680	2730	2350	2340	2275	2255	2650
9	2980	3030	2596	2583	2520	2500	2938
10	-	-	-	-	2755	2743	3225

Ring No. 1 (contd.)

Borehole DD

Turns	13	12	11	10	9	9	8
1	800	815	812	585	810	750	635
2	1110	1105	1103	885	1085	1010	921
3	1410	1401	1407	1183	1350	1275	1210
4	1710	1694	1698	1480	1625	1545	1510
5	2010	1994	1998	1780	1905	1820	1800
6	2310	2293	2302	2075	2180	2095	2080
7	2610	2587	2590	2360	2435	2370	2368
8	2910	2880	2889	2640	2680	2650	2640
9	-	3173	3188	2935	2950	2922	2928
10	-	-	-	-	-	-	-

Turns	7	7.5	6	5	4	3.5	3
1	695	615	545	762	830	625	815
2	995	920	845	1030	1145	930	1120
3	1290	1210	1145	1300	1455	1235	1430
4	1585	1505	1455	1580	1770	1545	1745
5	1885	1800	1750	1860	2080	1860	2055
6	2180	2100	2055	2150	2395	2175	2370
7	2465	2400	2355	2430	2705	2490	2690
8	2750	2696	2650	2700	3017	2887	3000
9	3030	2990	2950	2978	3330	3200	3312
10	-	-	-	-	-	-	-

Ring No. 1 (contd.)

Borehole DD

Turns	2.5	2	1.5	1	C.A.	C.B.	C.B.
1	655	737	590	800	740	700	890
2	955	1020	870	1010	970	935	1140
3	1255	1307	1160	1225	1228	1170	1370
4	1555	1600	1450	1450	1470	1405	1623
5	1365	1900	1750	1690	1710	1640	1865
6	2170	2190	2055	1945	1940	1880	2105
7	2475	2480	2350	2180	2160	2120	2345
8	2775	2770	2655	2400	2460	2360	2587
9	3078	3060	2955	2620	2702	2600	2825
10							

Borehole VL

Turns	16	15	14	13	12	11	10
1	793	890	655	710	790	730	612
2	1043	1183	937	1010	1040	1020	890
3	13051	1475	1223	1300	1300	1320	1182
4	1582	1763	1520	1585	1585	1526	1488
5	1862	2070	1822	1895	1860	1930	1789
6	2135	2365	2133	2185	2135	2240	2090'
7	2390	2662	2425	2490	2390	2250	2400
8	2633	2958	2721	2780	2630	2850	2400
9	2901	-	3020	3080	2895		-
10	-	-	-				-

Ring No. 1 (contd.)

Borehole VL

Turns	9	8	7	6	5	4	3
1	700	620	800	750	650	618	790
2	1000	900	1070	1020	935	900	1040
3	1290	1190	1340	1290	1220	1190	1305
4	1575	1482	1630	1570	1520	1480	1580
5	1895	1784	1915	1860	1822	1785	1860
6	2175	2084	2200	2150	2130	2090	2135
7	2480	2380	2480	2425	2426	2380	2390
8	2770	2675	2740	2690	2720	2675	2630
9	3070	2970	3005	2950	3020	2970	2895
10	-	-	-	3227	-	-	-

Borehole DU

Turns	2	1	C.A.	C.A.	C.B.	C.B.	14
1	738	610	875	863	684	835	930
2	1030	890	1125	1105	900	1045	1222
3	1330	1180	1365	1347	1120	1262	1485
4	1536	1490	1615	1595	1332	1475	1760
5	1940	1790	1860	1842	1542	1690	2040
6	2250	2090	2105	1842	1542	1690	2040
7	2560	2400	2350	2085	1753	1912	2315
8	2860	2710	2590	2330	1965	2128	2590
9	3165	3010	2833	2820	2397	2558	
10	-	-	3078	3065			

Ring No. 1 (contd.)

Borehole DU

Turns	13	12	11	10	9	8	7
1	970	670	935	765	760	760	905
2	1246	1030	1227	1040	1035	1033	1175
3	1514	1200	1489	1310	1305	1304	1430
4	1789	1465	1766	1590	1587	1583	1710
5	2064	1735	2045	1875	1870	1870	1980
6	2344	2005	2321	2145	2140	2140	2250
7	2070	2275	2595	2413	2410	2405	2520
8	2344	2535	2871	2688	2686	2684	2790
9	2618	2795	3131	2964	2961	2955	3060
10	-	-	-	-			

Turns	6	5	4	3	2	1	C.A.
1	740	930	675	696	965	810	710
2	1020	1220	1035	970	1215	1060	910
3	1290	1490	1200	1245	1450	1300	1110
4	1570	1760	1470	1515	1700	1550	1310
5	1840	2040	1740	1788	1940	1800	1512
6	2105	2315	2010	2065	2200	2050	1760
7	2370	2590	2280	2345	2444	2297	1950
8	2642	2865	2540	2619	2689	2544	2165
9	2914	3140	2800	2893	2932	2790	2380
10							

Ring No. 2

Borehole H

Turns	C.B.	C.B.	14	13	12	11	10
1	875	863	730	595	795	600	775
2	1125	1105	1035	885	1070	860	1060
3	1365	1347	1325	1175	1360	1115	1350
4	1615	1595	1640	1470	1660	1380	1640
5	1860	1845	1950	1775	1965	1660	1950
6	2105	2085	2235	2070	2270	1940	2255
7	2350	2330	2600	2375	2570	2220	2550
8	2590	2580	2910	2680	2880	2500	2840
9	2833	2820	3220	2978	3179	2774	3135
10	3078	3066	-				

Turns	9	8	7	6	5	4	3
1	710	840	780	670	730	695	600
2	1010	1150	1090	915	1030	980	865
3	1312	1460	1400	1190	1320	1270	1115
4	1610	1770	1710	1470	1625	1565	1395
5	1920	2085	2020	1731	1930	1855	1610
6	2230	2400	2340	1992	2235	2145	1950
7	2550	2710	2670	2255	2545	2435	2222
8	2870	3022	2984	2515	2847	2726	-
9	3178	-	-	-	3150	3015	-
10	-	-	-	-	-		-

Ring No. 2 (contd.)

Borehole H

Turns	2	1	C.A.	C.A.	C.A.	C.B.	C.B.
1	700	825	750	730	725	870	860
2	985	1140	990	975	975	1105	1100
3	1275	1455	1240	1225	1220	1337	1330
4	1570	1770	1490	1475	1470	1570	1565
5	1860	2090	1730	1720	1715	1805	1795
6	2150	2410	1975	1965	1960	2035	2029
7	2440	2730	2220	2215	2210	2272	2268
8	-	3045	2465	2460	2455	2505	2502
9	-	-	2710	2707	2704	2739	2735
10	-	-	-	-	-	-	-

Borehole DD

Turns	13	12	11	10	9	8	7
1	920	922	760	760	780	850	840
2	1225	1225	1040	1040	1065	1150	1138
3	1520	1523	1320	1320	1345	1450	1435
4	1810	1815	1600	1600	1625	1745	1725
5	2100	2105	1820	1820	1905	2045	2025
6	2380	2385	2181	2180	2180	2340	2330
7	2671	2670	2440	2443	2460	2638	2627
8	2965	2967	2722	2725	2740	2936	2924
9	-	-	3005	3000	3020	-	-
10	-	-	-	-	-	-	-

Ring No. 2 (contd.)

Borehole DD

Turns	6	5	4	3	2	1	C.A.
1	850	760	980	775	830	850	880
2	1148	1030	1275	1060	1120	1125	1115
3	1432	1310	1560	1345	1405	1390	1345
4	1720	1593	1850	1640	1685	1660	1570
5	2020	1880	2140	1930	1980	1930	1793
6	2315	2160	2430	2225	2265	2200	2025
7	2607	2441	2719	2500	2542	2470	2262
8	2899	2722	3008	2789	2825	2740	2492
9	-	3005	3297	3078	3110	3007	2722
10	-						-

Borehole DL

Turns	C.A.	13	12	11	10	9	8
1	840	720	940	820	900	880	920
2	1080	1000	1240	1121	1220	1195	1150
3	1318	1300	1540	1412	1520	1500	1375
4	1550	1592	1842	1718	1815	1800	1610
5	1781	1885	2140	2021	2125	2100	1850
6	2012	2180	2440	2320	2425	2405	2100
7	2250	2470	2740	2620	2725	2705	2340
8	2482	2762	3040	2920	3027	3008	2676
9	2715	3055	-	3223	-	-	-
10	-	-	-	-	-	-	-

Ring No. 2

Borehole DD

Turns	7	6	5	4	3	2	1
1	850	810	860	860	820	845	840
2	2200	1030	1150	1161	1121	1120	1140
3	1350	1240	1435	1460	1412	1465	1430
4	1600	1460	1730	1760	1718	1685	1720
5	1850	1680	2020	2055	2020	1975	2020
6	2100	1910	2310	2350	2320	2260	2320
7	2350	2130	2600	2642	2620	2540	2610
8	2600	2350	2890	2939	2920	2823	2905
9	2851	2572	3180	3236	-	-	-
10	-	-	-	-	-	-	-

Borehole VL

Turns	C.A.	C.A.	C.B.	C.B.	19	18	17
1	920	870	720	700	730	725	777
2	1143	1105	955	935	970	960	1025
3	1370	1340	1190	1178	1223	1200	1275
4	1600	1580	1420	1410	1495	1455	1532
5	1830	1820	1652	1635	1754	1720	1790
6	2061	2050	1890	1880	2036	1975	2045
7	2295	2285	1890	1880	2036	1975	2045
8	2525	2521	2120	2110	2320	2235	2303
9	-	2757	2353	2344	2587	2487	2560
10	-	-	2586	-	-	-	-

Ring No. 2 (contd.)

Borehole VL

Turns	16	15	14	13	12	11	10
1	830	725	735	750	710	715	758
2	1090	965	1005	990	992	997	1043
3	1350	1220	1270	1245	1280	1285	1335
4	1610	1490	1600	1515	1578	1579	1622
5	1875	1755	1830	1780	1872	1877	1928
6	2145	2035	2115	2060	2175	2179	2228
7	2400	2310	2395	2340	2471	2473	2526
8	2662	2575	2675	2606	2764	2767	2821
9	2925	2841	-	-	-	-	-
10	-	-	-	-	-	-	-

Turns	9	8	7	6	5	4	3
1	750	635	673	769	738	723	722
2	1040	912	972	1068	1025	1016	1002
3	1336	1204	1288	1375	1330	1322	1289
4	1624	1492	1593	1677	1632	1622	1572
5	1925	1792	1908	1995	1949	1922	1853
6	2226	2100	2228	2310	2260	2222	2138
7	2523	2408	2543	2618	2573	2525	2409
8	2818	2703	2855	2926	2879	2824	2691
9	-	-	-	-	-	-	-
10	-	-	-	-	-	-	-

Borehole VL

Borehole DU

Turns	2	1	C.A.	C.B.	14	13	12
1	767	732	590	750	760	720	770
2	1058	983	824	970	1030	1000	1040
3	1342	1232	1058	1192	1300	1280	1200
4	1642	1495	1292	1405	1575	1550	1570
5	1931	1750	1526	1620	1845	1805	1840
6	2228	2002	1261	1835	2115	2080	2100
7	2513	2238	1995	2050	2340	2345	2366
8	2805	2490	2228	2266	2565	2610	2632
9	-	-	2463				
10	-	-					

Turns	11	10	9	8	7	6	5
1	800	765	770	750	780	760	745
2	1070	1015	1000	940	1110	1030	1020
3	1090	1260	1280	1135	1240	1280	1270
4	1590	1515	1500	1335	1475	1540	1540
5	1880	1770	1840	1550	1715	1800	1805
6	2100	2020	2100	1770	1955	2050	2065
7	2360	2271	2330	1990	2180	2307	2320
8	2620	2522	2565	2197	2407	2564	2582
9	-	-	-	2404	2635	-	2844
10	-	-	-	-	-	-	-

Ring No. 2 (contd.)

Borehole DU

Borehole VR

Turns	2	1	C.A.	19	18	17	16
1	900	740	610	740	750	727	705
2	1100	985	826	965	970	962	965
3	1340	1235	1043	1205	1210	1208	1215
4	1585	1480	1259	1450	1450	1466	1485
5	1830	1730	1476	1691	1690	1710	1735
6	2085	1990	1692	1968	1965	1990	2015
7	2323	2240	1909	2182	2180	2235	2290
8	2562	2490	2125	2425	2420	2493	2565
9	2800	2740	2343	2843	2842	-	-
10	-	-	-	-	-	-	-

Turns	15	14	13	12	11	10	9
1	1000	1000	740	735	800	725	710
2	1245	1230	1000	995	1010	980	950
3	1495	1465	1256	1250	1280	2220	1210
4	1765	1705	1520	1515	1550	1470	1470
5	2015	1950	1800	1785	1810	1730	1733
6	2270	2200	2076	2058	2100	2000	2000
7	2530	2440	2342	2322	2365	2255	2250
8	2785	2685	2612	2586	2635	2510	2504
9	-	2925	2878	-	2905	2765	2754
10	-	-	-	-	-	-	-

Ring No. 2 (contd.)

Borehole VR

Turns	8	7	6	5	4	3	2
1	740	760	719	715	765	745	768
2	995	965	975	955	970	985	1038
3	1245	1175	1230	1215	1180	1233	1304
4	1508	1385	1485	1475	1390	1494	1578
5	1772	1605	1740	1735	1610	1768	1853
6	2040	1835	2000	2005	1840	2032	2138
7	2300	2070	2256	2265	2055	2310	2411
8	2560	2305	2512	2523	2270	2571	2684
9	-	2550	2768	2782	2490	-	-
10	-	-	-	-	-	-	-

Borehole DL

Turns	1	C.A.	C.B.	13	12	11	10
1	715	730	840	720	940	820	900
2	965	950	1080	1000	1240	1121	1220
3	1132	1180	1318	1300	1540	1412	1520
4	1495	1400	1550	1592	1842	1718	1815
5	1758	1620	1781	1885	2140	2021	2125
6	2025	1835	2012	2180	2440	2320	2425
7	2285	2045	2250	2470	2740	2617	2726
8	2551	2264	2484	2762	-	2914	3027
9	2812	2482	2718	3055	-	3211	-
10	-	-	-	-	-	-	-

Ring #2 (contd.)

Borehole DL

Turns	9	8	7	6	5	4	3
1	880	920	850	809	860	860	820
2	1195	1150	1100	1030	1150	1160	1121
3	1500	1375	1350	1240	1435	1460	1412
4	1800	1610	1600	1460	1730	1760	1718
5	2100	1850	1850	1680	2020	2055	2020
6	2405	2100	2100	1910	2310	2350	2320
7	2705	2340	2350	2130	2600	2642	2620
8	3008	2577	2600	2350	2890	2939	2920
9	-	2814	2850	2570	3181	3235	-
10	-	-	-	-	-	-	-

Borehole DR

Turns	2	1	C.A.	C.B.	14	13	12
1	845	840	877	715	705	730	715
2	1120	1140	1110	930	960	1055	970
3	1465	1430	1345	1145	1220	1200	1230
4	1685	1720	1580	1355	1473	1435	1485
5	1975	2020	1815	1565	1744	1690	1755
6	2260	2320	2041	1780	2015	1950	2925
7	2540	2610	2280	1990	2282	2215	2290
8	2823	2905	2513	2210	2250	2471	2552
9	3105	3200	-	2423	2804	2727	2814
10	-	-	-	-	-	-	-

Ring No. 2 (contd.)

Borehole DR

Turns	11	10	9	8	7	6	5
1	740	750	750	730	750	765	740
2	1000	1075	1025	995	1015	1030	1000
3	1260	1210	1280	1255	1260	1285	1250
4	1520	1455	1550	1525	1540	1545	1510
5	1780	1710	1815	1795	1815	1815	1770
6	1990	1972	2085	2080	2078	2080	2020
7	2205	2235	2351	2335	2340	2345	2280
8	2405	2490	2617	2603	2602	2600	2536
9	2612	2747	2885	2871	2865	2862	2793
10	2819	-	-	-	-	-	-

Turns	4	3	2	1	C.A.	C.A.	
1	740	742	770	720	760	750	
2	965	945	985	975	970	970	
3	1180	1140	1190	1220	1182	1192	
4	1410	1340	1392	1470	1385	1405	
5	1645	1542	1605	1720	1593	1620	
6	1880	1748	1810	1970	1800	1835	
7	2110	1950	2010	2219	2010	2050	
8	2340	2150	2216	2468	2228	2265	
9	2568	2351	2422	2713	-	-	
10	-	-	-	-	-	-	

Ring No. 3

Borehole H

Turns	C.B.	C.B.	14	13	12	11	10
1	620	780	790	830	705	680	700
2	850	1030	1080	1110	985	975	980
3	1070	1275	1380	1394	1275	1273	1270
4	1310	1520	1685	1685	1570	1573	1565
5	1540	1760	1990	1980	1866	1875	1865
6	1780	2000	2305	2267	2154	2170	2150
7	2015	2250	2610	2554	2445	2460	2445
8	2255	2490	2910	2842	2735	2750	2730
9	2500	2733	3195	-	3026	3046	3021
10	-	2968	3481	-	3317	-	-

Turns	9	8	C.A.	C.B.	7	6	
1	600	630	710	850	805	750	830
2	850	890	944	1095	1050	1040	1150
3	1140	1160	1149	1335	1290	1320	1465
4	1430	1440	1413	1580	1535	1610	1780
5	1730	1715	1647	1820	1780	1900	2095
6	2030	1940	1880	2060	2020	2190	2380
7	2332	2230	2116	2300	2265	2480	2690
8	2630	2500	2351	2540	2505	2770	3010
9	2922	2767	2585	2770	2740	3058	-
10	3215	-	-	-	2982	-	-

Ring No. 3

Borehole H

Turns	5	4	3	2	1	C.A.	C.A.
1	885	920	790	830	660	580	800
2	1180	1205	1080	1110	950	820	1045
3	1485	1495	1380	1395	1245	1065	1295
4	1785	1780	1685	1685	1550	1305	1545
5	2085	2070	1990	1980	1850	1550	1792
6	2385	2360	2305	2267	2148	1800	2040
7	2685	2650	2610	2555	2446	2045	2285
8	-	2938	2910	2843	2740	2290	2535
9	-	3226	3197	-	3036	2534	2782
10	-	-	-	-	-	-	-

Borehole VL

Turns	C.B.	C.B.	18	17	16	15	14
1	1973	1957	1730	1612	1650	1680	1810
2	2193	2185	1990	1865	1903	1955	2070
3	2424	2419	2240	2118	2156	2215	2330
4	2539	2655	2495	2372	2409	2455	2590
5	2653	2885	2750	2624	2662	2700	2850
6	2879	3118	3005	2875	2915	2955	3110
7	3107	3351	3260	3130	3168	3205	3370
8	3335	3583	3515	3383	3421	3457	3630
9	-	-	-	-	3675	-	-
10	-	-	-	-	-	-	-

Ring No. 3 (contd.)

Borehole VR

Turns	13	12	11	10	9	8	7
1	1860	1840	1310	1985	1010	985	1019
2	2110	2095	1535	2260	1262	1140	1209
3	2360	2350	1770	2535	1515	1310	1409
4	2610	2605	2005	2805	1765	1485	1600
5	2860	2860	2243	3060	2018	1660	1789
6	3110	3115	2475	3300	2270	1840	1970
7	3360	3370	2710	3564	2522	2010	2150
8	3610	3625	2944	3828	2775	2185	2330
9	-	2882	3178	-	3026	-	2510
10	-	-	-	-	-	-	-

Turns	6	6	5	4	3	2	1
1	1190	868	1170	1130	1370	1083	1345
2	1415	1075	1375	1345	1610	1330	1590
3	1635	1275	1590	1545	1850	1595	1850
4	1850	1480	1810	1755	2090	1870	2110
5	2060	1685	2020	1960	2340	2155	2380
6	2277	1895	2233	2165	2586	2435	2630
7	2495	2099	2445	2375	2829	2706	2888
8	2711	2300	2659	2581	3072	2978	3145
9	2928	2507	2875	-	3315	3248	3405
10	-	-	-	-	-	-	-

Ring No. 3 (contd.)

Borehole VR

Borehole VL

Turns	C.A.	C.A.	18	17	16	15	14
1	1040	1000	1115	1125	1010	1000	1180
2	1258	1234	1347	1350	1250	1242	1435
3	1485	1465	1579	1590	1490	1485	1700
4	1711	1695	1811	1830	1730	1715	1970
5	1945	1930	2043	2070	1972	1968	2240
6	2175	2168	2275	2310	2210	2210	2510
7	2402	2400	2507	2550	2450	2452	2775
8	2629	2633	2740	2788	2692	2695	3042
9	2857	2866	2973	3027	2933	2936	-
10	-	3100	3203	3265	-	-	-

Turns	13	12	11	10	9	8	7
1	980	1072	990	1085	1010	1174	995
2	1256	1335	1256	1300	1252	1440	1263
3	1530	1610	1522	1510	1495	1710	1530
4	1810	1890	1788	1730	1733	1985	1860
5	2085	2170	2054	1960	1975	2255	2067
6	2360	2450	2325	2200	2215	2525	2335
7	2636	2730	2586	2435	2456	2795	2600
8	2912	3007	2852	2675	2697	3245	2870
9	3188	3285	3120	2902	2938	-	3140
10	-		-	-		-	

Ring No. 3 (contd.)

Borehole VL

Turns	6	5	4	3	2	1	C.A.
1	1030	963	970	980	915	1015	1165
2	1275	1150	1210	1220	1180	1255	1385
3	1530	1350	1455	1470	1443	1505	1615
4	1790	1550	1705	1722	1722	1755	1843
5	2050	1750	1963	1983	2002	2010	2070
6	2320	1970	2225	2247	2290	2270	2305
7	2590	2200	2490	2510	2573	2525	2530
8	2850	2405	2743	2765	2849	2777	2758
9	3110	2610	2995	3020	3125	3030	2987
10	-	-	-	-	-	-	

Borehole DL

Turns	C.A.	14	13	12	11	10	9
1	1123	1005	915	995	1100	975	935
2	1350	1297	1210	1275	1386	1233	1185
3	1590	1589	1505	1555	1672	1492	1452
4	1825	1881	1795	1835	1960	1750	1720
5	2058	2175	2090	2115	2240	2010	1980
6	2298	2465	2385	2395	2530	2270	2220
7	2525	2757	2680	2675	2816	2528	2460
8	2759	3050	2970	2955	3102	2787	2716
9	2995	3340	3267	3235	3388	3046	2972
10	-	-	-	-	-	-	-

Ring No. 3

Borehole DL

Turns	8	7	6	5	4	3	2
1	1052	870	1021	890	1007	1075	1109
2	1350	1135	1320	1165	1293	1375	1390
3	1650	1428	1625	1460	1593	1670	1675
4	1950	1719	1930	1755	1390	1970	1965
5	2250	2011	2230	2055	2185	2265	2250
6	2550	2300	2530	2350	2475	2555	2520
7	-	2587	2830	2645	2765	2845	2793
8	-	2874	3131	2938	3059	3142	3074
9	-	2160	3432	3232	3352	3435	3355
10	-		-	-	-	-	-

Borehole DU

Turns	1	C.A.	14	13	12	11	10
1	989	950	870	1105	920	1010	900
2	1205	1173	1140	1367	1186	1265	1184
3	1430	1403	1410	1630	1452	1520	1470
4	1665	1638	1680	1890	1720	1775	1752
5	1900	1870	1950	2153	1984	2030	2036
6	2140	2150	2220	2415	2250	2285	2320
7	2385	2349	2490	2677	2516	2540	2604
8	2618	2572	2760	2940	2782	2795	2888
9	2850	2805	3030	3200	3050	3050	3172
10	3085	3038	-	-	-	-	-

Ring No. 3

Borehole DU

Turns	9	8	7	6	5	4	3
1	890	880	960	950	815	850	930
2	1160	1147	1215	1214	1063	1120	1195
3	1428	1415	1475	1480	1339	1392	1480
4	1697	1680	1740	1740	1605	1665	1770
5	1965	1950	2010	2000	1878	1940	2060
6	2235	2215	2280	2275	2150	2210	2348
7	2504	2482	2547	2540	2420	2475	2620
8	2773	2750	2812	2800	2688	2745	2904
9	3042	3015	3077	3070	2955	3011	3188
10		-	-	-	-	-	-

Borehole DD

Turns	2	1	C.A.	C.B.	C.B.	14	13
1	961	842	940	715	870	725	620
2	1245	1090	1168	950	1105	1000	880
3	1540	1340	1395	1182	1340	1273	1138
4	1835	1597	1630	1417	1575	1545	1400
5	2128	1833	1868	1650	1810	1819	1660
6	2411	2053	2100	1885	2045	2093	1920
7	2700	2290	2335	2120	2280	2365	2180
8	2990	2531	2570	2353	2515	2638	2442
9	3280	2772	2803	2587	2750	2911	2698
10	-	-	3036	2821	2985	3184	2960

Ring No. 3 (contd.)

Borehole DD

Turns	12	11	10	9	8	7	6
1	770	817	915	880	740	930	815
2	1030	1077	1140	1100	963	1188	1045
3	1290	1337	1365	1320	1186	1446	1275
4	1550	1595	1590	1540	1409	1705	1505
5	1810	1859	1815	1760	1630	1962	1735
6	2070	2117	2040	1980	1855	2220	1935
7	2330	2380	2265	2200	2078	2478	2195
8	2592	2634	2490	2422	2301	2736	2425
9	2848	2900	2715	2640	2524	2995	2655
10	-	-	2940	2860	2750	3252	2885

Turns	5	4	3	2	1	C.A.	C.A.
1	1000	990	800	710	705	790	812
2	1264	1260	1097	954	967	1025	1050
3	1530	1530	1395	1198	1230	1260	1285
4	1792	1800	1691	1442	1490	1495	1520
5	2056	2070	1988	1686	1755	1730	1755
6	2320	2340	2285	1930	2015	1965	1990
7	2584	2611	2582	2174	2277	2200	2230
8	2848	2880	2880	2418	2539	2435	2462
9	3112	3150	3175	2662	2800	2670	2700
10	-	-	-	-	3065	-	-

Ring No. 4

Borehole H

Turns	C.B.	C.B.	14	13	12	11	10
1	800	800	660	875	680	745	940
2	1044	1045	960	1190	970	1030	1250
3	1288	1295	1250	1510	1275	1340	1570
4	1532	1545	1534	1830	1590	1650	1885
5	1775	1792	1830	2140	1910	1970	2210
6	2020	2040	2120	2460	2225	2285	2540
7	2265	2285	2418	2777	2535	2594	2859
8	2508	2525	2720	3094	2845	2903	3178
9	2753	2772	3012	3411	3155	3212	3495
10	2995	3019	3304	-	-	-	-

Turns	9	8	7	6	5	4	3
1	690	625	720	725	900	725	970
2	990	930	1020	1025	1220	1030	1280
3	1300	1230	1325	1335	1540	1330	1590
4	1615	1545	1640	1650	1860	1635	1920
5	1940	1865	1060	1965	2190	1950	2230
6	2270	2190	2285	2290	2500	2270	2540
7	2600	2515	2615	2620	2820	2590	2850
8	2919	2830	2931	2935	3140	2900	3160
9	3237	3145	3247	3250	3460	3210	3470
10	-	-	-	-			-

Ring No. 4 (contd.)

Borehole H

Borehole DD

Turns	2	1	C.A.	C.A.	C.B.	C.B.	14
1	660	428	805	1040	940	934	900
2	940	720	1050	1285	1170	1165	1192
3	1225	1010	1300	-	1402	1402	1495
4	1525	1300	1550	1780	1640	1637	1775
5	1820	1590	1798	2035	1877	1873	2072
6	2120	1885	2040	2275	2107	2105	2358
7	2425	2185	2285	2523	2339	2338	2650
8	2719	2477	2532	2771	2573	2572	2940
9	3013	2770	2779	3020	2807	2807	3230
10	-	3061	3025	3267	-	3040	-

Turns	13	12	11	10	9	8	7
1	900	1000	910	1010	937	870	863
2	1192	1282	1199	1300	1237	1160	1163
3	1495	1572	1498	1610	1535	1458	1451
4	1775	1860	1785	1900	1838	1752	1750
5	2070	2150	2082	2195	2140	2050	2938
6	2360	2430	2365	2475	2440	2340	2332
7	2650	2690	2652	2760	2738	2630	2621
8	2940	2972	2950	3051	3038	2924	2906
9	3230	3265	3225	3342	3339	3218	3192
10	-	-	-	-	-	-	-

Ring No. 4 (contd.)

Borehole DD

Turns	6	5	4	3	2	1	C.A.
1	822	980	810	1000	919	840	817
2	1110	1290	1101	1303	1215	1110	1051
3	1420	1595	1415	1597	1517	1400	1285
4	1710	1885	1730	1891	1815	1660	1520
5	1900	2175	2042	2185	2113	1900	1755
6	2180	2465	2360	2480	2410	2151	1988
7	2460	2755	2672	2774	2695	2402	2220
8	2723	3045	2984	3068	2992	2653	2457
9	2986	3335	3295	3362	3289	2904	2690
10	3250	-	-		-	-	2925

Borehole DR

Turns	15	14	13	12	11	10	9
1	850	843	866	843	740	853	738
2	1130	1123	1147	1110	1001	1150	1000
3	1410	1403	1428	1392	1294	1458	1293
4	1690	1685	1709	1678	1587	1763	1587
5	1970	1963	1991	1965	1883	2063	1880
6	2250	2244	2270	2246	2177	2063	2180
7	2530	2525	2525	2528	2467	2363	2470
8	2810	2805	2833	2810	2766	2665	2769
9	3090	3085	3114	3095	3065	2965	3068
10	-	-	-	-	-	3267	3367

Ring No. 4 (contd.)

Borehole DR

Turns	8	7	6	5	4	3	2
1	832	892	740	893	1000	880	990
2	1115	1061	1000	1057	1290	1152	1229
3	1425	1348	1293	1340	1585	1438	1469
4	1722	1630	1588	1626	1887	1721	1710
5	2022	1921	1887	1909	2182	2010	1952
6	2322	2187	2173	2186	2477	2296	2180
7	2621	2467	2465	2455	2773	2578	2420
8	2920	2739	2755	2723	3070	2862	2658
9	3220	3010	3043	2990	3365	3146	2895
10	-	-	-	3560	-	-	-

Borehole DU

Turns	1	C.A.	C.A.	C.B.	14	13	12
1	913	700	795	865	720	815	1018
2	1175	920	1025	1095	990	1072	1298
3	1448	1162	1265	1321	1261	1342	1570
4	1715	1402	1502	1550	1529	1615	1840
5	1960	1638	1738	1775	1800	1892	2118
6	2223	1872	1974	2000	2071	2168	2389
7	2750	2338	2445	2450	2611	2710	2937
8	3012	2570	-	2675	2880	2972	3211
9	-	2804	-	-	3150	-	-
10							

Ring No. 4 (contd.)

Borehole DU

Turns	11	10	9	8	7	6	5
1	910	1018	1020	1158	840	835	940
2	1195	1285	1300	1439	1118	1105	1228
3	1470	1569	1575	1725	1408	1390	1522
4	1742	1840	1845	2012	1695	1675	1812
5	2022	2120	2122	2298	1985	1960	2105
6	2300	2385	2400	2583	2275	2245	2392
7	2577	2658	2675	2868	2562	2527	2668
8	2854	2930	2950	3153	2850	2810	2944
9	3130	3204	3225	3438	3136	3091	3220
10	-	-	-	-	-	-	-

Turns	4	3	2	1	C.A.	C.A.	
1	818	1030	950	990	990	985	
2	1112	1330	1235	1275	1215	1215	
3	1460	1630	1535	1570	1450	1450	
4	1690	1930	1829	1855	1680	1680	
5	1990	2230	2122	2145	1910	1910	
6	2290	2530	2415	2432	2140	2140	
7	2590	2830	2700	2432	2140	2140	
8	2884	-	2989	2720	2370	2370	
9	3180	-	3567	3295	2830	2832	
10	-	-	-	3584	-	-	

Ring No. 4 (contd.)

Borehole VL

Turns	C.B.	C.B.	18	17	16	15	14
1	760	750	745	735	730	700	730
2	970	970	1005	990	985	945	975
3	1182	1192	1270	1255	1243	1200	1230
4	1385	1405	1530	1510	1505	1465	1495
5	1593	1620	1800	1770	1765	1725	1760
6	1800	1835	2070	2035	2030	2000	2030
7	2010	2050	2334	2297	2290	2260	2290
8	2227	2267	2600	2559	2550	2520	2550
9	2444	2485	2860	2820	2810	2778	2811
10	2660	2700	3125	3083	3070	-	

Turns	13	12	11	10	9	8	7
1	740	720	700	750	740	765	740
2	995	975	960	980	980	1005	985
3	1265	1230	1210	1215	1225	1250	1230
4	1515	1500	1480	1455	1470	1500	1470
5	1775	1760	1730	1700	1720	1755	1720
6	2040	2030	2012	1950	1975	2015	1980
7	2300	2292	2258	2190	2220	2265	2230
8	2562	2554	2505	2430	2465	2515	2470
9	2820	2816	2750	2670	2713	2765	2730
10	3082	3078	2995	2910	2960	3015	2975

Ring No. 4 (contd.)

Borehole VL

Turns	6	5	4	3	2	1	C.A.
1	747	760	750	730	740	715	824
2	1000	1005	1010	980	995	955	1041
3	1245	1250	1280	1240	1255	1200	1257
4	1500	1505	1540	1500	1530	1450	1473
5	1760	1760	1815	1770	1800	1605	1690
6	2010	2020	2090	2050	2070	1970	1906
7	2260	2262	2357	2315	2336	2220	2123
8	2515	2517	2625	2576	2602	2468	2340
9	2770	2773	2890	2840	2870	2715	2556
10	-	-	3160	3100	3135	-	2772

Borehole DL

Turns	C.B.	15	14	13	12	11	10
1	850	820	720	862	800	770	880
2	1085	1108	1006	1148	1093	1065	1173
3	1321	1395	1292	1435	1386	1358	1465
4	1553	1685	1578	1719	1680	1650	1760
5	1790	1972	1865	2005	1972	1946	2050
6	2025	2260	2150	2292	2265	2240	2345
7	2260	2548	2436	2578	2558	2534	2638
8	2494	2835	2720	2865	2851	2828	2930
9	2728	3125	3010	3150	3145	3122	3224
10	2965	-	-	-	-	-	-

Ring No. 4

Borehole DL

Turns	9	8	7	6	5	4	3
1	610	705	805	775	811	722	810
2	906	990	1097	1065	1095	1018	1050
3	1200	1277	1390	1357	1378	1314	1290
4	1500	1563	1682	1648	1661	1611	1530
5	1794	1849	1975	1940	1945	1908	1770
6	2090	2135	2267	2230	2228	2204	2010
7	2386	2420	2560	2520	2512	2501	2251
8	2682	2707	2852	2812	2795	2797	2491
9	2978	2993	3145	3105	3080	3095	2729
10	3275	-	-	-	-	-	2970

Borehole VR

Turns	2	1	C.A.	C.A.	18	17	16
1	920	710	800	820	715	905	822
2	1188	965	1035	1054	1010	1197	1115
3	1456	1220	1271	1291	1308	1490	1405
4	1724	1475	1504	1525	1605	1781	1699
5	1990	1730	1740	1760	1901	2073	1990
6	2260	1985	1975	1995	2197	2365	2282
7	2528	2240	2210	2230	2495	2657	2574
8	2795	2495	2445	2465	2790	2950	2866
9	3065	2750	2680	2700	3087	3240	3158
10	-	-	-	2938	-	-	-

Ring No. 4 (contd.)

Borehole VR

Turns	15	14	13	12	11	10	9
1	715	828	810	770	914	810	770
2	1000	1113	1095	1050	1187	1083	1043
3	1286	1400	1381	1330	1458	1356	1316
4	1571	1683	1666	1610	1735	1630	1589
5	1857	1970	1952	1890	2005	1900	1862
6	2142	2255	2237	2170	2280	2177	2136
7	2428	2541	2523	2450	2552	2448	2410
8	2713	2826	2809	2730	2825	2720	2680
9	3000	3110	3095	3010	3098	2995	2955
10	-	-	3380	3290	-	3267	-

Turns	8	7	6	5	4	3	2
1	850	700	700	620	805	920	900
2	1025	870	962	895	1079	1194	1171
3	1200	1040	1224	1170	1353	1471	1442
4	1375	1210	1486	1445	1627	1745	1713
5	1550	1380	1748	1720	1901	2020	1984
6	1725	1550	2010	1995	2175	2295	2255
7	1900	1720	2272	2270	2450	2570	2526
8	2075	1890	2535	2545	2723	2845	2797
9	2250	2060	2796	2820	2998	3120	3068
10	2425	2230	3060	3095	3270	3395	3339

T-2470

Ring No. 4 (contd.)

Borehole VR

Turns	1	C.A.	C.A.
1	911	810	905
2	1172	1045	1141
3	1435	1280	1375
4	1695	1515	1610
5	1960	1750	1845
6	2220	1985	2080
7	2483	2220	2315
8	2745	2455	2551
9	3007	2690	2786
10	3270	2925	3020

Ring No. 5

Borehole H

Turns	C.B.	C.B.	14	13	12	11	10
1	815	969	860	740	860	740	860
2	930	1196	1135	1010	1125	1000	1145
3	1135	1422	1413	1280	1375	1270	1425
4	1320	1650	1693	1550	1640	1541	1715
5	1520	1875	1972	1830	1910	1830	2010
6	1745	2105	2250	2110	2175	2100	2285
7	1970	2331	2528	2383	2437	2372	2571
8	2285	2558	2806	2656	2699	2644	2843
9	2450	2785	3085	2930	2960	2916	3115
10	2975	3012	3360	3200	-	3188	3387

Ring No. 5 (contd.)

Borehole H

Turns	9	8	7	6	5	4	3
1	740	750	740	730	830	740	850
2	1010	1025	1017	1010	1110	1010	1130
3	1285	1300	1290	1280	1380	1280	1410
4	1545	1580	1570	1560	1670	1550	1695
5	1830	1870	1860	1845	1960	1830	1985
6	2110	2160	2142	2135	2240	2110	2275
7	2383	2441	2422	2415	2522	2383	2560
8	2656	2723	2702	2695	2804	2655	2844
9	2930	3005	2982	2975	3086	2930	3130
10	-	3288	3260	-	3368	3200	-

Borehole DD

Turns	2	1	C.A.	C.B.	14	13	12
1	742	800	813	950	890	905	1129
2	1000	1040	1040	1175	1173	1184	1389
3	1270	1290	1565	1400	1453	1563	1680
4	1545	1535	1490	1631	1742	1742	1958
5	1825	1780	1718	1863	2034	2021	2238
6	2100	2030	1942	2090	2314	2300	2509
7	2372	2276	2170	2320	2595	2580	2787
8	2644	2522	2395	2548	2875	2858	3065
9	2916	2768	2621	2776	3154	3137	3342
10	3188	3015	-		-	--	-

Ring No. 5 (contd.)

Borehole DD

Turns	11	10	10	9	8	7	6
1	1129	880	860	1128	1003	1005	975
2	1390	1112	1090	1389	1270	1265	1220
3	1678	1350	1332	1677	1553	1540	1465
4	1960	1600	1590	1961	1830	1820	1725
5	2239	1855	1850	2239	2110	2095	1990
6	2510	2120	2120	2511	2385	2388	2250
7	2788	3367	2372	2789	2662	2670	2500
8	3066	2614	2623	3067	2940	2943	2755
9	3344	2861	2875	3344	3215	3215	3010
10	-	3105	3125	-	3493	3489	-

Turns	5	4	3	2	1	C.A.	C.A.
1	920	900	870	1000	975	970	975
2	1160	1150	1140	2360	1235	1212	1195
3	1395	1400	1423	1535	1520	1442	1435
4	1625	1655	1712	1812	1790	1675	1670
5	1865	1915	1999	2095	2070	1910	1910
6	2100	2175	2285	2380	2350	2150	2142
7	2335	2430	2570	2663	2630	2385	2377
8	2570	2685	2854	2941	2905	2616	2610
9	2805	2940	3140	3220	3185	2850	2845
10	3040	-	-	-	3462	3086	3084

Ring No. 5
Borehole DL

Turns	C.B.	14	13	12	12	11	10
1	815	895	880	890	821	905	910
2	1035	1140	1080	1090	1025	1175	1160
3	1272	1378	1280	1280	1219	1445	1400
4	1502	1640	1580	1465	1405	1715	1650
5	1740	1890	1790	1645	1595	1985	1895
6	1979	2130	2101	1822	1780	2255	2135
7	2209	2377	2365	2000	1963	2525	2380
8	2442	2620	2630	2184	2152	2795	2628
9	2676	2860	2875	2368	2341	3066	2870
10	2910	-	-	2555	2530	-	3115

Turns	9	8	7	C.A.	C.B.	6	5
1	905	890	890	880	855	690	778
2	1146	1375	1135	1103	1070	754	905
3	1404	1615	1375	1335	1192	814	1032
4	1650	1855	1635	1573	1432	891	1158
5	1910	2085	1880	1810	1665	972	1285
6	2168	2310	2125	2044	1907	1111	1412
7	2428	2580	2373	2278	2144	1180	1538
8	2680	2852	2619	2512	2380	1252	1666
9	2932	3120	2866	2746	2618	1321	1792
10	3185	-	3113	2980	2855	1392	1920

Ring No. 5 (contd.)

Borehole VR

Turns	9	8	7	6	5	4	3
1	750	730	710	690	680	805	810
2	1005	985	960	953	934	1062	1060
3	1265	1236	1212	1215	1189	1320	1308
4	1521	1489	1465	1480	1440	1575	1557
5	1779	1742	1715	1742	1692	1833	1806
6	2035	1995	1965	2005	1950	2090	2055
7	2292	2248	2216	2268	2205	2347	2304
8	2550	2500	2467	2530	2458	2605	2555
9	2806	2754	2718	2795	2710	2861	2800
10	3064	3005	2970	3055	2966	3120	3050

Turns	2	1	C.A.				
1	815	720	620				
2	1072	960	837				
3	1330	1200	1054				
4	1586	1446	1271				
5	1843	1688	1488				
6	2100	1930	1705				
7	2357	2172	1922				
8	2615	2415	2140				
9	2870	2656	2356				
10	3130	2900	2575				

Ring No. 5 (contd.)

Borehole DR

Borehole VR

Turns	2	1	C.A.	C.A.	C.B.	18	17
1	610	750	500	900	650	780	760
2	850	1010	715	1125	865	1022	1005
3	1090	1270	940	1350	1085	1264	1255
4	1330	1480	1190	1570	1301	1506	1501
5	1540	1793	1380	1785	1518	1750	1748
6	1750	2037	1575	1995	1735	1990	1995
7	1960	2262	1793	2210	1950	2232	2242
8	2195	2495	2005	2428	2170	2475	2490
9	2425	2730	2220	2646	2385	2716	2735
10	2660	2968	2435	2864	2605	2959	2983

Turns	16	15	14	13	12	11	10
1	690	710	605	840	800	810	800
2	918	940	844	1088	1050	1065	1061
3	1150	1172	1085	1335	1301	1316	1322
4	1375	1403	1322	1585	1550	1570	1583
5	1600	1635	1560	1832	1798	1822	1845
6	1830	1865	1800	2080	2050	2075	2105
7	2058	2095	2340	2328	2300	2330	2368
8	2285	2327	2278	2576	2552	2581	2627
9	2514	2558	2517	2825	2800	2835	2888
10	2742	2790	2756	3072	3050	3087	3150

Ring No. 5 (contd.)

Borehole DR

Turns	C.B.	15	14	13	12	11	10
1	740	790	510	610	760	754	740
2	970	1050	750	850	1030	1018	1000
3	1200	1300	980	1090	1300	1288	1240
4	1420	1550	1210	1328	1555	1500	1470
5	1643	1800	1440	1538	1800	1800	1700
6	1860	2052	1675	1760	2050	2050	2005
7	2080	2304	1930	2010	2307	2305	2300
8	2305	2557	2180	2262	2565	2558	2543
9	2529	2810	2434	2515	2820	2812	2786
10	2750	3060	2687	2765	3078	3065	3030

Turns	9	8	7	6	5	4	3
1	700	755	810	770	800	810	670
2	935	1015	1066	1030	1055	1055	905
3	1180	1275	1322	1285	1295	1280	1145
4	1390	1465	1578	1541	1535	1510	1375
5	1600	1795	1834	1798	1805	1740	1615
6	1810	2041	2090	2055	2055	1975	1840
7	2035	2285	2346	2312	2350	2200	2075
8	2255	2540	2602	2570	2605	2450	2321
9	2476	2800	2858	2826	2860	2685	2568
10	2898	3055	3115	3085	3110	2920	2815

Ring No. 5 (contd.)

Borehole VL

Turns	13	12	11	10	9	8	7
1	810	750	775	785	740	775	755
2	1060	1000	1000	1030	960	1010	1065
3	1300	1240	1260	1295	1210	1250	1245
4	1550	1490	1520	1555	1450	1490	1500
5	1800	1740	1780	1810	1708	1740	1738
6	2050	2000	2050	2080	1960	1995	2000
7	2300	2250	2310	2340	2220	2238	2255
8	2548	2500	2560	2600	2470	2481	2499
9	2795	2748	2810	2850	2720	2724	2740
10	3040	3000	3060	3100	2970	2965	2990

Turns	6	5	4	3	2	1	C.A.
1	750	785	800	740	780	770	730
2	1000	950	990	970	945	1010	950
3	1260	1115	1200	1220	1110	1240	1180
4	1520	1290	1400	1460	1285	1470	1400
5	1790	1485	1620	1710	1400	1690	1620
6	2060	1680	1820	1970	1675	1922	1840
7	2320	1875	2020	2220	1920	2155	2060
8	2582	2056	2225	2467	2160	2385	2278
9	2845	2240	2430	2715	2405	2610	2500
10	3105	2420	2640	-	2647	2840	2720

Ring No. 5 (contd.)

Borehole DU

Turns	7	6	5	4	3	2	1
1	765	770	740	790	780	750	770
2	1031	1030	970	1055	1030	1010	1020
3	1277	1280	1210	1310	1265	1265	1280
4	1560	1540	1450	1570	1515	1530	1535
5	1790	1740	1690	1830	1760	1785	1800
6	2045	2040	1930	2080	2010	2050	2065
7	2303	2300	2170	2338	2255	2310	2315
8	2560	2565	2410	2595	2500	2570	2575
9	2813	2822	2650	2854	2745	2830	2830
10	3070	3080	2890	3110	2991	3090	3095

Borehole VL

Turns	C.A.	C.B.	18	17	16	15	14
1	675	740	950	810	915	770	770
2	895	959	1100	1042	1144	1010	1010
3	1105	1178	1348	1270	1373	1240	1240
4	1325	1395	1593	1505	1605	1470	1470
5	1543	1615	1860	1735	1835	1690	1700
6	1760	1835	2092	1968	2055	1920	1900
7	1977	2054	2325	2198	2295	2150	2127
8	2195	2275	2556	2428	2530	2380	2354
9	2410	2490	2788	2657	2755	2610	2580
10	2628	2710	3020	2888	2985	2840	2810

Ring No. 5

Borehole DL

Turns	4	3	2	1	C.A.	C.B.	C.B.
1	700	690	735	800	932	812	915
2	760	754	860	900	1169	1028	1132
3	832	816	980	1150	1406	1244	1350
4	891	890	1120	1300	1647	1460	1566
5	992	980	1260	1462	1880	1646	1783
6	1124	1112	1393	1617	2115	1890	2000
7	1257	1245	1525	1772	2355	2108	2217
8	1390	1376	1658	1925	2588	2325	2434
9	1523	1509	1790	2085	2825	2540	2650
10	1655	1640	1925	2235	3060	2756	2868

Borehole DU

Turns	14	13	12	11	10	9	8
1	615	744	880	845	770	750	810
2	878	1002	1127	1090	1012	1000	1060
3	1140	1260	1375	1335	1255	1240	1305
4	1405	1518	1620	1580	1495	1500	1565
5	1667	1776	1868	1825	1738	1760	1835
6	1930	2034	2115	2070	1980	2030	2100
7	2193	2295	2362	2315	2220	2286	2358
8	2436	2550	2610	2560	2464	2543	2616
9	2719	1808	2856	2805	2706	2798	2874
10	2983	3065	3105	3050	2948	3055	3130

Ring No. 6

Borehole H

Turns	C.B.	14	13	12	11	10	9
1	815	710	780	800	770	720	900
2	1045	995	1065	1080	1050	995	1165
3	1270	1278	1350	1365	1330	1295	1450
4	1500	1562	1635	1630	1620	1590	1737
5	1727	1845	1920	2100	1910	1868	2023
6	1955	2130	2205	2220	2200	2155	2310
7	2183	2415	2490	2510	2480	2442	2595
8	2410	2699	2775	2795	2766	2730	2880
9	2640	2980	3060	3078	3052	3015	3165
10	2867	3265	-	-	-	-	-

Turns	8	7	6	5	4	3	2
1	730	810	745	750	720	705	780
2	1000	1025	965	1020	995	955	1040
3	1270	1245	1210	1300	1265	1210	1310
4	1540	1450	1460	1595	1550	1480	1590
5	1810	1675	1710	1880	1835	1750	1880
6	2080	1900	1960	2163	2120	2225	2160
7	2350	2105	2204	2450	2400	2518	2435
8	2620	2335	2448	2730	2680	2811	2715
9	2890	2565	2695	3012	2960	3104	2995
10	-	2795	2930	3300	3242	3400	3268

Ring No. 6 (contd.)

Borehole H

Borehole DD

Turns	1	C.A.	C.B.	14	13	12	11
1	712	800	560	875	805	908	820
2	985	1035	775	1065	1005	1132	948
3	1250	1270	995	1250	1190	1360	1210
4	1520	1505	1210	1455	1400	1590	1420
5	1800	1740	1425	1655	1595	1822	1630
6	2070	1977	1640	1870	1810	2035	1840
7	2350	2210	1855	2080	2020	2260	2051
8	2625	2445	2070	2260	2218	2487	2263
9	2895	2680	2290	2450	2440	2710	2465
10	3170	2915	2505	2633	2635	2940	2680

Turns	10	9	8	7	6	5	4
1	592	680	675	668	670	682	623
2	738	768	882	895	885	882	873
3	882	970	1098	1125	1130	1085	1135
4	1032	1333	1548	1590	1580	2390	1393
5	1195	1450	1775	1800	1700	1680	1650
6	1348	1813	2005	2012	1940	1885	1928
7	1510	2030	2227	2240	2168	2085	2186
8	1665	2250	2450	2470	2395	2285	2445
9	1820	2467	2670	2700	2625	2485	2700
10	1980	2685	2895	2930	2852	2685	2960

Ring No. 6 (contd.)

Borehole DD

Borehole VL

Turns	3	2	1	C.A.	C.B.	19	18
1	618	800	700	815	855	760	1405
2	852	1010	900	1040	1068	1035	1640
3	1115	1220	1100	1266	1280	1300	1875
4	1370	1430	1305	1490	1495	1570	2105
5	1614	1640	1513	1715	1705	1825	2340
6	1923	1855	1710	1940	1920	2058	2575
7	2140	2066	1915	2165	2133	2290	2810
8	2355	2275	2120	2390	2345	2525	3045
9	2565	2485	2325	2615	2558	2757	-
10	2780	2695	2530	2840	2770	2990	-

Turns	17	16	15	14	13	12	11
1	1065	820	704	860	736	970	840
2	1295	1039	925	1095	982	1236	1085
3	1525	1258	1144	1335	1225	1500	1320
4	1755	1480	1361	1570	1455	1765	1570
5	1985	1695	1585	1808	1685	2035	1820
6	2220	1915	1805	2062	1915	2300	2055
7	2442	2134	2020	2290	2245	2570	2298
8	2675	2353	2240	2520	2490	2825	2540
9	2900	2572	2460	2760	2737	3090	2785
10	3135	2790	2680	2995	2990	3355	3027

Ring No. 6 (contd.)

Borehole VL

Turns	10	9	8	7	6	5	4
1	795	788	960	822	880	790	705
2	1040	1030	1210	1080	475	1030	940
3	1283	1269	1475	1330	708	1270	1176
4	1525	1510	1735	1560	945	1510	1411
5	1780	1752	1990	1780	1180	1750	1645
6	2020	1995	2250	2015	1420	1990	1882
7	2270	2240	2500	2250	1652	2232	2118
8	2495	2480	2750	2485	1888	2465	2354
9	2740	2715	3005	2720	2125	2710	2590
10	2983	2956	3262	2955	2360	2950	2825

Borehole DU

Turns	3	2	1	C.A.	C.B.	14	13
1	650	710	810	900	800	805	710
2	886	930	1034	1115	1017	1062	965
3	1120	1152	1258	1330	1234	1320	1220
4	1355	1370	1482	1542	1450	1576	1472
5	1592	1590	1706	1756	1665	1833	1725
6	1827	1810	1930	1970	1885	2090	1980
7	2065	2030	2155	2183	2102	2347	2234
8	2298	2250	2378	2390	2319	2605	2488
9	2534	2472	2602	2612	2536	2860	2740
10	2770	2690	2825	2825	2753	3120	2998

Ring No. 6 (contd.)
Borehole DU

Turns	12	11	10	9	8	7	6
1	900	812	750	710	770	740	700
2	1155	1060	1007	975	1030	995	963
3	1410	1310	1260	1235	1290	1250	1226
4	1668	1562	1518	1500	1550	1503	1490
5	1925	1812	1770	1762	1810	1758	1752
6	2180	2060	2025	2025	2070	2012	2015
7	2435	2310	2280	2288	2330	2267	2278
8	2692	2560	2535	2550	2590	2520	2540
9	2950	2810	2790	2815	2850	2776	2805
10	3205	3060	3045	-	3110	3030	3067

Turns	5	4	3	2	1	C.A.	C.A.
1	690	705	800	810	770	765	800
2	945	952	1050	1065	1025	980	1020
3	1205	1198	1301	1322	1281	1200	1238
4	1460	1445	1550	1578	1536	1415	1455
5	1718	1695	1800	1834	1790	1633	1675
6	1975	1940	2050	2090	2047	1850	1890
7	2232	2187	2300	2345	2300	2065	2115
8	2490	2435	2550	2602	2560	2285	2333
9	2746	2680	2800	2858	2814	2501	2552
10	3003	2928	-	3114	3070	2718	2770

Ring No. 6 (contd.)

Borehole DR

Turns	C.B.	14	13	12	11	10	9
1	715	705	810	688	718	800	790
2	950	990	1095	975	1005	1083	1062
3	1185	1270	1385	1265	1293	1367	1334
4	1422	1554	1671	1550	1580	1650	1605
5	1655	1837	1958	1840	1868	1934	1878
6	1892	2120	2245	2128	2155	2217	2150
7	2125	2405	2532	2416	2443	2501	2422
8	2360	2685	2820	2705	2730	2785	2695
9	2595	2970	3106	2992	3020	3068	2965
10	2830	3253	3393	3280	3305	3350	3238

Turns	8	7	6	5	4	3	2
1	640	700	705	810	840	755	765
2	925	982	983	1089	1120	1023	1035
3	1210	1265	1260	1368	1400	1291	1305
4	1495	1545	1540	1647	1677	1560	1575
5	1780	1828	1820	1925	1956	1827	1845
6	2063	2110	2095	2205	2235	2095	2115
7	2350	2392	2373	2484	2515	2363	2386
8	2635	2674	2651	2763	2793	2630	2656
9	2920	2955	2930	3042	3072	2900	2925
10	3205	3237	3207	3321	-	3167	3195

Ring No. 6 (contd.)

Borehole DR

Borehole DL

Turns	1	C.A.	C.B.	14	13	12	11
1	720	785	800	750	805	900	810
2	975	1020	1040	1017	1070	1165	1045
3	1230	1255	1280	1284	1335	1427	1280
4	1490	1490	1520	1550	1600	1690	1518
5	1740	1725	1760	1820	1865	1955	1755
6	1995	1960	2003	2085	2130	2220	1990
7	2250	2194	2240	2352	2395	2485	2225
8	2505	2430	2480	2620	2660	2748	2462
9	2760	2665	2740	2886	2925	3012	2698
10	3015	2900	2960	-	3190	-	2934

Turns	10	9	8	7	6	5	4
1	590	670	810	900	740	735	760
2	858	938	1025	1155	974	950	980
3	1125	1206	1245	1410	1208	1165	1200
4	1395	1474	1460	1665	1442	1380	1420
5	1662	1742	1678	1920	1676	1595	1640
6	1930	2010	1895	2175	1910	1810	1858
7	2198	2278	2112	2430	2145	2025	2080
8	2465	2545	2329	2685	2378	2240	2300
9	2730	2815	2546	2940	2612	2455	2520
10	3000	3080	2763	3195	2846	2670	2740

Ring No. 6 (contd.)

Borehole DL

Turns	3	2	1	C.A.	C.B.	19	18
1	660	715	820	810	780	680	770
2	920	960	1079	1048	995	940	1032
3	1178	1205	1338	1290	1214	1202	1295
4	1437	1450	1597	1530	1430	1465	1556
5	1695	1694	1856	1772	1648	1724	1818
6	1955	1938	2115	2012	1865	1985	2080
7	2215	2185	2375	2250	2082	2246	2342
8	2473	2430	2633	2490	2298	2507	2605
9	2730	2675	2890	2732	2516	2768	-
10	2990	2920	3150	2972	2733	3030	-

Turns	17	16	15	14	13	12	11
1	590	620	712	805	845	870	800
2	848	880	970	1060	1100	1130	1056
3	1105	1140	1230	1313	1356	1389	1312
4	1364	1397	1492	1567	1613	1647	1568
5	1622	1656	1752	1820	1869	1905	1825
6	1880	1915	2012	2075	2125	2168	2080
7	2138	2174	2270	2329	2380	2425	2336
8	2395	2433	2532	2583	2637	2684	2590
9	2654	2692	2790	2837	2893	2943	2848
10	-	2950	3050	3090	3150	3202	3105

Ring No. 6 (contd.)

Borehole VR

Turns	10	9	8	7	6	5	4
1	700	720	720	680	910	815	820
2	955	950	975	938	1167	1070	1070
3	1207	1180	1235	1195	1425	1320	1325
4	1460	1410	1491	1455	1681	1590	1575
5	1715	1642	1758	1713	1940	1840	1830
6	1970	1870	2005	1970	2195	2095	2080
7	2225	2100	2262	2228	2452	2350	2332
8	2478	2330	2520	2486	2710	2605	2584
9	2732	2560	2776	2744	2965	2863	2836
10	2985	2791	3033	3002	3225	3120	3090

Turns	3	2	1	C.A.	C.A.
1	735	740	800	600	605
2	990	985	1030	815	825
3	1245	1228	1270	1035	1042
4	1500	1472	1490	1251	1262
5	1760	1715	1715	1468	1480
6	2005	1960	1950	1685	1700
7	2265	2205	2177	1902	1920
8	2520	2448	2410	2120	2139
9	2775	2692	2640	2335	2355
10	-	2935	2870	2552	2576